2010

Marine Applications of an Autonomous Indicator-Based pH Sensor

Sarah E. Cullison
The University of Montana

MARINE APPLICATIONS OF AN AUTONOMOUS INDICATOR-BASED pH SENSOR

By

SARAH ELIZABETH CULLISON

B.A. Chemistry, St. Mary's College of Maryland, 2004

Dissertation

Presented in partial fulfillment of the requirements
for the degree of

Doctor of Philosophy
in Chemistry

The University of Montana
Missoula, MT

Spring 2010

Approved by:

Dr. Perry Brown, Associate Provost for Graduate Education
Graduate School

Dr. Michael DeGrandpre
Chemistry

Dr. Christopher Palmer, Chair
Chemistry

Dr. Xi Chu
Chemistry

Dr. Bob Yokelson
Chemistry

Dr. Heiko Langner
Geosciences

Cullison, Sarah, Ph.D., Spring 2010   Chemistry

Marine Applications of an Autonomous Indicator-Based pH Sensor

Chairperson: Michael DeGrandpre

  Currently, the lack of accurate in situ pH measurements limits our understanding of natural pH variability. In order to predict future pH changes in the oceans, quality high temporal resolution pH data are needed. This work used the newly developed Submersible Autonomous Moored Instrument for pH (SAMI-pH), a fully autonomous, in situ spectrophotometric pH sensor, to study oceanic pH variability. The three main goals of this research were to: determine the field performance of the new SAMI-pH, establish the utility of combining SAMI-pH data with in situ pCO_2 data to characterize the entire inorganic carbon cycle and establish pH variability, and what drives it, in a coral reef.
  Autonomous pH and pCO_2 sensors were deployed in tandem in Monterey Bay, CA from June to August 2007. The results showed that the pH-pCO_2 combination can provide information about data quality and can be used to model calcium carbonate ($CaCO_3$) saturation states. The pH and pCO_2 can be combined with a salinity-derived A_T to model both long and short-term DIC variability. The SAMI-pH was also used to examine pH variability on Media Luna coral reef, Puerto Rico for two month periods over three seasons in 2007 and 2008. pH on the reef was at a minimum of 7.89 pH units during the fall and at a maximum of 8.17 pH units during the winter. Half of this seasonal variability was driven by temperature, with the remaining changes due to organic carbon and $CaCO_3$ production. CO_2 gas fluxes showed that the reef was a source of CO_2 during the summer and fall, and a sink during the winter. Annually, the reef was a source of CO_2, with a flux of 1.19 mol m^{-2} year^{-1}. Calcium carbonate saturation states were modeled with pH and pCO_2 and showed seasonal values between 2.7-5.4 for aragonite and 4.0-7.0 for calcite. Both data sets showed that the SAMI-pHs performed well in extended field tests, including high fouling environments, making it possible to determine combined temporal pH and pCO_2 variability in unprecedented breadth and detail.

Acknowledgements

Table of Contents

List of Tables

List of Figures

CHAPTER 1

Introduction

1.1 Overview

Carbon dioxide (CO_2) levels in the atmosphere have increased dramatically (Fig. 1.1.1) since pre-industrial times as a result of fossil fuel consumption. This CO_2 increase has lead to a concurrent increase in the partial pressure of CO_2 (pCO_2) (Feely et al., 2004; Sabine et al., 2004) and decrease in the pH (Caldeira and Wickett, 2003) of the oceans. Data collected at the Bermuda Atlantic Time Series (BATS) and the Hawaii Ocean Time Series (HOTS) sites over the last 20 years have shown this pCO_2 increase and pH decrease (Fig. 1.1.2, Fig 1.1.3). The decrease in pH due to increasing CO_2 levels has been termed 'ocean acidification'.
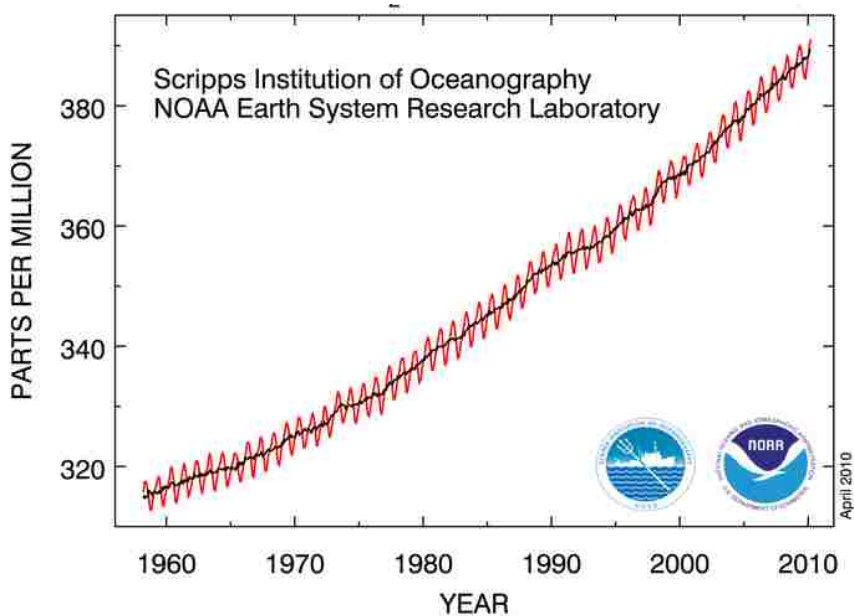
Fig. 1.1.1 Atmospheric CO_2 measured at Mauna Loa Observatory, HI. The red line shows the monthly mean CO_2 and the black line shows the monthly mean CO_2 after correction for the seasonal cycle. Data courtesy of the Mauna Loa Observatory.
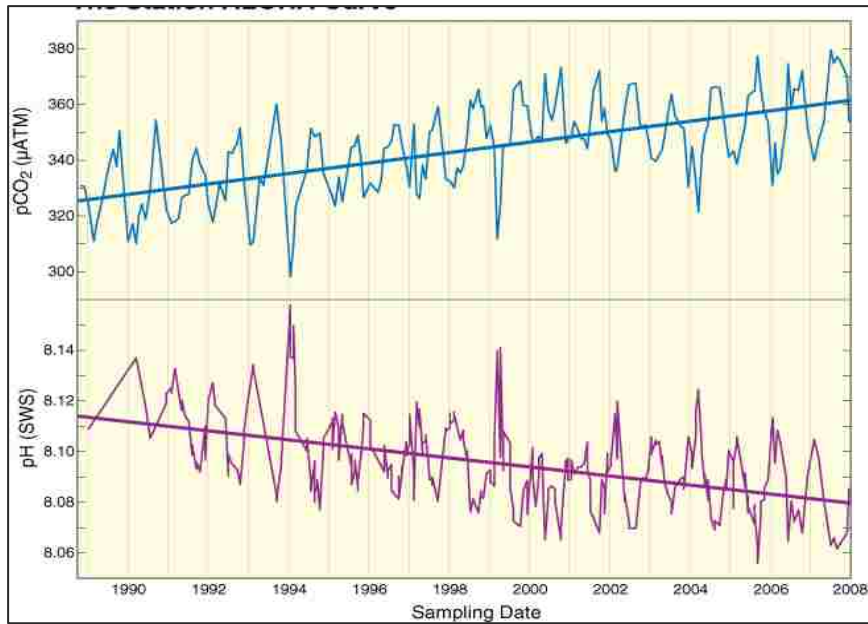
Fig. 1.1.2 Surface seawater pCO_2 (blue) and pH (purple) at Station ALOHA, 115 km north of Oahu, HI. Station ALOHA is part of the Hawaii Ocean Time Series (HOTS) program. pCO_2 and pH were modeled from ~monthly discrete A_T and DIC samples collected at Station ALOHA. Data courtesy of the HOTS program
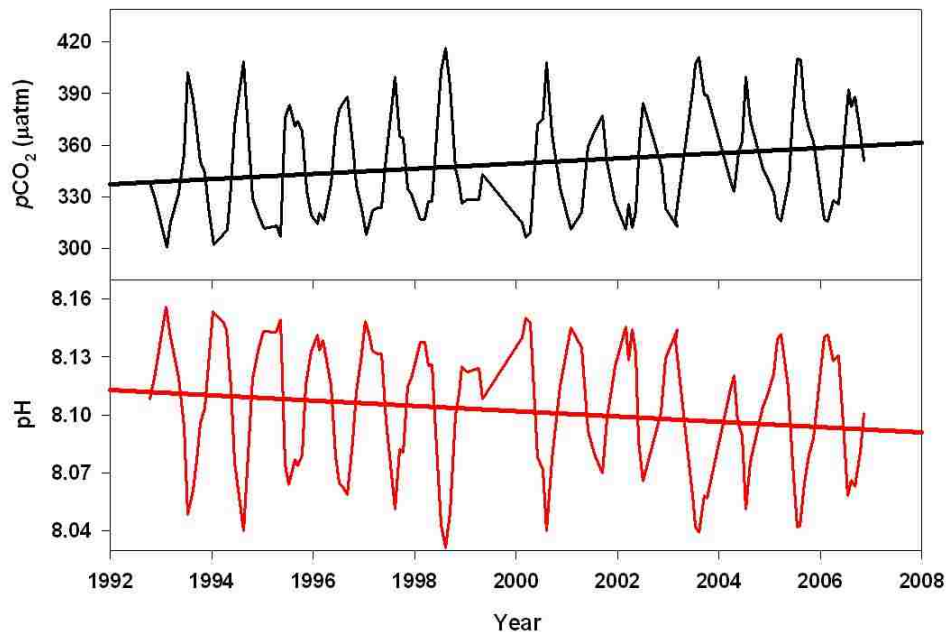
Fig. 1.1.3 pCO_2 (black) and pH (red) modeled from discrete A_T and DIC measured at the BATS station. The BATS station is located in the Atlantic Ocean near Bermuda. Data courtesy of the BATS program.

2

The inorganic carbon cycle consists of four main, measureable parameters. These parameters are pH, $p\text{CO}_2$, total alkalinity (A_T) and total dissolved inorganic carbon (DIC). The carbonate equilibria are shown below in Eqns. (1.1-1.4). It is difficult to distinguish between the $\text{CO}_2(aq)$ and H_2CO_3 species and they are typically combined into one theoretical species, $\text{H}_2\text{CO}_3{}^*$ (Eqns. (1.5-1.7)). The DIC and A_T expressions are shown in Eqns. (1.8-1.9). In the A_T equation (Eqn. (1.8)), $\text{B(OH}_4)^-$ is the main contributor to A_T other than carbonates. $\text{B(OH}_4)^-$ is conservative with salinity and is accounted for in inorganic carbon modeling using the measured salinity. Using the equilibrium expressions and the DIC and A_T expressions for seawater, the carbonate equilibria can be reduced to two equations with four unknowns. Once any two of the four measureable inorganic carbon parameters are known, the remaining two parameters can be calculated using these expressions (Millero, 1995).

$$\text{CO}_2(g) \leftrightarrow \text{CO}_2(aq) \tag{1.1}$$

$$\text{CO}_2(aq) + \text{H}_2\text{O} \leftrightarrow \text{H}_2\text{CO}_3 \tag{1.2}$$

$$\text{H}_2\text{CO}_3 \leftrightarrow \text{H}^+ + \text{HCO}_3{}^- \tag{1.3}$$

$$\text{HCO}_3{}^- \leftrightarrow \text{H}^+ + \text{CO}_3{}^{2-} \tag{1.4}$$

$$\text{H}_2\text{CO}_3{}^* = \text{CO}_2(aq) + \text{H}_2\text{CO}_3 \tag{1.5}$$

$$\text{CO}_2(g) \leftrightarrow \text{H}_2\text{CO}_3{}^*(aq) \tag{1.6}$$

$$\text{H}_2\text{CO}_3{}^* + \text{H}_2\text{O} \leftrightarrow \text{H}^+ + \text{HCO}_3{}^- \tag{1.7}$$
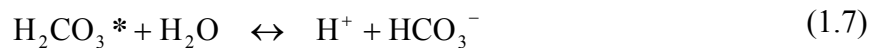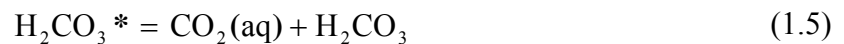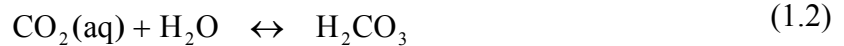
$$DIC \ = \ [H_2CO_3\text{*}] + [HCO_3^-] + [CO_3^{2-}] \qquad (1.8)$$

$$A_T \ = \ [HCO_3^-] + 2[CO_3^{2-}] + [OH^-] + [B(OH)_4^-] - [H^+] \qquad (1.9)$$

Measuring even two of these parameters in the ocean, however, can be a difficult task. Carbon cycle time series such as the BATS collect annual data (Fig. 1.1.3), but are very expensive to maintain and can have low temporal resolution (1 sample/month). The use of autonomous sensors to measure carbon cycle parameters allows high temporal resolution data (e.g. 1 sample/30 minutes) to be collected at numerous locations around the world for a fraction of the cost. To this end, the Submersible Autonomous Moored Instruments for CO_2 (SAMI-CO_2) and pH (SAMI-pH) were previously developed (DeGrandpre et al., 1995; Martz et al., 2003; Seidel et al., 2008) to measure aquatic pCO_2 and pH, respectively. While the SAMI-CO_2 has been used extensively in the past (e.g. DeGrandpre et al., 1999; DeGrandpre et al., 1995; DeGrandpre, 2002; Kuss et al., 2006), the SAMI-pH has only recently been optimized for seawater measurements. The SAMI-pH had undergone only one two-week field test at the Scripps Institution of Oceanography (Seidel et al., 2008) at the start of this work. The development of the SAMI-pH made it possible to measure two of the four inorganic carbon parameters, pH and pCO_2, in situ for extended time periods. Sensors for the remaining parameters, DIC and A_T, are still in the developmental stages (Martz et al., 2006; Sayles and Eck, 2009).

Previous work has focused on determining the best combination of inorganic carbon parameters for modeling, based on thermodynamic and measurement errors (Byrne, 1999; Clayton et al., 1995; Lee et al., 2000; McElligott et al., 1998; Millero, 1995). Table 1.1.1 shows the errors associated with each of the six possible

combinations of parameters. These estimates were modeled using discrete seawater measurements of each parameter (Millero, 1995), assuming the current estimates of accuracy and precision for each parameter, shown in Table 1.1.2. pH-pCO$_2$ is considered the worst pairing because it produces errors in the modeled A$_T$ and DIC which are much greater than the measurement accuracies of A$_T$ and DIC. Since pH and pCO$_2$ are directly proportional to each other for a given DIC or A$_T$, any small changes in either pH or pCO$_2$ that are not mirrored by the second parameter will lead to compounding large errors in the modeled DIC or A$_T$ (Dickson and Riley, 1978). (see Chapter 3 introduction for a more detailed explanation of the pH-pCO$_2$ pairing). Despite accuracy problems with the pH-pCO$_2$ pair, pH and pCO$_2$ are currently the only inorganic parameters that can be measured autonomously in situ, as mentioned above. The development of the SAMI-pH provided the opportunity to evaluate the utility of combining pH and pCO$_2$ measurements for inorganic carbon modeling, using in situ data rather than discrete samples. Even if the modeled A$_T$ and DIC contain absolute accuracy errors, the continuous data can still provide information about short-term and seasonal changes in these parameters that is not available from discrete samples.

Table 1.1.1 Estimated probable absolute errors in the calculated parameters of the carbonate system (Table taken from Millero, 1995).

Input	ΔpH (pH units)	ΔA_T (μmol kg^{-1})	ΔDIC (μmol kg$^{-1)}$	ΔpCO$_2$ (μatm)
pH-A$_T$	-----	-----	±3.8	±2.1
pH-DIC	-----	±2.7	-----	±1.8
pH- pCO$_2$	-----	±21	±18	-----
pCO$_2$-DIC	±0.0025	±3.4	-----	-----
pCO$_2$-A$_T$	±0.0026	-----	±3.2	-----
A$_T$-DIC	±0.0062	-----	-----	±5.7

Table 1.1.2 Estimates of the accuracy and precision of pH, A$_T$, DIC and pCO$_2$ measurements (Table taken from Millero, 1995).

Analysis	Precision	Accuracy
pH (spectrophotometric)	± 0.0004 pH units	± 0.002 pH units
A$_T$ (potentiometric)	± 2 μmol kg^{-1}	± 4 μmol kg^{-1}
DIC (coulometric)	± 1 μmol kg^{-1}	± 2 μmol kg^{-1}
pCO$_2$ (infrared)	± 0.5 μatm	± 2 μatm

1.2 Background

1.2.1 Importance of Inorganic Carbon Parameters

Measurements of each of the carbonate parameters can provide information about the inorganic carbon cycle. For example, the DIC can be used to determine ecosystem productivity. When DIC increases, carbon is being added to the system, while a decrease

indicates that carbon is being removed. These changes can be driven by numerous

processes such as photosynthesis, gas exchange, mixing or the export of carbon to the

deep oceans (Key et al., 2004). Key et al. (2004) summarized discrete DIC

measurements from numerous ocean sampling experiments into a global spatial

distribution of DIC in the oceans (Fig. 1.1.4). DIC is generally lowest near the equator

and increases with latitude towards the poles. However, in order to determine which

processes are driving the DIC changes, additional carbonate parameters are needed. Key

et al. (2004) found that the surface distribution of DIC largely follows a pattern similar to

nutrient distribution. This relationship decreases towards the polar and subarctic fronts

due to the effects of mixing and gas exchange on DIC.
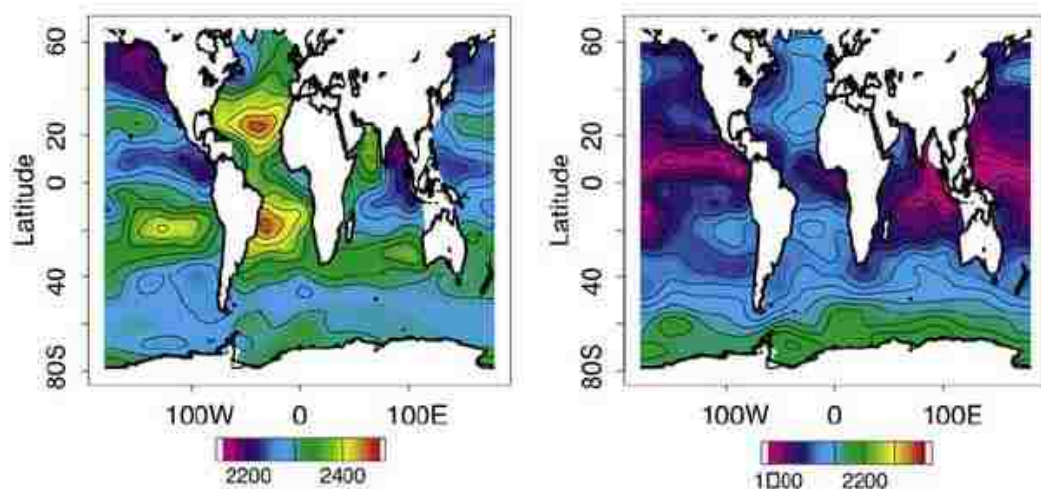
Fig. 1.1.4 Annual mean distribution of A_T (left, μmol kg^{-1}) and DIC (right, μmol kg^{-1}) in
the surface ocean compiled from ocean sampling expeditions. The DIC scale should be
1000 μmol kg^{-1} on the purple end. Unlabeled contours at an interval of 25 μmol kg^{-1} are
included to help discern gradients. (Figure taken from Key et al., 2004)

$p\mathrm{CO_2}$ data can be used to calculate the $\mathrm{CO_2}$ gas flux between the ocean and the atmosphere. Information about the spatial and temporal variability in the $\mathrm{CO_2}$ flux is important for understanding the global carbon cycle and for determining future atmospheric $\mathrm{CO_2}$ levels as anthropogenic inputs increase (Takahashi et al., 2009). The $\mathrm{CO_2}$ flux is also important for determining what is driving DIC changes, as $\mathrm{CO_2}$ invasion or loss changes the DIC concentration. $\mathrm{CO_2}$ fluxes have been previously determined in numerous different ocean basins (e.g. Bates, 2002; DeGrandpre, 2002; DeGrandpre et al., 2004; Feely et al., 2006; Omar and Olsen, 2006). Takahashi et al. (2009) compiled surface water $p\mathrm{CO_2}$ measurements to produce a global estimate of the mean $\mathrm{CO_2}$ flux (Fig. 1.1.5). The equatorial Pacific Ocean is the largest source of $\mathrm{CO_2}$ to the atmosphere, while the mid-latitudes and the North Atlantic Ocean are the largest sinks for atmospheric $\mathrm{CO_2}$. The North Atlantic sink is attributed to strong phytoplankton blooms in the spring and strong cooling in the winter. The mid-latitudes are a strong sink primarily due to high winds between 40° and $50^{\circ}\mathrm{S}$ and low $p\mathrm{CO_2}$ values produced when cooled subtropical gyre waters with low $p\mathrm{CO_2}$ meet subpolar waters with biologically-lowered $p\mathrm{CO_2}$ (Takahashi et al., 2009). The sink over the southern ocean is small due to large seasonal ice cover that reduces gas exchange (Takahashi et al., 2009).
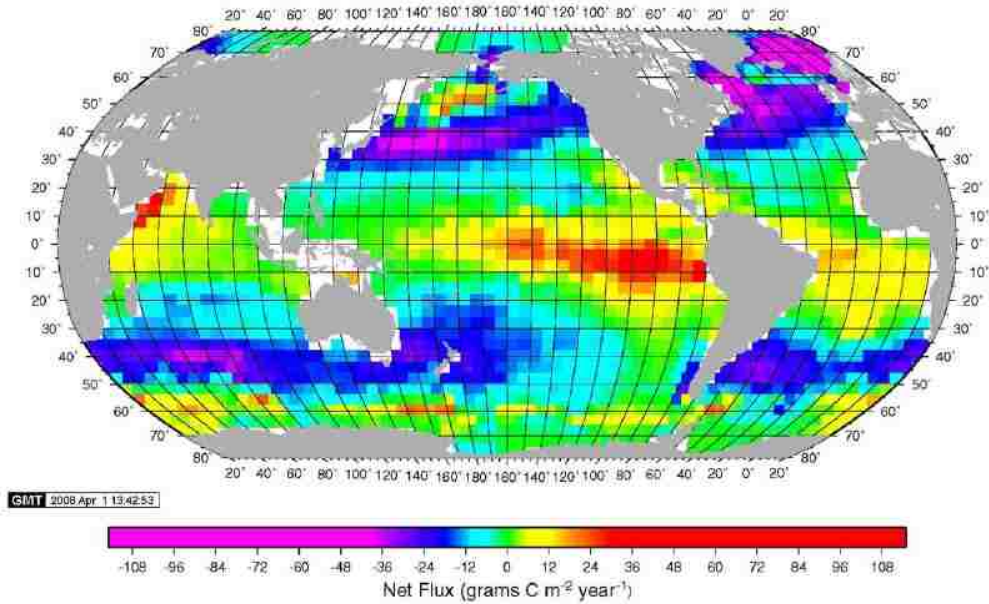
Fig. 1.1.5 Mean annual sea-air CO_2 flux (g-C m^{-2} yr^{-1}) for the year 2000 based on 3.0 million surface water pCO_2 measurements obtained since 1970. Positive values (yellow to red) show a flux from the ocean to the atmosphere (Figure taken from Takahashi et al., 2009). Reprinted with permission from Elsevier.

Since photosynthesis and respiration have little effect on A_T (Millero, 1998), A_T measurements are not useful for determining production. The distribution of A_T in the oceans is mainly driven by evaporation-precipitation, mixing and the precipitation-dissolution of calcium carbonate ($CaCO_3$). When calcification is not present, A_T is generally conservative with temperature and salinity. Reasonable A_T estimates can be calculated from region-specific A_T algorithms, using measured temperature and salinity data (Lee et al., 2006; Millero, 1998). When calcification is present, A_T cannot be estimated from temperature and salinity. However, direct measurements of the change in A_T over time can be used to determine calcification rates since every mol of $CaCO_3$ consumed during calcification decreases A_T by two mols (Eqn. (1.9)) (Barnes, 1983). This simple relationship holds because A_T is not largely affected by production.

However, A_T can be affected by terrestrial A_T inputs (Kawahata et al., 2000), which can complicate the system. Key et al. (2004) also summarized A_T measurements into a global spatial distribution of A_T in the oceans (Fig. 1.1.4). Global measurements show that A_T varies more with latitude than DIC. The highest A_T values are observed in Atlantic, both north and south of the equator, following trends in salinity. Low A_T values are observed both in the poles and near the equator in the Pacific Ocean, again following salinity trends (Key et al., 2004). A_T is higher in the Southern Ocean due to upwelling of deep waters with accumulated A_T from the dissolution of calcium carbonate (Key et al., 2004).

Measurements of pH cannot provide information about production and carbon fluxes by themselves, but they can be combined with A_T estimates from temperature and salinity (Lee et al., 2006; Millero, 1998). The pH and A_T can be used to model DIC and pCO$_2$ as well as CaCO$_3$ saturation states. Estimates of pH are not possible from temperature and salinity measurements as with the A_T, so direct measurements of pH are more useful than measurements of A_T when a single parameter is determined. Global mean pH distributions based on discrete measurements are not currently available due to the lack of accurate pH measurements.

1.2.2 History of pH Measurements

While the pH of seawater has been measured for almost 100 years, and used to be a common chemical parameter measured in the ocean (Dickson, 1993), pH measurements came to be seen as unreliable and dropped out of use. This was largely due to problems with the measurement method. pH has historically been measured using potentiometry.

In this method, a glass electrode sensitive to pH is used to measure changes in electrical potential relative to a reference electrode. These electrode measurements can suffer from large systematic errors due to electrode drift, susceptibility to electromagnetic interference and problems with the reference electrode (Brezinski, 1983; Davison and Woof, 1985; Dickson, 1993; French, 2002). Two pH electrodes will typically not output the same potentials for the same solution (Martz et al., 2003). The composition of the pH standards must closely match the experimental solution to avoid large changes in the liquid junction potential from calibration to measurement. In seawater, this requires the use of synthetic seawater buffers (Dickson, 1993). However, even with careful calibration pH electrodes, with the exception of the hydrogen electrode, are not capable of achieving the needed accuracy (0.002 pH units) (Seidel et al., 2008) for inorganic carbon modeling. Hydrogen electrodes have been used to estimate pH to within 0.002 pH units (DelValls and Dickson, 1998) but these measurements are difficult and not generally used in modern laboratories or for in situ pH studies. For these reasons, even though pH data can offer a wealth of information about the inorganic carbon system and biological production in the ocean, pH measurements have not been widely used.

pH electrodes have been used in some oceanographic studies when the desire to overcome the spatial and temporal limitations of discrete A_T and DIC sampling outweighed the potential problems of pH electrodes. Fuhrmann and Zirino (1988) used a shipboard flow-through system to measure pH with high spatial resolution in both the horizontal and vertical directions. Using seawater buffers for calibration, they were able to obtain an accuracy of 0.01 ± 0.003 pH units. Mackey et al. (1989) used pH electrodes to measure vertical pH profiles as well as surface pH values. These pH values were

combined with a A_T value estimated from water depth to calculate pCO_2. The absolute accuracy of these pCO_2 measurements was limited by the study's pH accuracy, ~0.008 pH units, and the authors propose this data is more readily used for determining changes in pCO_2 rather than absolute accuracy. While these studies show that pH data can be collected with high spatial resolution using flow-through systems and pH electrodes, they also demonstrate that these methods do not achieve the pH accuracy needed for inorganic carbon modeling (0.002 pH units).

Over the last twenty years pH measurements have been making a comeback with the development of the spectrophotometric pH technique (Byrne and Breland, 1989). In this method, a water sample is mixed with a sulfonephthalein indicator. Different pH values change the ratio of the acid to base forms of the indicator and these changes are recorded with a spectrophotometer. Spectrophotometric pH methods are capable of much higher precision (0.0007 pH units) and accuracy (0.002 pH units) (Seidel et al., 2008), compared to potentiometric pH methods. The accuracy of spectrophotometric pH methods depends on the $pK_a^{'}$ of the indicator solution, which can be accurately determined in seawater solutions. In addition, spectrophotometric pH data can be re-evaluated as better measurements of dye equilibrium constants are obtained in the future (Clayton and Byrne, 1993). This type of accuracy correction is not possible with pH electrodes since the accuracy of potentiometric methods is based on a calibration curve, rather than on equilibrium constants that can be improved. While several sensors for indicator-based pH measurements have been developed in the past (Liu et al., 2006; Nakano et al., 2006), these instrument designs require high power and are limited to field deployments of a few days. The lack of an accurate in situ pH instrument has made

quality long-term pH measurements scarce. The SAMI-pH (Martz et al., 2003; Seidel et al., 2008) used in this research is the only autonomous, in situ instrument currently available for long-term pH measurements, making the data collected here unique.

In addition to its use as one of the four inorganic carbon parameters, current interest in pH measurements is driven by the desire to understand the effects of ocean acidification. Ocean acidification has rapidly become a hot topic in climate research, and has the potential to be one of the most serious outcomes of fossil fuel consumption. Once CO_2 is absorbed in the oceans there is no practical way to remove it, with the oceans taking thousands of years to naturally return to a higher pH state. Models based on current CO_2 emissions scenarios predict that ocean pH may be lower in the next few centuries than anytime in the last 300 million years (Caldeira and Wickett, 2003). In addition, these pH changes will likely have a large negative impact on $CaCO_3$ forming organisms and ecosystems, with damages possibly leading to billions of dollars per year in economic losses (Raven et al., 2005). Riebesell et al. (2000) have shown that the structure of coccolithophorid shells begins to break down when the organisms are incubated at elevated CO_2 levels (Fig. 1.1.6). Laboratory tests have also shown that coral health and coral $CaCO_3$ production also begin to decline as the pCO_2 of seawater is increased (Jokiel et al., 2008; Langdon and Atkinson, 2005; Langdon et al., 2003; Leclercq et al., 2000).
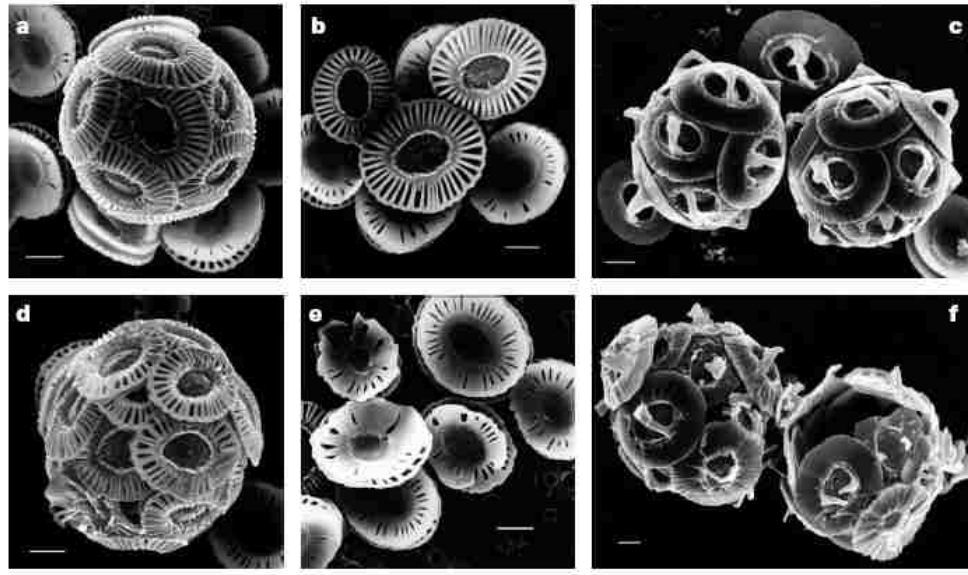
Fig. 1.1.6 SEM photographs of coccolithophorids under different CO_2 conditions. (a-c) Incubated at ~300 ppm CO_2. (d-f) Incubated at 750-850 ppm CO_2. Coccolithophorid structure begins to break down under the high pCO_2 scenario (Figure taken from Riebesell et al., 2000). Reprinted with permission from Macmillian Publishers Ltd.: [Nature].

Newer studies have shown that $CaCO_3$ production is dependent on the aragonite saturation state, rather than absolute pCO_2 levels. Aragonite and calcite are the main biogenic mineral forms of $CaCO_3$. Aragonite is the more soluble form of $CaCO_3$. The saturation state is defined in Eqn. (1.10), where Ω is the saturation state for aragonite or calcite and K_{sp} is the solubility product for either aragonite or calcite. When the saturation is > 1, the mineral is supersaturated. A saturation equal to 1 is saturated and a saturation < 1 is undersaturated. Fabry et al. (2008) found that pteropod shells incubated in waters with an aragonite saturation < 1 begin to dissolve (Fig 1.1.7). Since saturation is a gradient, and not a single threshold value, organisms that use $CaCO_3$ to form their shells can see decreased growth and health in waters with low saturation values, even if the value is above 1.

$$\Omega = \frac{[Ca^{2+}][CO_3^{2-}]}{K_{sp(cal/arag)}}$$

<div align="right">(1.10)</div>
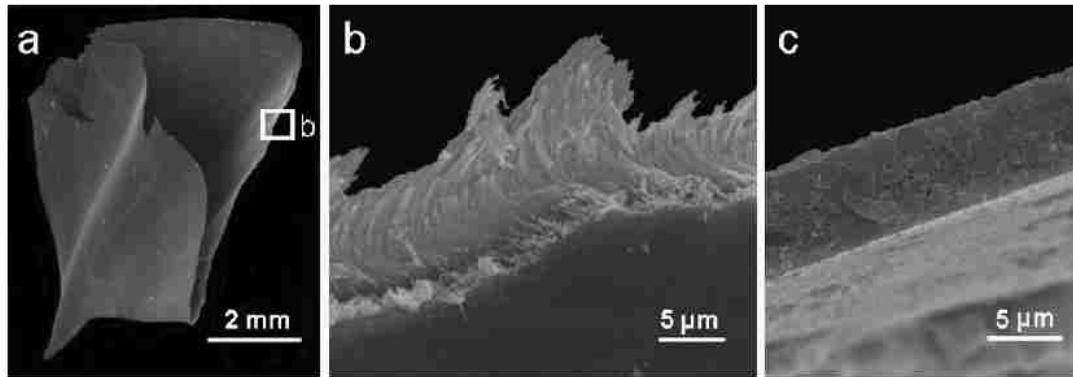
Fig. 1.1.7 SEM photographs of a pteropod shell. (a) Whole shell of an animal incubated for 48 hours in a closed container, where animal respiration forced the aragonite saturations state <1. (b) Magnified portion of the leading edge of the shell section shown in (a), revealing dissolution of aragonite rods. (c) Magnified leading edge of the shell of a control animal incubated in seawater that remained supersaturated with aragonite for the duration of the experiment (Figure taken from Fabry et al., 2008). Reprinted with permission from Oxford University Press.

While surface water undersaturation was not projected to occur until 2050 (Orr et al., 2005), Feely et al. (2008) found that "acidified waters" with an aragonite saturation < 1 are already reaching the surface ocean along the continental shelf of western North America. These "acidified waters" are brought to the surface through upwelling of deep ocean waters that have lower saturation values. As shown by Feely et al. (2008), the first areas to experience undersaturation will be those with naturally low aragonite saturation levels. Feely et al. (2008) projected that aragonite saturation in California shelf waters would be ~0.2 units higher without the anthropogenic CO_2 signal, bringing the values above saturation. McNeil and Matear (2008) have projected that wintertime aragonite

saturation will be below 1 in the Southern Ocean by 2030-2038, due to the anthropogenic

impact on the already seasonally low saturation values.

1.3 Research Objectives

This research consisted of three main goals, all centered on increasing our

understanding of the global inorganic carbon cycle. The first goal was to further test, in

the laboratory and field, the new SAMI-pH instrument. The accuracy of the SAMI-pH

was evaluated on numerous different instruments and the robustness of the SAMI-pH was

tested in several field environments, including high fouling areas.   The second goal was

to determine if pH and pCO$_2$ data can be used to accurately model the remaining two

carbonate parameters, A$_T$ and DIC. The accuracy of modeled data was evaluated over

both long and short-term time scales. The final goal was to use the SAMI-pH and SAMI-

CO$_2$ to measure pH and pCO$_2$ on a coral reef ecosystem. These measurements made it

possible to establish both diel and seasonal pH variability on the reef and to determine

what is driving the changes. The first goal is addressed in Chapter 2, which details

laboratory and field testing of the SAMI-pH. The second goal was studied at a field site

off the coast of California. Chapter 3 describes the second goal, which was studied at a

field site off the coast of California. In Chapter 4, the pH and pCO$_2$ dynamics on a coral

reef off the southwestern coast of Puerto Rico are examined. Finally, Chapter 5 contains

a summary of the dissertation research as well as projected future work.

CHAPTER 2

Methods and Instrument Performance

This chapter describes how the SAMI-pH works, the field deployments using a SAMI-pH, and performance characteristics of the instrument including e-values, pH accuracy and battery volt usage. E-values and accuracy tests were run on all SAMI-pHs before each field deployment.

2.1 Instrument overview

The SAMI-pH is based on the spectrophotometric pH technique. An in-depth discussion of the theoretical basis for spectrophotometric pH measurements is given in Clayton and Byrne (1993). A brief discussion of spectrophotometric pH theory is given below. This method uses a diprotic pH indicator that changes color based on the absorbance spectra of the diprotonated $[H_2L]$, monoprotonated $[HL^-]$ and deprotonated $[L^{2-}]$ forms of the indicator (Seidel, 2006). For seawater measurements, the equilibrium between the monoprotonated (acid) and deprotonated (base) forms of the indicator meta-cresol purple (mCP) was used to determine the pH of the solution with the relationship in Eqn. (2.1). Equation (2.1) can be converted to the form in Eqn. (2.2) to calculate pH.

$$HL^- \leftrightarrow H^+ + L^{2-} \tag{2.1}$$

$$pH = pKa' + \log\left(\frac{[L^{2-}]}{[HL^-]}\right) \tag{2.2}$$

In Eqn. (2.2), the pKa' is the apparent dissociation constant for Eqn. (2.1) and takes into account the temperature and ionic strength dependence off the equilibrium constant (Seidel, 2006). When using the pKa', the ion activity coefficients do not need to be included in Eqn. (2.2), leaving only the concentrations of L^{2-} and HL^-. For mCP, the peak acid wavelength is 434 nm and the peak base wavelength is 578 nm (Fig. 2.1.1). Since the absorbances for the acid and base forms overlap at the peak wavelengths, Eqn. (2.2) must be modified to take into account the small amount of the base form at the acid wavelength, and vice versa.
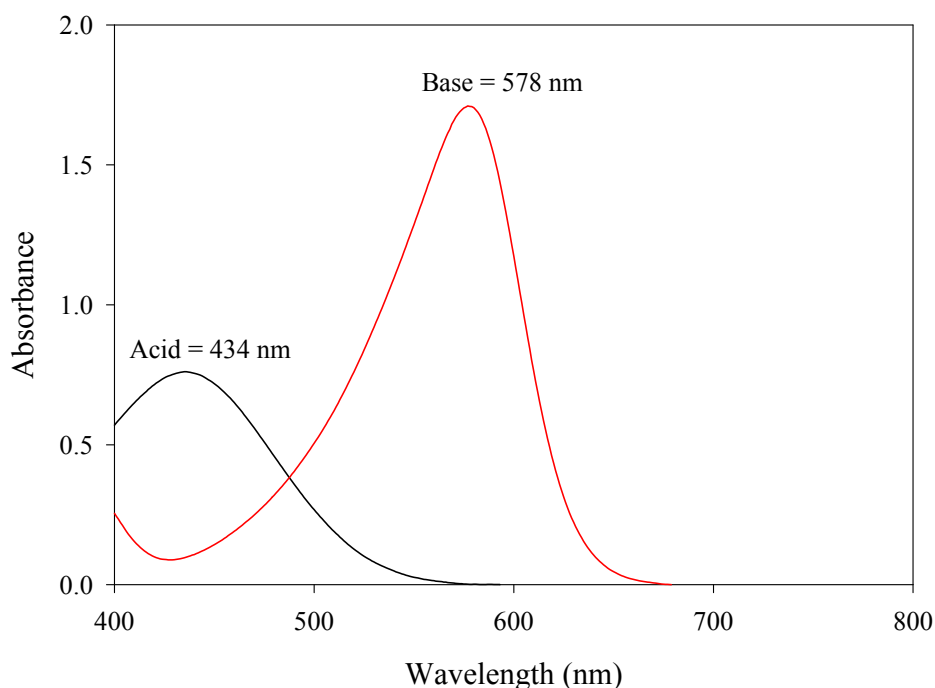
Figure 2.1.1 Absorbance spectra for ~5.0 x 10^{-5} mol kg^{-1} mCP solutions at a pH of 4 (black) and a pH of 12 (red) using the Cary 300 (10 cm cell). The absorbance maximum for the acid spectrum is 434 nm while the base spectrum is at 578 nm. Figure taken from Seidel (2006).

This is accomplished using the Beer's Law relationship (A=εbc). The absorbances at the acid (A_1) and base (A_2) wavelengths are shown in Eqns. (2.3-2.4),

18

$$A_1 = {}_{HL}\varepsilon_{434}[HL^-]b + {}_L\varepsilon_{434}[L^{2-}]b \qquad (2.3)$$

$$A_2 = {}_{HL}\varepsilon_{578}[HL^-]b + {}_L\varepsilon_{578}[L^{2-}]b \qquad (2.4)$$

where ε is the molar absorptivity for the HL^- and L^{2-} forms of the indicator at the wavelengths of maximum absorbance for each form, b is the pathlength and [] designates the concentration of each indicator form (Seidel, 2006). Equations (2.2), (2.3) and (2.4) are combined to give the new pH equation (Eqn. (2.5)).

$$pH = pK_a' + \log\left(\frac{R - e_1}{e_2 - Re_3}\right) \qquad (2.5)$$

In Eqn. (2.5), R is the ratio of the absorbances at the peak wavelengths (A_{578}/A_{434}) and the e_i's are the ratios of the molar absorptivities (ε) of the two species at each wavelength:

$$e_1 = \frac{\varepsilon_{a578}}{\varepsilon_{a434}} \qquad e_2 = \frac{\varepsilon_{b578}}{\varepsilon_{a434}} \qquad e_3 = \frac{\varepsilon_{b434}}{\varepsilon_{a434}} \qquad (2.6)$$

Once the e-values are determined for an instrument, the pH of a seawater sample is determined by mixing the sample with the mCP indicator and measuring the absorbances at the peak wavelengths to calculate R. However, adding mCP indicator to the seawater sample can perturb the pH of the sample. When measuring spectrophotometric pH in the laboratory, 10 cm pathlength cells are typically used so that a small amount of indicator

(indicator concentrations typically around 1 x 10^{-6} mol kg^{-1}) can be added to the seawater

and still achieve high enough absorbencies without perturbing the pH more than 0.001

pH units (Seidel, 2006). To account for the remaining 0.001 pH unit perturbation, several

small additions of mCP can be added to the seawater sample, instead of one larger

addition, to create a plot of indicator concentration versus pH (Fig. 2.1.2). These points

can be linearly extrapolated back to zero indicator concentration to determine the final

pH of the seawater sample without the perturbation.
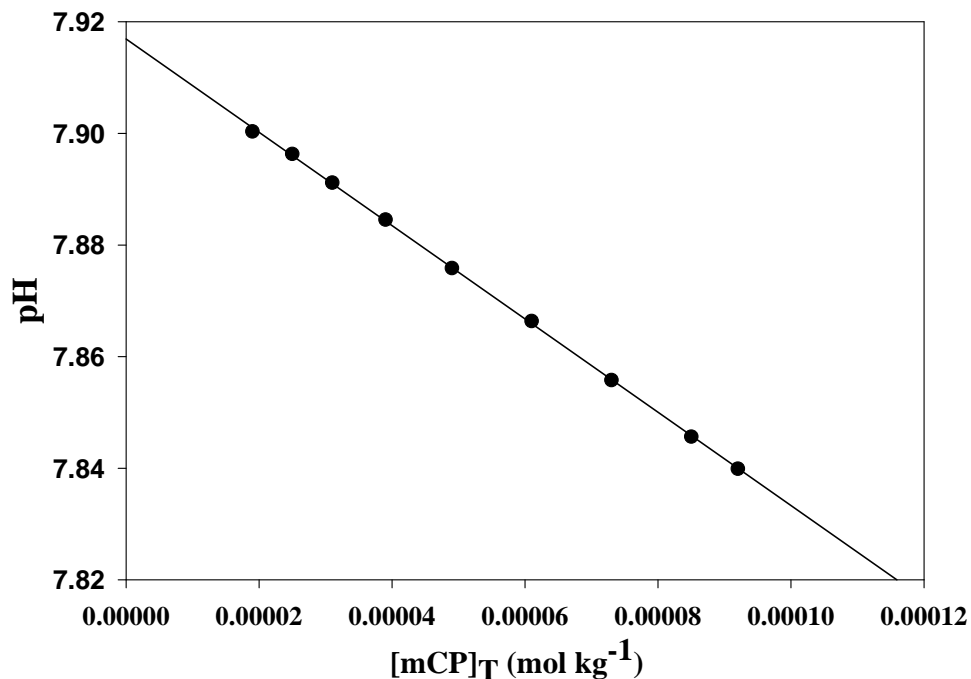
Figure 2.1.2 Plot of total indicator concentration [mCP]$_T$ versus pH for SAMI-pH data. A linear extrapolation through the data gives an R^2 value of 0.9998 with a y-intercept of 7.9169 which represents the pH when [mCP]$_T$ = 0. Figure taken from Seidel (2006).

Fig. 2.1.3 shows a schematic of the SAMI-pH. A pH measurement is carried out

as follows. First, fifty 50 μL pumps of seawater are flushed through the normally open

(NO) valve and the static mixer into the z-cell to clear out any remaining indicator from

the previous measurement so a blank measurement can be taken. Next, one 50 µL pump of indicator is injected into the seawater sample through the normally closed (NC) valve, followed by 23 pumps of seawater. The static mixer mixes the mCP indicator pump into the seawater sample, creating the absorbance plot versus time seen in Fig. 2.1.4. The first four of the 23 pulses to reach the z-cell are indicator free and are used as the measurement blank for each sample. Since there are more points in the linear range on the decreasing side of the absorbance curve (Fig. 2.1.4), these points are used to create the pH versus indicator concentration curve (Fig. 2.1.2). The SAMI-pH is calibrated by comparing the pH measured on the SAMI-pH to the pH determined by a second method or by measuring the pH of a standard on the SAMI-pH. See section 2.3 for further details.
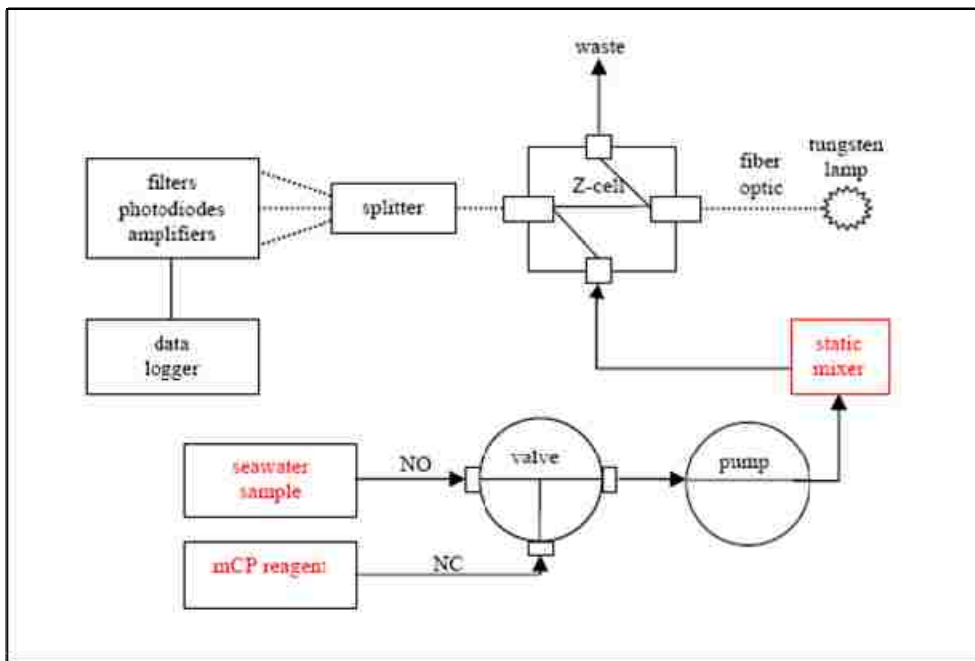
Fig. 2.1.3 Schematic for the SAMI-pH. NO and NC are the normally open and normally closed ports on the valve. The dotted lines represent fiber optics.
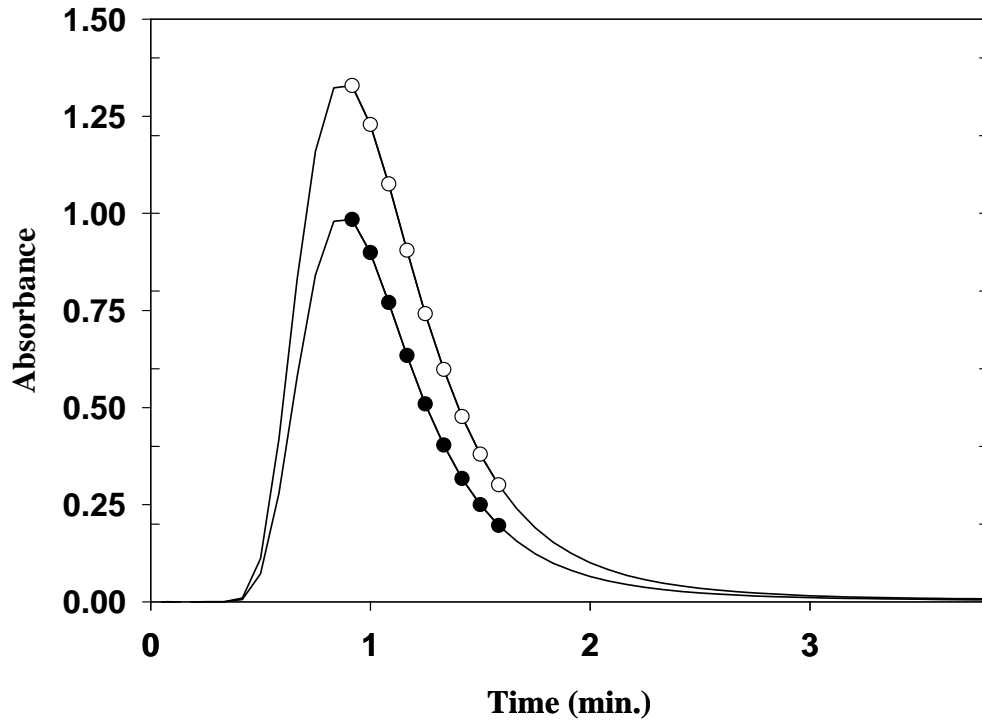
Fig. 2.1.4 Absorbance values calculated from intensity measurements taken for 50 pump pulses as the indicator slug passes through the flow cell. The filled (A_{434}) and open (A_{578}) circles shown the measurement points used for the final pH calculation. Figure taken from Seidel (2006)

2.2 Deployment Overview

Table 2.2.1 shows the deployments during this work that used a SAMI-pH.

Figures 2.2.1-2.2.6 show maps of each deployment location.

Table 2.2.1 Summary of all deployments using a SAMI-pH

Deployment	Abbreviation	Dates	SAMI-pH
Media Luna Reef, PR #1	PR#1	June-August 2007	42, 47
Media Luna Reef, PR #2	PR#2	January-March 2008	68, 47
Media Luna Reef, PR #3	PR#3	September-November 2008	68, 59
Ocean Station Papa #1	OSP#1	June 2007-March 2008	59
Ocean Station Papa #2	OSP#2	June 2008-January 2009	13
Ocean Station Papa #3	OSP#3	June 2009-October 2009	59
Monterey Bay, CA	MB	June-August 2007	13
Southern Ocean Gas Exchange Cruise, 2008	SOGasEx	March 2008	13

Fig. 2.2.1 Map of Puerto Rico. The black arrow shows the location of the La Parguera shelf reef system.
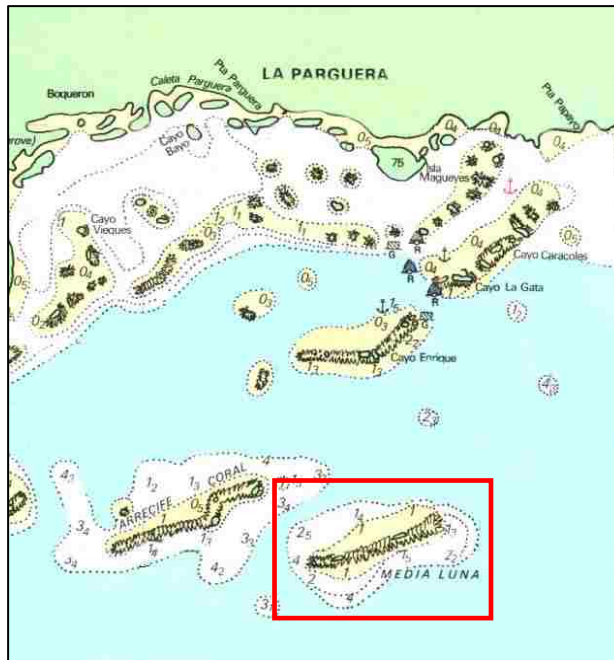
Fig. 2.2.2 Blowup of the La Parguera, PR area. The red box shows Media Luna reef and its location relative to the shoreline and other coral reefs in the area.
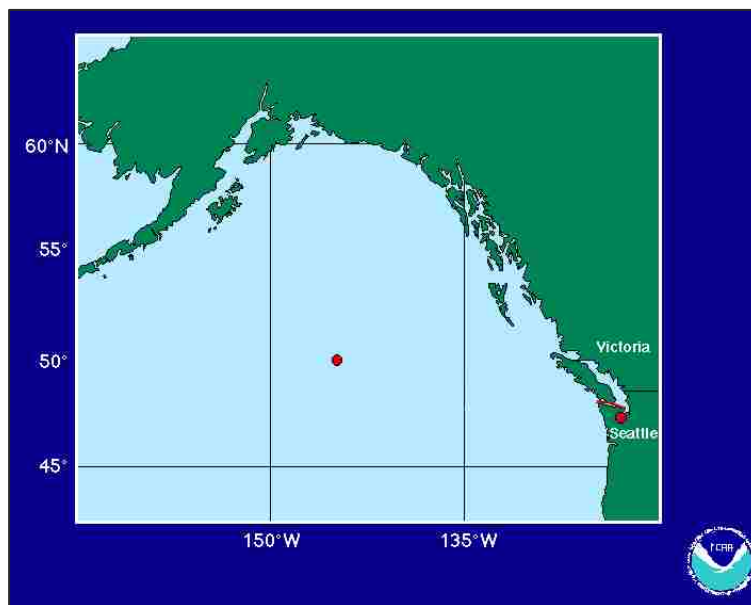
Fig. 2.2.3 Location of the Ocean Station Papa mooring in the North Pacific Ocean, shown by the red dot between 150 ^{o}W and 135 ^{o}W. Figure courtesy of NOAA.

Fig. 2.2.4 Map showing the location of Monterey Bay off the coast of California and the location of the moorings (M0, M1, M2, S2) in Monterey Bay. Figure courtesy of the Monterey Bay Aquarium Research Institute.
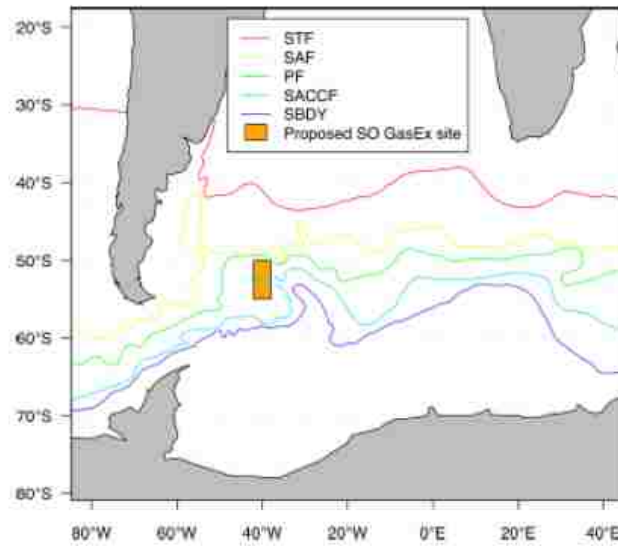
Fig. 2.2.5 Map showing the approximate location of the Southern Ocean Gas Exchange Cruise, 2008. The orange box shows the approximate cruise location off the southeastern coast of South America. Figure courtesy of the NOAA Gas Exchange Southern Ocean Cruise Report.

2.3 e-Values

Since the e-values (e_1, e_2, e_3) are used to calculate pH from SAMI-pH data (Eqn. (2.5)), they directly affect the accuracy of the SAMI-pH measurement. Molar absorptivities are dependant on the bandpass of the instrument they are measured on. The bandpass can vary slightly between SAMI-pH instruments, due to differences in the interference filters used to filter the white light source to our three measurement wavelengths. Molar absorptivities are also dependant on the pathlength of the measurement cell, which on the SAMI-pH can be slightly from instrument to instrument due to machining tolerances. Because of these differences, molar absorptivities were measured on each SAMI-pH using acidic (pH = 5.5 or 5.0) and basic (pH = 12) mCP solutions prepared according to Seidel et al. (2008). All mCP solutions were prepared from the same lot of indicator (Sigma, 11517KC) to avoid differences in impurities between lots. Molar absorptivity measurements on SAMI-pHs were carried out on the bench top unless laboratory temperature varied more than a degree throughout a day, in which case measurements were carried out in a water chamber temperature controlled to 20.0 $^{\circ}$C. Currently, the standard molar absorptivity measurements procedure uses the temperature controlled water chamber. Molar absorptivities were corrected from the average measurement temperature to 25 $^{\circ}$C using the mCP molar absorptivity temperature dependence equations determined by K. Harris (Table 2.2.1). The temperature corrected molar absorptivities were then used to calculate e-values (Eqn. 2.6). Table 2.2.1 shows the newer mCP temperature dependence equations of K. Harris and the equations determined previously by M. Seidel. The equations of K. Harris were used in this work because they were found to give more reproducible values at low

temperatures during repeated trials. The temperature dependences of the mCP indicator

were determined on the UV-VIS spectrophotometer, in order to achieve the highest

absorbance accuracy for the measurements.

Table 2.2.1 mCP molar absorptivity temperature dependence equations for correcting to
25 ^{o}C. $\varepsilon_{a\,x\,t}$ represents the molar absorptivity at the measured temperature t (^{o}C) and $\varepsilon_{a\,x}$
(25) represents the molar absorptivity at 25 ^{o}C. Both the K. Harris and M. Seidel
equations were determined from 5-25 ^{o}C.

K. Harris	M. Seidel
$\varepsilon_{a\,434\,t} = \varepsilon_{a\,434\,(25)} - 22.28\,(t\text{-}25)$	$\varepsilon_{a\,434t} = \varepsilon_{a\,434(25)} - 26\,(t\text{-}25)$
$\varepsilon_{a\,578\,t} = \varepsilon_{a\,578\,(25)} + 0.5853\,(t\text{-}25)$	$\varepsilon_{a\,578t} = \varepsilon_{a\,578(25)} + (t\text{-}25)$
$\varepsilon_{b\,434\,t} = \varepsilon_{b\,434\,(25)} + 6.326\,(t\text{-}25)$	$\varepsilon_{b\,434\,t} = \varepsilon_{b\,434\,(25)} + 12\,(t\text{-}25)$
$\varepsilon_{b\,578\,t} = \varepsilon_{b\,578\,(25)} - 99.65\,(t\text{-}25)$	$\varepsilon_{b\,578\,t} = \varepsilon_{b\,578\,(25)} - 71\,(t\text{-}25)$

Figures 2.2.1-2.2.3 show the e-values for each SAMI-pH over several different

trials. Tabulated e-value data are given in Appendix A. The e-values for SAMI-42

showed a marked difference from the other SAMI-pHs. After the Media Luna Reef PR

#1 deployment SAMI-42 never functioned correctly for pH measurements, despite

extensive troubleshooting and re-building. Systematic tests to determine if the problem

was due to the electronics or fluidics were never able to resolve the problem Lamps,

tubing, pump-valve housings/assemblies, and all electronic boards were switched out one

by one and all at once but the instrument still did not produce an accurate point pH curve.

Normal problems that cause a SAMI-pH to produce erroneous results, such as an

incorrectly assembled static mixer, silicone oil in the lines, clogged tubing, or an

electronic board problem, did not seem to be present here and replacing these parts did

not fix the problem. The specific problem was never fully diagnosed despite at least

three lab members spending numerous hours and weeks on the project, and the

instrument was eventually converted into a SAMI-CO_2. Table 2.2.2 shows the average e-

values for all SAMI-pHs for each trial. Each trial point is the average of 4 molar

absorptivity measurements. The trials were carried out before each instrument was sent

out for a field deployment and several months/years may be present between trials. See

Appendix A for exact trial dates.
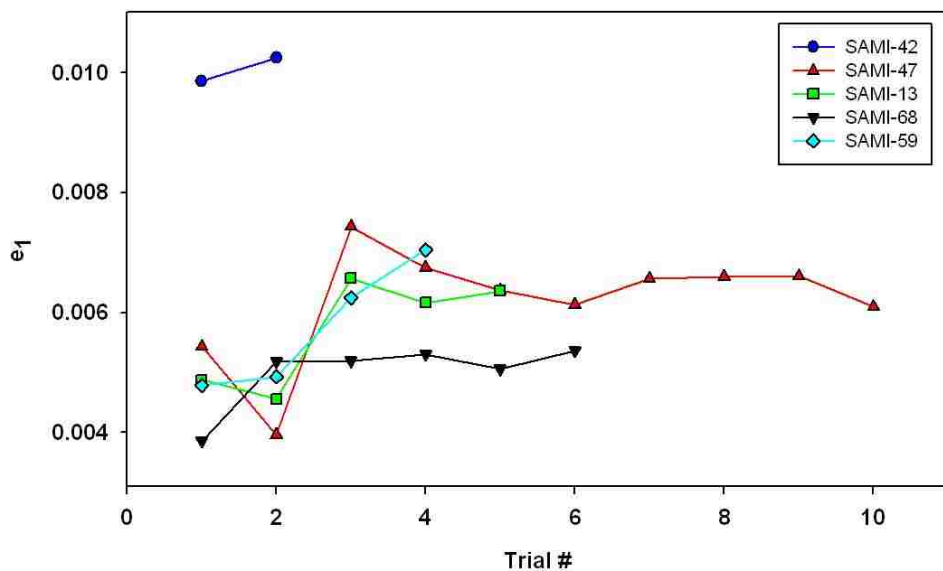
Fig. 2.2.1 e_1 values for all SAMI-pHs.
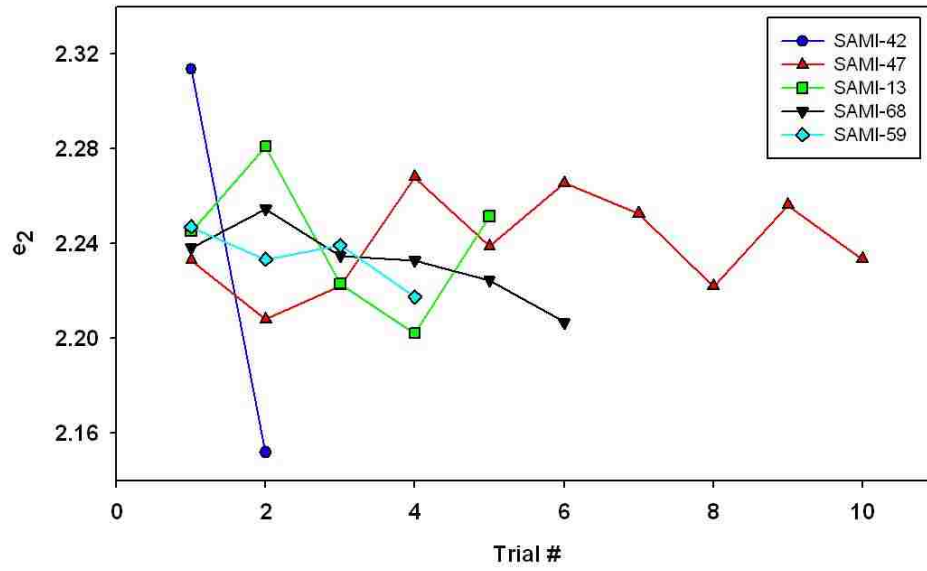
Fig. 2.2.2 e$_2$ values for all SAMI-pHs.
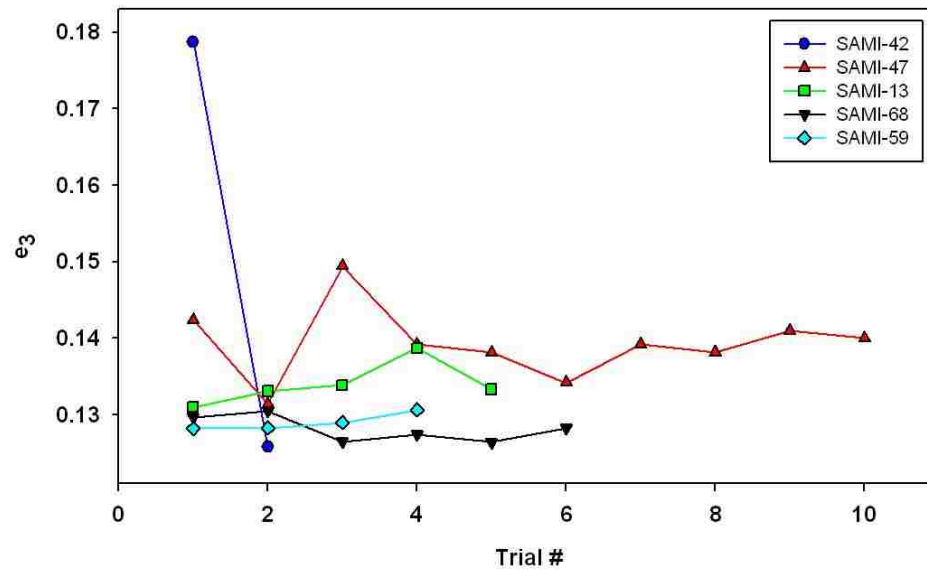
Fig. 2.2.3 e$_3$ values for all SAMI-pHs.

Table 2.2.2 Average e-values at 25 ^{o}C for all SAMIs (n=28)

	e_1	e_2	e_3
All SAMIs	0.0061 ± 0.0015	2.2368 ± 0.0293	0.1353 ± 0.0105
All SAMIs minus SAMI-42	0.0057 ± 0.0010	2.2371 ± 0.0196	0.1339 ± 0.0059

Table 2.2.3 Average molar absorptivity values at 25 ^{o}C for all SAMIs (n=28)

	$\varepsilon_{a\,434}$	$\varepsilon_{a\,578}$	$\varepsilon_{a\,578}$	$\varepsilon_{b\,578}$
All SAMIs	18147 ± 1176	109 ± 26	2452 ± 229	40581 ± 2684
All SAMIs minus SAMI-42	18150 ± 1223	104 ± 16	2428 ± 168	40602 ± 2747

One way of determining the accuracy of a SAMI-pH is to compare the pH of a seawater sample on both a SAMI-pH and on a UV-VIS spectrophotometer. Eqn. (2.5) is used to calculate the pH on both instruments so molar absorptivities must also be known for the UV-VIS. Molar absorptivities were measured on the DeGrandpre lab UV-VIS spectrophotometer at The University of Montana, and the Corredor lab UV-VIS spectrophotometer (PR UV-VIS #1 and #2) at the Magueyes Island satellite campus of the University of Puerto Rico, Mayagüez. The University of Montana UV-VIS is a Varian Cary 300 and was used to verify the accuracy of SAMI-pHs before deployment. The Puerto Rico UV-VIS is a Shimadzu UV-1601 and was used to measure the pH of discrete field samples during the three PR deployments. Tables 2.2.4 and 2.2.5 compare the new molar absorptivities and e-value measurements, respectively, with those

determined previously on the DeGrandpre lab UV-VIS spectrophotometer by Seidel

(2006). Uncertainties for the MT UV-VIS, Seidel values were not reported in Seidel

(2006). The molar absorptivities from M. Seidel were temperature corrected using the M.

Seidel temperature dependence equations. All other UV-VIS molar absorptivities were

temperature corrected using the newer temperature dependences of K. Harris (Table

2.2.1).

Table 2.2.4 Molar absorptivity values at 25 $^{\circ}$C for the UV-VIS spectrophotometers, given in kg mol^{-1} cm^{-1}.

Species	MT UV-VIS, Seidel	MT UV-VIS, Cullison	PR UV-VIS, #1	PR UV-VIS, #2
$\varepsilon_{a\ 434}$	17340	17313 ± 25	17072 ± 38	16835 ± 14
$\varepsilon_{a\ 578}$	79	90 ± 7	57 ± 5	105 ± 4
$\varepsilon_{a\ 578}$	2151	2133 ± 22	2128 ± 18	2181 ± 26
$\varepsilon_{b\ 578}$	37973	38883 ± 20	38135 ± 24	37268 ± 10

Table 2.2.5 Molar absorptivity ratios at 25 $^{\circ}$C for the UV-VIS spectrophotometers

e-value	MT UV-VIS, Seidel	MT UV-VIS, Cullison	PR UV-VIS, #1	PR UV-VIS, #2
e_1	0.0046	0.0052 ± 0.0004	0.0033 ± 0.0003	0.0062 ± 0.0002
e_2	2.1900	2.2459 ± 0.0041	2.2337 ± 0.0023	2.2137 ± 0.0021
e_2	0.1241	0.1232 ± 0.0013	0.1246 ± 0.0012	0.1296 ± 0.0015

2.3 pH Accuracy

2.3.1 Seawater Sample

At the start of this work, seawater pH standards were not commercially available.

Tris buffers, based on 2-amion-2-hydroxy-methyl-1,3-propanediol (DelValls and

Dickson, 1998) have been used historically as a secondary pH standard (Smith and Hood, 1964). However, these solutions are difficult to prepare to an accurate absolute pH. After preparation, the pH of the solution is calibrated against a hydrogen electrode (DelValls and Dickson, 1998), which is a difficult measurement that is not commonly carried out in modern laboratories. Because of the difficulties with creating a pH standard, the pH accuracy was determined by comparing the pH of a seawater sample measured on the SAMI-pH and a UV-VIS spectrophotometer. As discussed above, the UV-VIS method has been the standard method for measuring seawater pH. For accuracy measurements, a seawater sample, collected from Hood Canal, Washington, was stored in a gas-impermeable bag and measured on both instruments on the same day. The entire SAMI-pH instrument was placed in a thermostated chamber, while UV-VIS measurements were carried out in dual 10 cm jacketed cell holders (see Seidel et al., 2008 for details). The MT UV-VIS e-values determined by M. Seidel (Table 2.2.4) were found to give more consistent results between the UV-VIS and the SAMI-pHs, and were used for all pH measurements on the Montana UV-VIS spectrophotometer. The temperature correction equations of K. Harris (Table 2.2.1) were used to correct the UV-VIS and SAMI-pH measurements to an identical temperature. Figure 2.3.1 shows the accuracy results for several SAMI-pHs. Tabulated values are given in Appendix B. The average accuracy for all samples was 0.0027 ± 0.0057 (average $\pm$ standard deviation) pH units. While the spectrophotometric pH measurements on a UV-VIS have been found to be capable of a pH accuracy of 0.001-0.005 pH units (Seidel et al., 2008), it can be difficult to achieve these results. Much of the pH difference precision error (± 0.0057 pH units) (Fig. 2.3.1) comes from variation in the UV-VIS measurements, not the SAMI-pH

measurements. For example, the pH difference precision for the PR#2, SAMI-68 series in Fig. 2.3.1 is ± 0.0023 pH units. The UV-VIS and SAMI-pH precisions for this measurement were ± 0.0022 and ± 0.00092 pH units, respectively. The accuracy between the SAMI-pH and the UV-VIS can also be affected by changes in the pH of the measured sample. The seawater sample is not heavily buffered like the Tris buffers (discussed below) and even in the gas impermeable bags, can experience pH changes over time between when the sample was measured on the SAMI-pH and when it was measured on the UV-VIS. Most of the bags used for the seawater samples in Fig. 2.3.1 were ordered assembled from Pollution Management Company (PMC). While the bag material is gas impermeable, it was later discovered that the fittings holding the tubing on the bag were not being tightened enough to prevent all gas exchange. A flux of CO_2 into the bag would lead to a decreased pH of the sample. If the seawater sample were first measured on the UV-VIS and then the SAMI-pH, a decreased sample pH would could to the positive bias in pH accuracy seen in Fig. 2.3.1 (UV-VIS – SAMI-pH). If the sample were measured on the UV-VIS after the SAMI-pH, a decreased sample pH could lead to the negative bias in pH accuracy seen for three of the SAMIs in Fig. 2.3.1. Currently, bag materials are bought from PMC and the bags are assembled in the DeGrandpre lab. It is now possible to tighten the fittings with a wrench before final assembly to prevent gas exchange into or out of the bags.

2.3.2 Tris Buffer Sample

With Tris pH buffers (DelValls and Dickson, 1998) becoming commercially available, it is now possible to test the accuracy of the SAMI-pHs against a pH standard.

All Tris buffer tests used Batch 1 standards, prepared by Andrew Dickson at Scripps

Institution of Oceanography. The pH of Batch 1 Tris buffer, measured with a hydrogen

electrode system, was 8.0916 ± 0.0006 at 25 $^{\circ}$C. The pH can be calculated at other

temperatures using the equation of DelValls and Dickson (1998) and subtracting a 0.0020

pH unit correction factor from the predicted value. The Tris buffer pH value measured

with a hydrogen electrode (8.0916 pH units, from Andrew Dickson) was found to be

0.0020 pH units lower than the predicted value. The total uncertainty in the final pH of

the Tris buffer is ~0.002 pH units. Since the Tris sample is buffered, mixing mCP

indicator with Tris during a measurement does not lead to the decreasing point pH with

increasing indicator concentration seen with a seawater sample (Seidel et al., 2008).

Instead, an initial drop in point pH occurs when the mCP indicator is first mixed with the

buffer, followed by a horizontal linear section (Fig. 2.3.2).
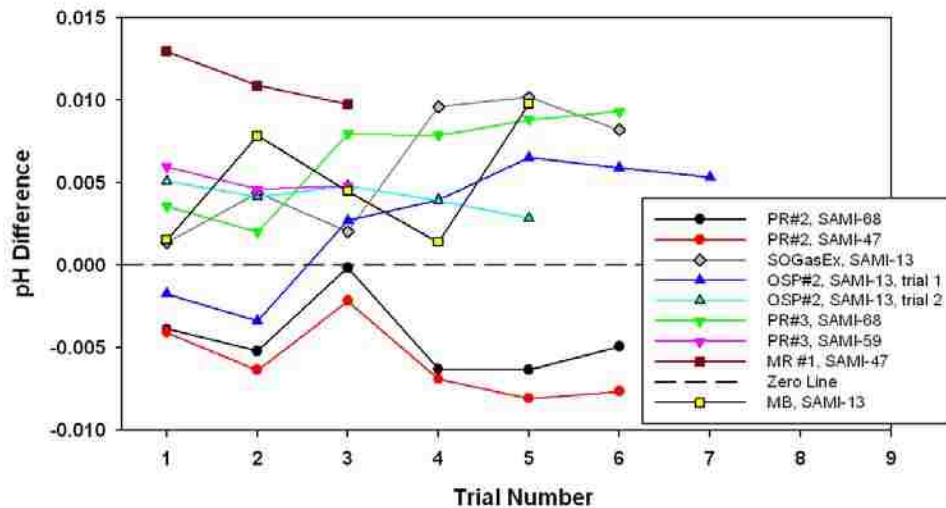
Fig. 2.3.1 Accuracy of SAMI-pHs versus the UV-VIS spectrophotometer (pH difference
= UV-VIS –SAMI-pH), measured on a seawater sample. Legend abbreviations are
explained in Table 2.2.1.

Rather than calculating pH from a linear extrapolation (Fig. 2.1.2), an average pH is taken over the linear section to calculate the final pH of a Tris buffer sample. Fig. 2.3.2 shows a typical point pH curve for a seawater sample and a Tris buffer sample. The first four pumps are used as a blank so the indicator pumps in Fig. 2.3.2 start at pump number 5. The pH of the indicator is set to 7.5 pH units and therefore should always be lower than the typical seawater pH sample (range = 7.8-8.2 pH units). As indicator is mixed with the seawater sample, the pH therefore decreases. As the indicator is then diluted with more seawater as pumping continues, the pH of the sample increases again. Only the linear portions of the curves are used in the pH calculation. For the seawater portion, points ~13-17 (Fig. 2.3.2) would be used for the linear extrapolation (Fig. 2.1.2). For the Tris buffer sample, points ~15-20 would be averaged to determine the final pH.
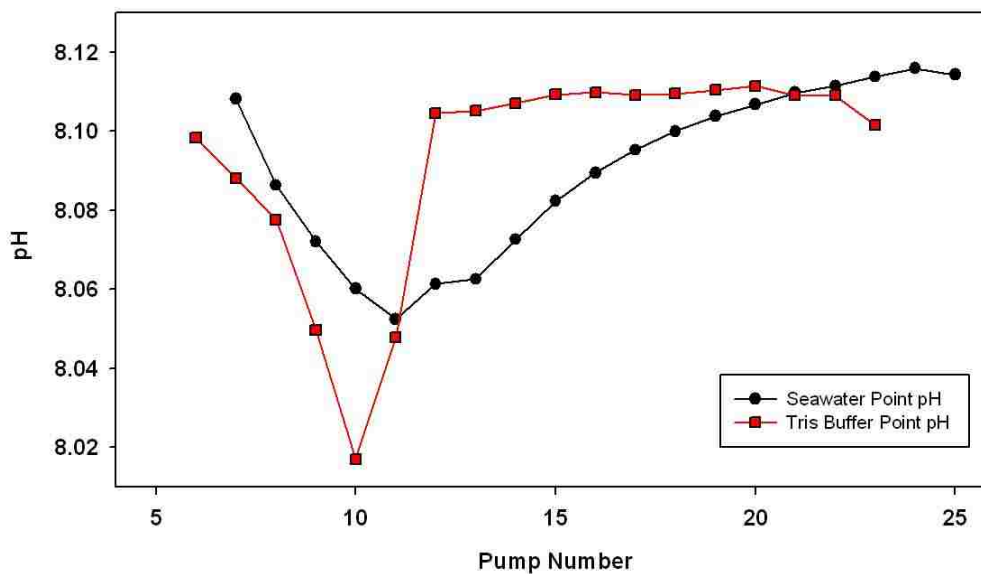
Fig. 2.3.2 SAMI-pH point pH curves for seawater and Tris buffer samples.

To measure a Tris buffer sample, both the SAMI-pH and a glass bottle containing the Tris buffer were submerged in a thermostated water bath. The pH measured on the SAMI-pH was compared to the value of the Tris buffer, calculated at the SAMI-pH measurement temperature. The pH difference (Tris – SAMI-pH) of all measured samples is shown in Fig. 2.3.3. Tabulated values are given in Appendix B. During initial Tris buffer accuracy tests, the SAMI-pH was triggered with a magnet directly after each measurement finished, rather than running the SAMI-pH on a standard measurement interval (minimum of 15 minutes), to save time. This method gave an average SAMI-pH accuracy of 0.0053 ± 0.0018 pH units. During the second Molasses Reef deployment, the SAMI-pH was left to run on a typical measurement interval of 15 or 60 minutes, which increased the accuracy of the SAMI-pH (Fig. 2.3.3). Table 2.3.1 shows the accuracy of SAMI-47 for the same bottle of Tris, with the three different measurement intervals. Both the 15 and 60 minute measurements are within the uncertainty of the Tris buffer pH calculation (0.002 pH units). As a result, 15 minutes was chosen as the acceptable interval for future Tris buffer accuracy tests, balancing measurement time with accuracy. This increase in Tris accuracy with a longer measurement interval could be due to the flow of the Tris buffer through the SAMI-pH. The Tris buffer is 'stickier' than seawater samples, which can make it more difficult to flush all of the mCP indicator-Tris buffer mix out of the flow cell between measurements. Letting the sample sit in the cell for 15 to 60 minutes could allow a steady state to be established between the flow cell and tubing material and the Tris sample, making it easier to flush the previous sample out of the cell. A future test could also involve increasing the flushing between samples to

36

remove any traces of the previous sample to potentially achieve more accurate pH

numbers without having to use a longer measurement interval.
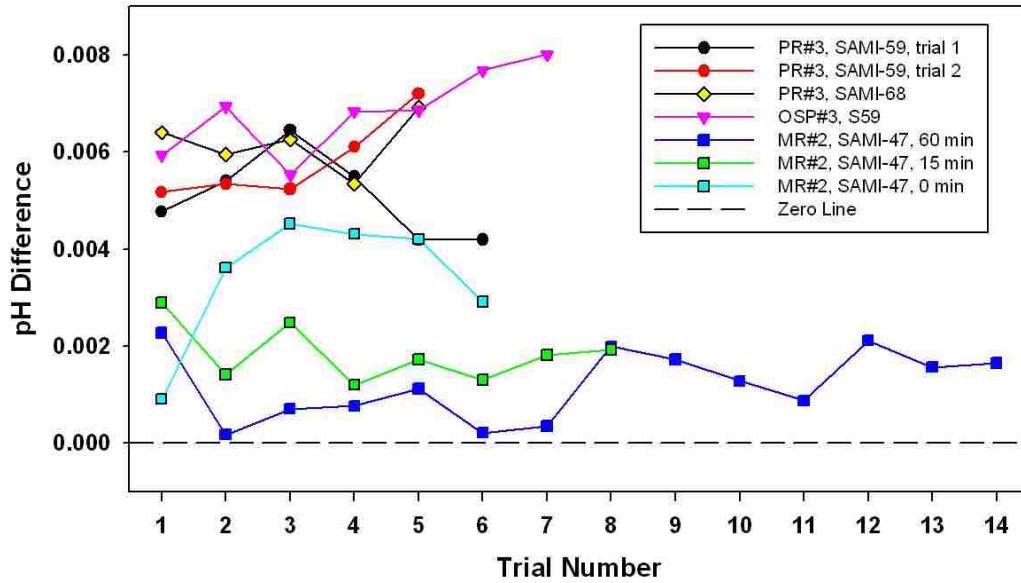
Fig. 2.3.3 pH difference between the SAMI-pH and the calculated Tris buffer standard
value (pH difference = Tris –SAMI-pH). Legend abbreviations are explained in Table
2.2.1.

Table 2.3.1 Accuracy of SAMI-47 (Molasses Reef #2 deployment) compared to Tris
buffer Batch 1, Bottle 20 on several measurement intervals.

Measurement Interval	Accuracy (Tris – SAMI-pH)
Trigger Immediately	0.0034 ± 0.0014
15 min	0.0018 ± 0.0006
60 min	0.0012 ± 0.0007

2.4 Battery Life

The battery life for each SAMI-pH deployment is shown in Fig. 2.4.1. All SAMI-pHs were the first generation design, with a two battery packs in series, each consisting of 9 D-cell batteries in parallel. In this configuration, the lower limit for battery power is 9-10 volts, below which the solenoid pumps will not work.   In Fig. 2.4.1, each battery volt series was adjusted to a common starting point of 14.0 volts. The sample number is the number of measurements collected by the SAMI-pH, which is independent of the measurement interval. Temperature ranges for each deployment site are shown in Fig. 2.4.1, with additional details for each deployment in Table 2.4.1. The change in battery volts over time was not clearly related to temperature changes between sites. The lowest temperatures were observed during the Southern Ocean Gas Exchange cruise (4-6 ^{o}C) but this battery volts curve followed the battery volt trend from several coral reef deployments with much higher temperatures (23-29 ^{o}C). The Ocean Station Papa deployments showed the next lowest temperatures at 4-13 ^{o}C and these series did show that battery volts were depleted faster in the colder water compared to the warmer deployments (Fig. 2.4.1). However, one of the warm (26-29 ^{o}C) Puerto Rico coral reef deployments also showed the battery volts being drawn down faster, making the results inconclusive.
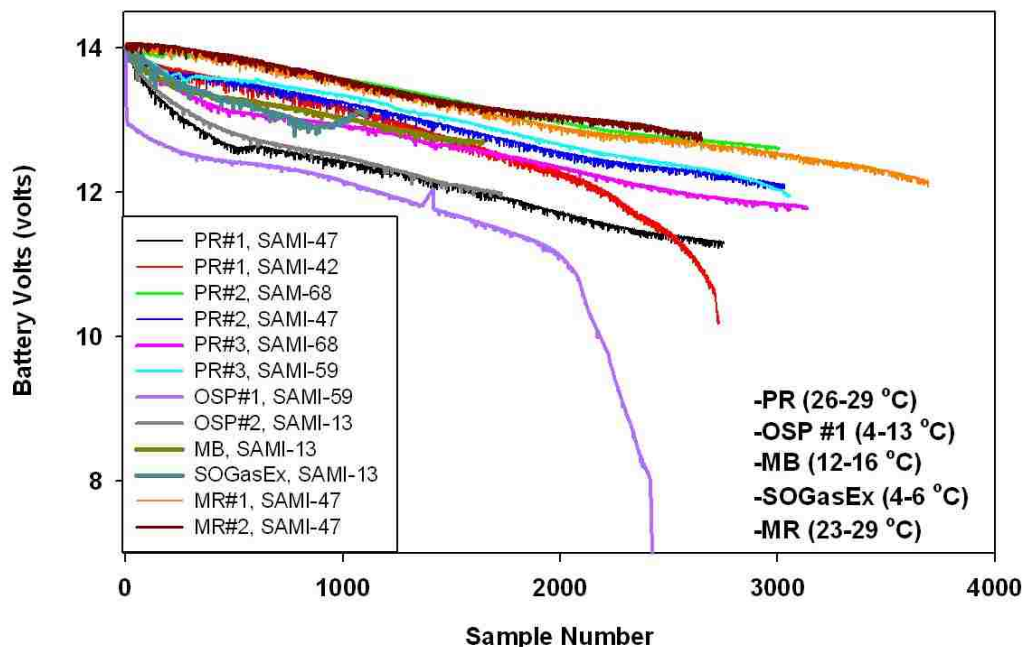
Fig. 2.4.1 Battery volts vs. sample number for each SAMI-pH, by deployment. Legend abbreviations are explained in Table 2.1.1.

Table 2.4.1 summarizes the temperature range, measurement interval, and sample number for each SAMI-pH. The PR #1 SAMIs collected fewer samples than the second and third Puerto Rico deployments because the SAMI datalogger storage capacity was exceeded before the end of the deployment. The SAMI-pH program was re-written after the first Puerto Rico deployment to store fewer bytes and avoid the problem in future deployments. The second Ocean Station Papa deployment collected fewer samples than the first Ocean Station Papa deployment because the open ocean mooring broke free from the mooring chain and was recovered early during the second deployment. There is no data from the third Ocean Station Papa deployment because the SAMI-pH belongs to collaborators at the University of Washington and the data have not yet been released.

Table 2.4.1 Summary of SAMI-pH deployment parameters related to battery life

Deployment	SAMI-pH	Temperature Range	Measurement Interval (min)	Sample Number	Final Battery Volts
Media Luna Reef, PR #1	42	28.9-30.0 ^{o}C	30	2731	9.6
Media Luna Reef, PR #1	47	28.9-30.0 ^{o}C	30	2753	12.3
Media Luna Reef, PR #2	68	25.5-27.5 ^{o}C	30	3007	11.8
Media Luna Reef, PR #2	47	25.5-27.5 ^{o}C	30	3031	11.9
Media Luna Reef, PR #3	68	27.7-30.3 ^{o}C	30	3134	11.8
Media Luna Reef, PR #3	59	27.7-30.3 ^{o}C	30	3057	11.9
Ocean Station Papa #1	59	4.4-13.3 ^{o}C	180	2376	9.3
Ocean Station Papa #2	13	6.5-13.0 ^{o}C	180	1731	12.2
Monterey Bay, CA	13	10.7-16.2 ^{o}C	60	1643	12.2
Southern Ocean Gas Exchange Cruise 2008	13	4.4-6.2 ^{o}C	60	1106	12.6

CHAPTER 3

<u>Inorganic Carbon Modeling using in situ pH Measurements</u>

<u>3.1 Abstract</u>

Autonomous pH and partial pressure of carbon dioxide (pCO_2) sensors were deployed in tandem in Monterey Bay, CA from June to August 2007. The in situ data show a high degree of short-term variability, with pH and pCO_2 changing by as much as 0.32 pH units and 240 µatm over an 18 day period, respectively, which correlates with upwelling events in the area. Our goal was to examine the utility of combining in situ pH measurements with other inorganic carbon parameters for autonomous mooring-based carbon cycle research. The pH and pCO_2 data were used to model the remaining two inorganic carbon parameters, total alkalinity (A_T) and total dissolved inorganic carbon (DIC), in addition to the calcite and aragonite saturation states. Low-pass averaged A_T and DIC calculated from pH-pCO_2 were compared to A_T calculated from salinity (A_{Tsalin}) and DIC calculated from pH-A_{Tsalin} and pCO_2-A_{Tsalin}. DIC from pH-pCO_2 was initially within 14 µmol kg^{-1} of the other calculated DIC values, while A_T from pH-pCO_2 was initially within 15 µmol kg^{-1} of A_{Tsalin}. However, the pH-pCO_2 DIC and A_T drifted apart from the other calculated values by over 150 µmol kg^{-1} throughout the 69 day deployment, potentially due to biofouling. Short-term DIC projections from the pH-A_{Tsalin} and pCO_2-A_{Tsalin} pairings were reasonable compared to nitrate values, but short-term estimates from the pH-pCO_2 pair were often much larger than the other estimates. The pH-pCO_2 pair modeled aragonite and calcite saturation to within a mean of 0.15 ± 0.01 and 0.24 ± 0.15 compared to the pCO_2-A_{Tsalin} and pH-A_{Tsalin} values, respectively, over the entire deployment. In situ pH and pCO_2 data from the Southern Ocean Gas

Exchange cruise (2008) show similar trends in short-term DIC variability from pH-pCO_2, but also found large absolute offsets that may be due to measurement inaccuracy or modeling errors. These results show that the reliability of long-term predictions of mean A_T and DIC values from pH-pCO_2 requires further research but that the pH and pCO_2 data can still provides valuable insights into data quality and calcium carbonate ($CaCO_3$) saturation states and, when paired with A_T, short-term DIC variability.

3.2 Introduction

With atmospheric and oceanic carbon dioxide (CO_2) levels continuing to rise, a thorough understanding of the marine inorganic carbon system is essential for predicting future global climate changes and ocean acidification. The inorganic carbon system can be characterized by the four main, measureable parameters: A_T, DIC, pCO_2, and pH. When two of these parameters are known, the remaining two can be calculated using the thermodynamic relationships (Millero, 1995). Previous work has focused on determining the best combination of parameters based on thermodynamic and measurement errors (Byrne, 1999; Clayton et al., 1995; Lee et al., 2000; McElligott et al., 1998; Millero, 1995). The dissociation constants of Mehrbach et al. (1973) refit by Dickson and Millero have been found to give the most consistent modeled values when compared to measured values (Lee et al., 2000) and, with the exception of pCO_2, the accuracy errors in the thermodynamic constants are lower than the accuracy errors in the experimental data (Millero, 1995). The best two parameters to measure are pCO_2 and DIC, given all measurement and thermodynamic errors, but the pH-DIC, pH-A_T and pCO_2-A_T combinations also produce acceptable results (Millero, 1995). pH-pCO_2 and A_T-DIC are

the worst pairings due to the direct relationship between these measured parameters, with the pH-pCO$_2$ combination producing the largest errors in the modeled data.

Ideally, all four parameters would be measured on moorings and autonomous platforms, however pCO$_2$ and pH are the only inorganic carbon parameters for which in situ sensors are available (DeGrandpre et al., 1995; Friederich et al., 1995; Hood et al., 1999; Mackey et al., 1989; Wootton et al., 2008). Past studies have used potentiometric pH sensors for this measurement (Mackey et al., 1989; Wootton et al., 2008), which can suffer from large systematic errors due to electrode drift, susceptibility to electromagnetic interference and problems with the reference electrode (Dickson, 1993). Spectrophotometric pH techniques are now available (Byrne and Breland, 1989) and provide the needed 0.002 pH unit accuracy for inorganic carbon modeling (Seidel et al., 2008). Previous work to develop an in situ indicator-based pH sensor has produced high power instruments that can be deployed for short intervals (hours to days) only (Liu et al., 2006; Nakano et al., 2006). While autonomous systems for DIC and A$_T$ are still in the development stages (Martz et al., 2006; Sayles and Eck, 2009), the Submersible Autonomous Moored Instrument for pH (SAMI-pH), a fully autonomous, in situ, spectrophotometric pH sensor, has recently been developed (Martz et al., 2003; Seidel et al., 2008). Consequently, two accurate inorganic carbon parameter sensors can now be deployed together for extended periods to evaluate the potential for autonomous characterization of the inorganic carbon system.

As stated above, however, the pH-pCO$_2$ pair is the worst combination of parameters. It is commonly stated that this is because the pH and pCO$_2$ are highly correlated. This can be more clearly understood by looking at the relationships between

A_T, DIC, pCO_2 and pH. DIC is defined in Eqn. (3.1). At the average seawater pH (8.0),

approximately 90% of the inorganic carbon is present as HCO_3^-. Simplifying Eqn. (3.1)

to DIC $\approx HCO_3^-$ and using the inorganic carbon equilibrium expressions, it can be seen

that pH and pCO_2 are directly proportional to each other for a given DIC (Eqn. (3.2)),

where K_0 and K_1 represent the equilibrium constants for carbonic acid (Eqns. (3.4-3.5)).

Any small changes in either pH or pCO_2 that are not mirrored by the other parameter will

lead to compounding large errors in the modeled DIC (Dickson and Riley, 1978). Using

the same assumption that DIC $\approx HCO_3^-$, Eqn. (3.3) shows that modeled DIC is less

sensitive to errors in the measured parameters when the pH-A_T combination is used. This

is because errors in $[H^+]$ are offset by its presence in both the numerator and the

denominator. K_2 represents the second dissociation constant for carbonic acid (Eqn.

(3.6)).

$$DIC = [H_2CO_3^*] + [HCO_3^-] + [CO_3^{2-}] \tag{3.1}$$

$$DIC \approx \frac{K_1 K_0 pCO_2}{[H^+]} \tag{3.2}$$

$$DIC \approx \frac{(A_T - \text{other acids and bases})\,[H^+]}{[H^+] + 2K_2} \tag{3.3}$$

$$K_0 = \frac{[H_2CO_3^*]}{pCO_2} \tag{3.4}$$

$$K_1 = \frac{[H^+][HCO_3^-]}{[H_2CO_3^*]} \tag{3.5}$$

$$K_2 = \frac{[H^+][CO_3^{2-}]}{[HCO_3^-]} \tag{3.6}$$

The CO2SYS modeling program (Pierrot et al., 2006) can be used to numerically illustrate the DIC errors that are produced from various measurement inputs. pH and pCO_2 with precisions of ±0.002 pH units and ±2 µatm, respectively, generate random DIC errors of ±35 µmol kg^{-1} while pH and A_T inputs with precisions of ±0.002 pH units and ±2 µmol kg^{-1}, respectively, produce DIC errors of ±5 µmol kg^{-1}. These numbers indicate that at typical measurement uncertainties, the pH-pCO_2 pair produces modeled DIC with errors much larger than the current DIC measurement error (±2 µmol kg^{-1}) (Millero, 1995). The pH and pCO_2 precisions would need to be ±0.0001 pH units and ±0.125 µatm, respectively, to achieve a modeled DIC precision of ±2 µmol kg^{-1}. Since these are random errors, more precise DIC estimates may be possible through signal averaging.

Here, a LI-COR-based CO_2 system (Friederich et al., 1995) and a SAMI-pH were deployed in Monterey Bay, CA, representing one of the first times that two autonomous, in situ sensors for carbonate parameters have been deployed in tandem. In previous work, spectrophotometric pH and pCO_2 sensors were deployed together on a vertical profiler over a 14 day period (Nakano et al., 2006). This work presents a unique opportunity to evaluate the utility of combining pH and pCO_2 data from continuous, in situ sensors for inorganic carbon modeling, acknowledging the problems with the pH-pCO_2 combination as well as the lack of long-term, continuous A_T and DIC data worldwide. A SAMI-CO_2 (DeGrandpre et al., 1995) and a SAMI-pH were also deployed in tandem in the Southern Ocean in February 2008, and these results are compared with the Monterey Bay data set.

3.3 Methods

3.3.1 Monterey Bay Deployment

As part of an ongoing monitoring program run by the Monterey Bay Aquarium Research Institute (MBARI) in Moss Landing, CA, numerous sensors were deployed on the M0 buoy in Monterey Bay (36.83^o N, 121.90^o W, M0 buoy) from June 21 to August 28, 2007 at a depth of 1 meter. The M0 buoy is equipped with meteorological sensors for wind speed, wind direction and temperature, as well as in situ sensors for salinity, nitrate and pCO_2. Nitrate was measured using an in situ ultraviolet spectrophotometer (ISUS) sensor capable of an accuracy of 1.5 µM $\pm$ 0.5 µM (Johnson and Coletti, 2002). pCO_2 was measured with a LI-COR brand non-dispersive infrared analyzer adapted for mooring use (Friederich et al., 1995). This system measures absolute pCO_2 and was calibrated before deployment with CO_2 standards. Atmospheric CO_2 measurements were collected during periods of onshore winds and compared to the in situ atmospheric LI-COR measurements as an accuracy check throughout the deployment. The estimated uncertainty of this system is ± 2 µatm (Friederich et al., 2002). A SAMI-pH (Seidel et al., 2008) was added to the buoy for this deployment. The SAMI-pH is based on the spectrophotometric pH method using metacresol purple indicator (Clayton and Byrne, 1993). The recorded pH is on the total hydrogen ion scale and has been shown to be thermodynamically consistent with the other measurable CO_2 parameters (Byrne, 1999). The SAMI-pH is currently the only instrument capable of long-term, autonomous, in situ indicator-based pH measurements. Prior to this study, the SAMI-pH had been deployed only once, for an instrument validation test (Seidel et al., 2008). In addition to containing the longest in situ spectrophotometric pH dataset published to date (1581 measurements

over 69 days), this study was the first to use the SAMI-pH data to understand inorganic carbon dynamics. The SAMI-pH is capable of an accuracy of 0.0017 ± 0.0007 pH units. Salinity, nitrate, $p\mathrm{CO}_2$ and pH were measured nearly hourly and interpolated at 1 sample/hour using the interp1 function in MATLab. No discrete samples were collected during the study period.

The 6 hour upwelling index from the National Oceanic and Atmospheric Administration (NOAA) Southwest Fisheries Science Center (36° N, 122° W) was used to determine upwelling periods. All modeling of inorganic carbon parameters was done in CO2SYS (Pierrot et al., 2006) on the total pH scale with K_1 and K_2 from Mehrbach et al. (1973), refit by Dickson and Millero (1987) and $KHSO_4$ from Dickson (1990). A_T was also modeled from an A_T-salinity relationship ($A_{T salin}$) derived for California coastal waters ($2150+44*(salinity-31.25)$) (Seidel et al., 2008) using surface $p\mathrm{CO}_2$ and DIC measurements.

3.3.2 Southern Ocean Deployment

We used data from another field study, the Southern Ocean Gas Exchange Experiment, for comparison with the Monterey Bay data set. A NOAA/PMEL built $MAPCO_2$ buoy was deployed from the R.V. Ronald H. Brown at 50.35^{o} S, 38.40^{o} W on March 8, 2008 after the injection of a ^{3}He/SF$_6$ tracer patch. The buoy contained a SAMI-pH and a SAMI-CO_2 at depths of 1 m and 5 m, respectively, as well as a SeaBird 37 Microcat Conductivity Temperature Depth (CTD) sensor at 1 m. The SAMI-pH, SAMI-CO_2, and SeaBird sensor measured at 1 hour, 30 minute and 15 minute intervals, respectively. The $MAPCO_2$ buoy was removed from the water from March 12 to March

13 for instrument reconfiguration, from March 18 to March 21 for establishment of a new tracer patch after rough weather and on March 31 at the end of the cruise. Continuous shipboard pCO_2 measurements were performed using a headspace equilibrator and a LI-COR analyzer (Wanninkhof and Thoning, 1993). The SAMI-CO_2 agreed well with the shipboard pCO_2 after a -4 μatm offset was applied to the SAMI-CO_2 data and this offset was applied throughout. Discrete samples for DIC and A_T were collected during CTD casts, which were performed every 12 hours while the ship was in the tracer patch. DIC measurements were carried out using coulometry, following the DOE Handbook standard method ($\pm$1.5 μmol kg^{-1}) (Dickson et al., 2007). The system was standardized every 24 samples to certified reference materials (CRMs) (Dickson et al., 2003). A_T measurements were performed using potentiometric titrations (Dickson et al., 2003) with CRMs analyzed every 24 samples, yielding a precision of 2.5 μmol kg^{-1}. Discrete samples from the upper 10 m of the water column, which was well mixed, were used in this work. For continuous DIC modeling with pH-$A_{Tdiscrete}$ and pCO_2-$A_{Tdiscrete}$, the discrete alkalinity samples were interpolated to a 30 minute interval. All modeling was done in CO2SYS (Pierrot et al., 2006) on the total pH scale with K_1 and K_2 from Mehrbach et al. (1973), refit by Dickson and Millero (1987) and KHSO$_4$ from Dickson (1990).

3.4 Results and Discussion-Monterey Bay

3.4.1 Data Overview

The data from Monterey Bay are shown in Fig. 3.4.1. The pH and pCO_2 ranged from 7.93-8.37 pH units and 150-533 μatm, respectively, with temperature and salinity

ranges of 10.7-16.2 $^{\circ}$C and 33.5-34.0, respectively. The average 30-hour low-pass

filtered atmospheric CO_2, measured on the M0 buoy, was 389 μatm $\pm$ 3 μatm. Low-pass

filtering was done in MATLab using the filtfilt function. The coastal M0 buoy site is

located in an upwelling shadow that receives advected water from the Point Año Nuevo

upwelling center to the northwest. Point Año Nuevo experiences frequent upwelling

events in the spring and summer (Skogsberg, 1936; Skogsberg and Phelps, 1946) and

these events drive large changes in pH and pCO$_2$ (Friederich et al., 2002). This

upwelling is controlled by Ekman transport where equatorward wind stress displaces

surface water. The displaced water is replaced by deep water which is high in CO_2 and

nutrients since it originates below the photic zone, where respiration drives up CO_2 and

lowers pH. Even during strong upwelling periods, pCO$_2$ at this site was typically

undersaturated with respect to atmospheric values (Fig. 3.4.1). Water in the upwelling

shadow can have residence times that exceed the nutrient removal time, leading to

decreased production (Graham and Largier, 1997) and undersaturated pCO$_2$ values.

There was a weak but significant correlation between upwelling index and pH and pCO$_2$

(Fig. 3.4.1C). The upwelling index is a measure of how much upwelling is occurring,

with higher values indicating more upwelling. It is calculated based on Ekman's theory

of mass transport due to wind stress. Ekman mass transport is defined as the wind stress

divided by the Coriolis parameter (a function of the earth's rotation and latitude). When

the upwelling index was high (>100), the maximum negative correlation between

upwelling and pH was found with a 2 day lag in the pH data (R^2=0.0722, p<0.004 one-

tail, n=99), however, the correlation was still significant with no lag (R^2=0.0400, p<0.02).

This lag is expected since the upwelling index is based on measurements of wind stress,

not actual water mass changes. When wind stress is higher, a larger deep-water mass is upwelled and this upwelling cannot occur instantaneously. In addition, time is needed for the upwelled water to migrate from Point Año Nuevo to the M0 buoy. When the upwelling index was low (<100) there was no significant time lag between upwelling index and pH (R^2=0.0483, p<0.002 one-tail, n=192). Similar time lags were found for the correlation between nitrate and upwelling index.

The measured pH and pCO$_2$ are inversely and nonlinearly correlated, as shown in Fig. 3.4.2 (R^2=0.9890, 2nd order polynomial). The scatter in the data shows the changes in the pH-pCO$_2$ relationship over the temperature range, 11-16 ^{o}C, as well as the times when pH and pCO$_2$ were not directly correlated. To help understand the origin of this correlation, the pH and pCO$_2$ data were also modeled in CO2SYS using temperature, Redfield, calcification/dissolution and dilution relationships. The temperature dependence was examined by varying temperature over the deployment range, 11-16 ^{o}C, with a constant DIC and A_T, the Redfield relationship varied DIC and A_T by -106:18, the calcification/dissolution relationship varied DIC and A_T by 1:2 and the dilution relationship reduced DIC and A_T by 1:1. The initial DIC and A_T were selected based on the beginning values on June 21, 2007, as shown below, with DIC=2032 μmol kg^{-1} and A_T=2254 μmol kg^{-1}. The Redfield, calcification/dissolution and dilution curves were modeled at a constant temperature of 14 ^{o}C. The temperature model matches the shape of the field data and the curve shifts left and right depending on production and respiration (Redfield relationship). The Redfield ratio model created at the average deployment temperature (14 ^{o}C) (Fig. 3.4.2) also matches the shape of the field data. The Redfield

curve shifts left and right if different average temperatures are used, with decreased temperatures leading to lower pCO$_2$/higher pH values.

From Fig. 3.4.2, it can be seen that biological production, calcification/dissolution and dilution lead to changes that are very difficult to discern from temperature changes. The calcification curve shows the largest departure from the field data but the difference is small considering the very large changes in A$_T$ and DIC used in this calculation. In contrast, if pH and DIC are used for modeling, only pH varies with temperature and processes such as biological production are readily discerned from this variability. **3.4.2**

A$_T$ and DIC modeling

As expected, we found short-term changes in the unfiltered pH-pCO$_2$ derived A$_T$ and DIC that were unreasonably large, with variations in A$_T$ and DIC of 264 µmol kg^{-1} hour^{-1} and 248 µmol kg^{-1} hour^{-1}, respectively, as highlighted in Fig. 3.4.3. Small measurement uncertainties can lead to large A$_T$ and DIC errors, with temporal and spatial measurement mismatches amplifying these errors. Large spikes in DIC and A$_T$ appear to occur when pH and pCO$_2$ are not correlated or when pH and pCO$_2$ change rapidly (Fig. 3.4.3). Breakdowns in the correlation between pH and pCO$_2$ can be caused by time response and water mass offsets between the two instruments.
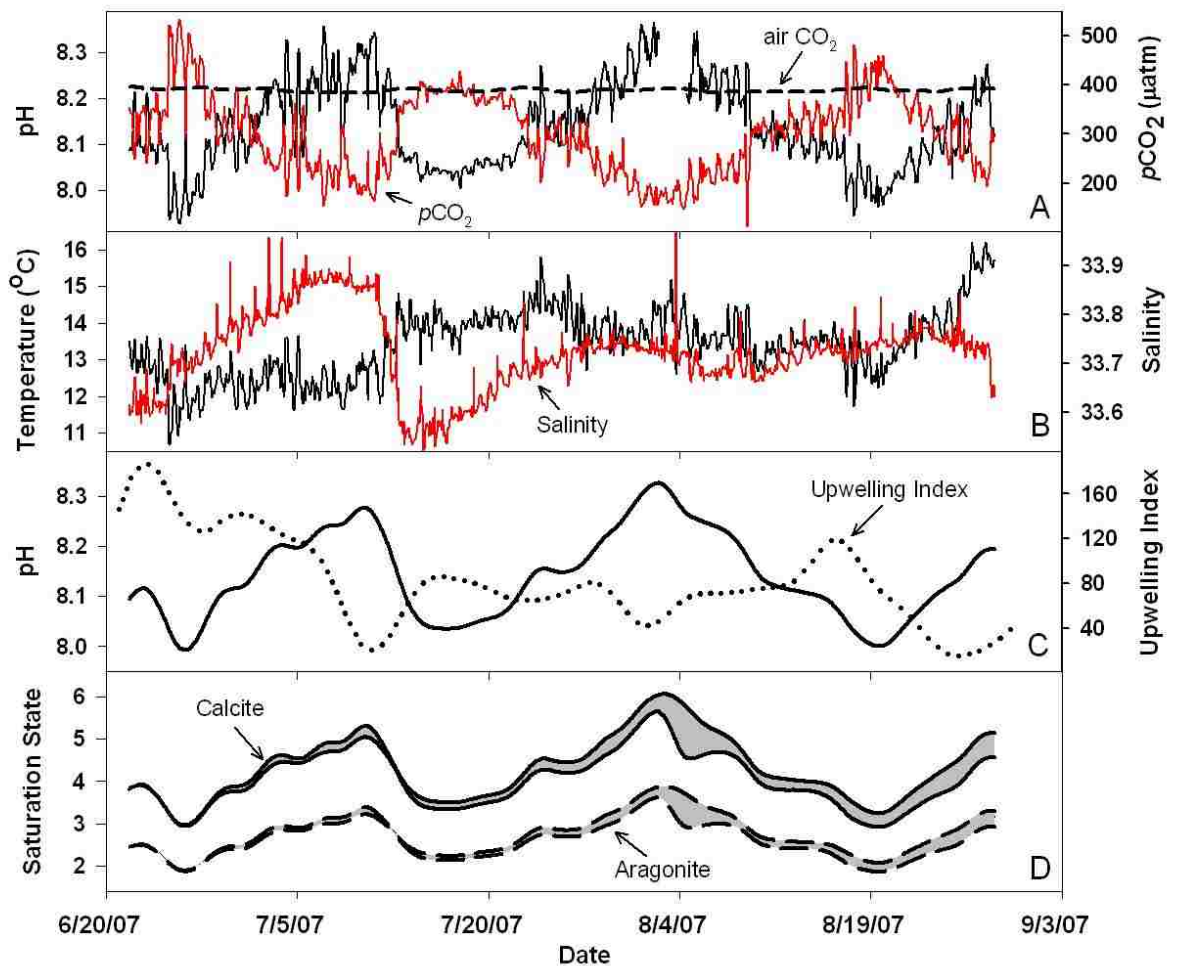
Fig. 3.4.1 (A) pH (solid black) from the SAMI-pH and pCO$_2$ (solid red) and atmospheric CO$_2$ (dashed black) from the non-dispersive infrared analyzer on M0. The gap in pH data is due to clogging of the SAMI-pH inlet, which later cleared. (B) Temperature (black) from the SAMI-pH and salinity (red) from M0. (C) 30 hour low-pass filtered pH (solid black) and upwelling index (dotted black) from the NOAA Southwest Fisheries Science Center (10 hour filter). A larger upwelling index indicates that stronger upwelling is occurring. (D) Aragonite (dashed black) and calcite (solid black) saturation states modeled in CO2SYS. The shaded region represents the uncertainty generated by using the pH-pCO$_2$ data (lower line for both saturation states) versus the pCO$_2$-A$_{Tsalin}$ data (upper line for both saturation states) for modeling. Aragonite and calcite are the two biogenic mineral forms of calcium carbonate (CaCO$_3$).
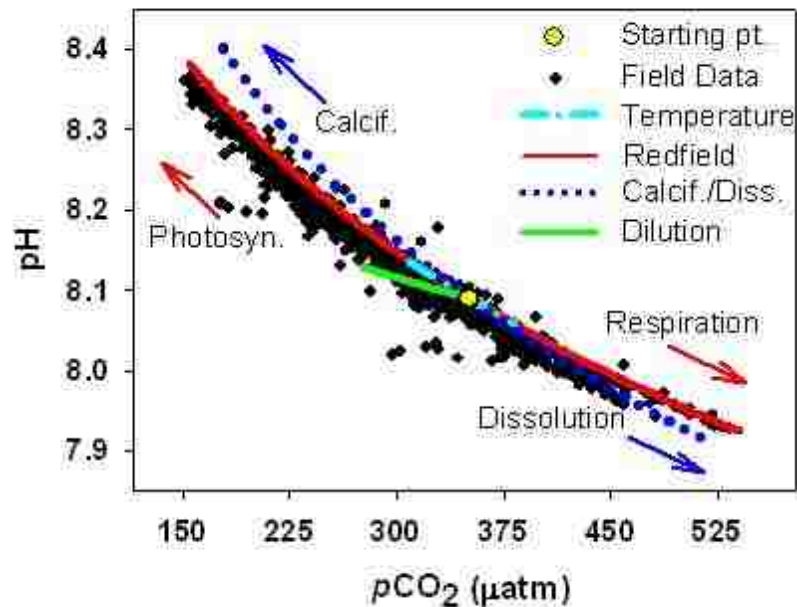
Fig. 3.4.2. Correlations of pH and pCO_2 for field data and different modeled processes. (Black circles) Field data (Fig. 3.4.1) (R^2=0.9890); (Solid red) DIC and A_T are varied by the Redfield ratio, -106:18 (temperature=14.0 °C); (Dotted blue) DIC and A_T are varied by 1:2, which is indicative of calcification (temperature=14.0 °C); (Dashed/dotted light blue) DIC and A_T are held constant (DIC = 2032 μmol kg^{-1}, A_T = 2254 μmol kg^{-1}) and temperature is varied (from 11-16 °C); (Solid green) A_T and DIC are reduced by dilution, 1:1 (starting at DIC = 2032 μmol kg^{-1}, A_T = 2254 μmol kg^{-1}). For all modeled correlations, salinity=33.7.

A 4-hour low-pass filter was applied to the pH and pCO_2 data before modeling to reduce

time response and water mass errors between the instruments (Fig. 3.4.3 and 3.4.4). A

low-pass filter keeps all of the data that is at a frequency higher than the specified value

(4 hours in this case). The 4-hour low-pass filter reduced the magnitude of the A_T and

DIC spikes by approximately 100 μmol kg^{-1}, leaving diel A_T and DIC changes that were

generally ≤50 μmol kg^{-1}. The remaining variability in the modeled data is similar to the

results of Johnson (2010), who reported short-term DIC changes up to ~50 μmol kg^{-1}

during the 2006 upwelling season at the M1 buoy located at 36.75°N, 122.03°W in

Monterey Bay. Johnson (2010) used measured pCO_2 and a salinity-derived A_T to model DIC. These data show that 4-hour low-pass filtered pH-pCO_2 data may predict reasonable short-term DIC and A_T variability. The validity of these calculations is examined in further detail below, in comparison with nitrate data.
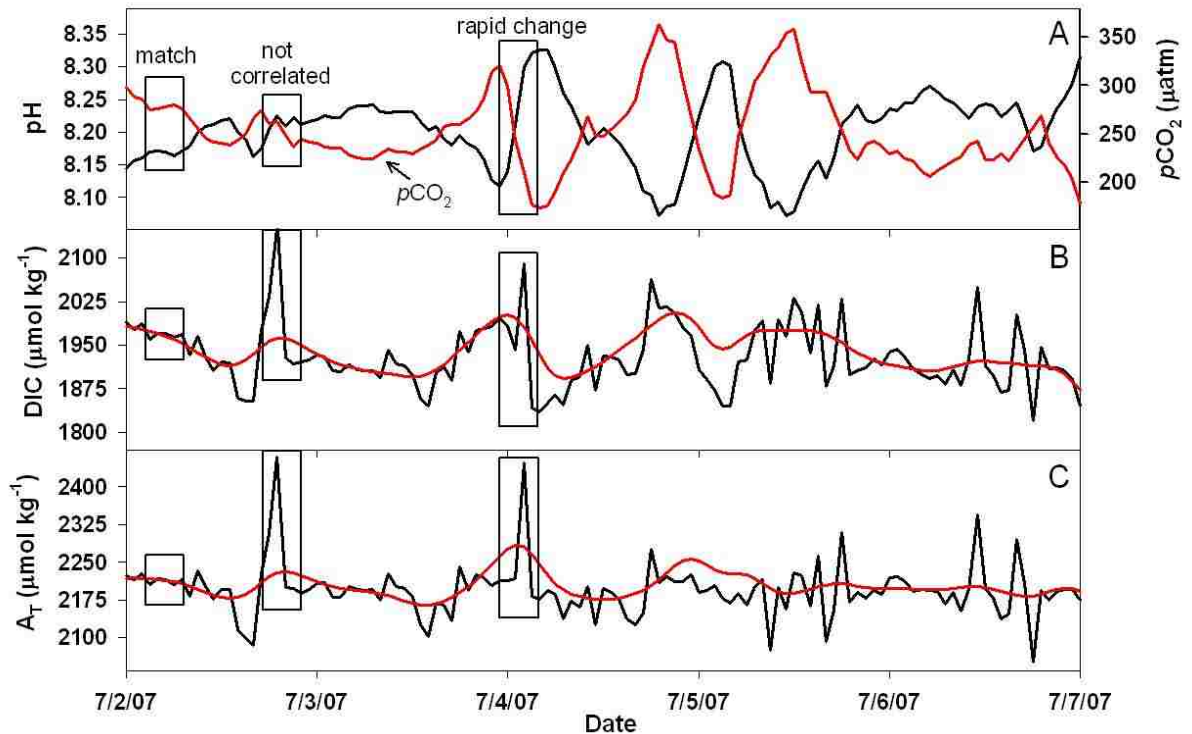
Fig. 3.4.3. Short-term changes in pH, pCO_2 and calculated DIC and A_T. (A) Monterey Bay pH (black) and pCO_2 (red). (B) Unfiltered (black) and 4-hour low-pass filtered (red) pH-pCO_2 derived DIC. (C) Unfiltered (black) and 4-hour low-pass filtered (red) pH-pCO_2 derived A_T. The large spikes in unfiltered DIC and A_T correspond to times when the pH and pCO_2 data do not show a direct inverse relationship or are changing rapidly over time.

To examine longer-term variability in the data, a 30-hour low-pass filter was applied to the pH and pCO_2 before they were used to model A_T and DIC. Since no independent measurements of A_T or DIC were made, we used DIC calculated from A_{Tsalin} and either pH or pCO_2 for comparison (Fig. 3.4.4B). The pH-pCO_2 derived A_T matches

the A_{Tsalin} to within 17 μmol kg^{-1} for the first 7 days of the deployment with an initial difference of 15 μmol kg^{-1} (starting A_T = 2269 μmol kg^{-1}) (Fig. 3.4.4A). After this time, the pH-pCO_2 A_T slowly drifts below the A_{Tsalin}, with a final difference of 158 μmol kg^{-1} (ending A_T = 2100 μmol kg^{-1}, ± 48 μmol kg^{-1}). The maximum difference between the pH-pCO_2 modeled DIC and the DIC derived from pH/A_{Tsalin} and pCO_2/A_{Tsalin} is 16 μmol kg^{-1} for the first 7 days of the deployment with an initial difference of 14 μmol kg^{-1} (starting DIC = 2046 μmol kg^{-1}) (Fig. 3.4.4B). As with the A_T data, the DIC modeled from pH-pCO_2 begins to drift away from the pH-A_{Tsalin} and pCO_2-A_{Tsalin} derived DIC after this time, with an offset of 150 μmol kg^{-1} by the end of the 69 day deployment (final DIC = 1824 μmol kg^{-1}, ± 63 μmol kg^{-1}).

The large downward trends in the pH-pCO_2 modeled A_T and DIC are not realistic for this site. A simultaneous decrease in A_T and DIC could only occur through calcification, dilution or advection of lower salinity water. The A_T in California coastal waters has been shown to be conservative with salinity (G. Friederich, pers. comm., 2006) and our modeled pCO_2 data (below, Fig. 3.4.5B) did not indicate that any calcification is occurring at this site and thus changing the salinity-A_T relationship substantially. There is also no significant trend in salinity (Fig. 3.4.1) to indicate dilution or freshwater movement.
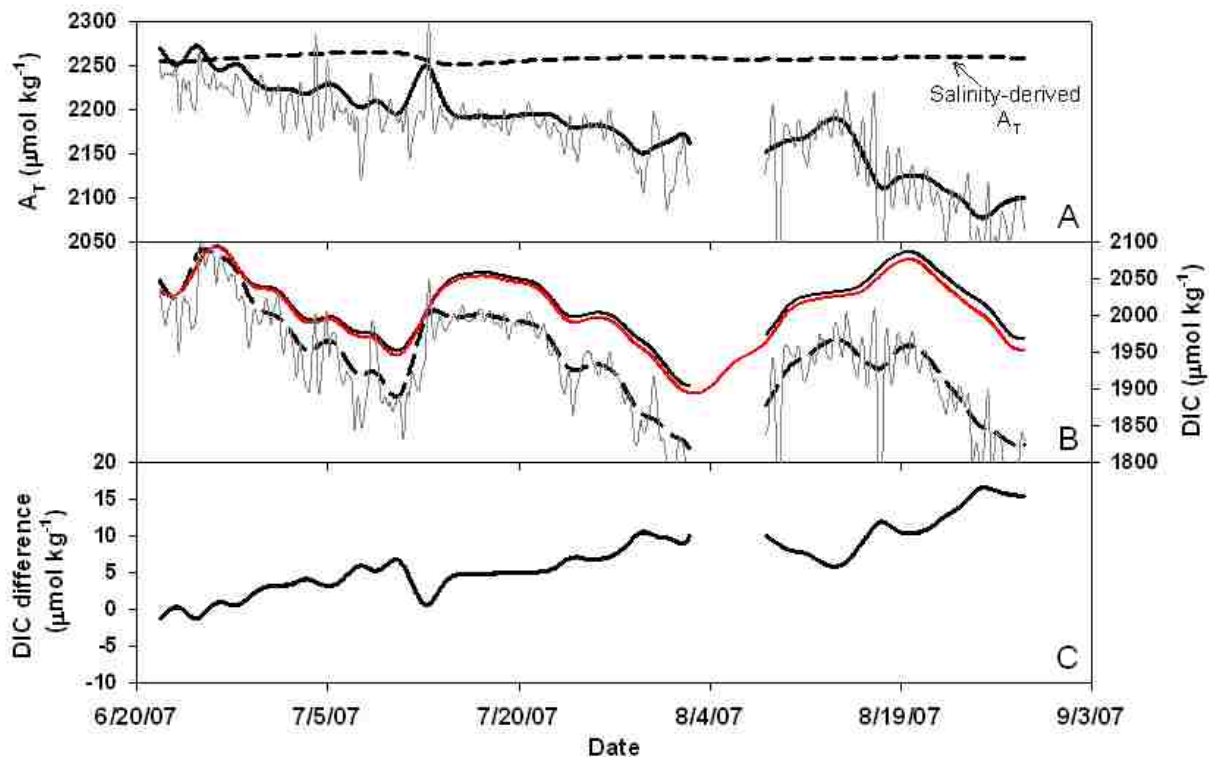
Fig. 3.4.4. (A) A_T modeled from 4-hour low-pass filtered pH-pCO$_2$ (solid gray), 30-hour low-pass filtered pH-pCO$_2$ (solid black)and an A_{Tsalin} relationship for California coastal waters (dashed black) (Seidel et al., 2008). (B) DIC modeled from 4-hour low-pass filtered pH-pCO$_2$ (solid gray) and 30-hour low-pass filtered pH-pCO$_2$ (dashed black), pH-A_{Tsalin} (solid black), and pCO$_2$-A_{Tsalin} (solid red). (C) DIC difference between pH-A_{Tsalin} derived DIC and pCO$_2$-A_{Tsalin} derived DIC for the data in 4B. The gaps in the data correspond to when the SAMI-pH inlet tubing was clogged.

The salinity-derived A_T and DIC more likely represent the typical range of these parameters in nearshore Monterey Bay (Fig 3.4.4). The pH-A_{Tsalin} and pCO$_2$-A_{Tsalin} modeled DIC ranges, 1893-2090 µmol kg^{-1}, are lower than nearshore discrete DIC values measured by Friederich et al. (2002) during the spring of 1997 in Monterey Bay (2100-2130 µmol kg^1). However, the discrete pCO$_2$ values observed by Friederich et al. (2002) were also higher (650 µatm) than our observed pCO$_2$ range (150-533 µatm). Johnson

(2010) has reported modeled DIC values (from measured pCO_2 and A_{Tsalin}) further offshore at the M1 buoy that ranged from 1900-2200 $\mu mol\ kg^{-1}$ for June-August, 2006.

While the unfiltered pH-pCO_2 data showed deviations from the A_{Tsalin} derived DIC even early on, the heavily filtered data were much closer during the first week of the deployment (16 $\mu mol\ kg^{-1}$). The downward drift in the pH-pCO_2 derived A_T and DIC data over time is likely due to photosynthesis from the heavy macroalgae fouling around the instruments, causing higher pH, lower pCO_2 values. For example, a pH error of 0.01 pH units combined with a pCO_2 error of 9 μatm, or a pH error of 0.0018 pH units combined with a pCO_2 error of 16 μatm would both produce a DIC error of 150 $\mu mol\ kg^{-1}$.

We can further examine the quality of the pH and pCO_2 data sets by comparing the different DIC estimates. If the pH and pCO_2 data are accurate, the pH and pCO_2 data will produce identical DIC values when paired with the same A_T, because of the relationship between the four inorganic carbon parameters. Our pH-A_{Tsalin} and pCO_2-A_{Tsalin} derived DIC remained close for most of the deployment (Fig. 3.4.4B, 3.4.4C), with a difference near zero initially and $\leq 5\ \mu mol\ kg^{-1}$ after 1 month. This difference increased to 10 $\mu mol\ kg^{-1}$ by the end of the second month and then rose rapidly during the last 12 days of the deployment to a maximum of 16 $\mu mol\ kg^{-1}$ (Fig. 3.4.4C). The modeled DIC therefore supports the quality of the pH and pCO_2 data despite the large drift produced by the pH-pCO_2 combination. The accuracy of the A_T data, and by extension the DIC data, is discussed in detail below.

We examined short-term DIC changes using unfiltered pH-A_{Tsalin} and pCO_2-A_{Tsalin} derived DIC (Fig. 3.4.5A). Similar to the long-term trends, the two DIC estimates

show nearly the same short-term variability throughout the deployment, even as they start

to drift away from each other slightly over time, as in Fig. 3.4.4B (mean DIC

difference=10 µmol kg^{-1} ±13 µmol kg^{-1}). The pH-A_{Tsalin} and pCO_2-A_{Tsalin} data put

bounds on the uncertainty of the pH and pCO_2 and provide a means for quality control. It

is not possible, however, to determine which sensor or sensors are inaccurate. In order to

determine the accuracy of the A_{Tsalin} data, we used the pH-A_{Tsalin} combination to model

pCO_2. The mean difference between the measured and modeled pCO_2 was -15 µatm ±15

µatm, indicating that our A_{Tsalin} is an accurate representation of A_T, even in this

complicated upwelling system. If the A_{Tsalin} data were incorrect, the pCO_2-A_{Tsalin}

combination would not model a pCO_2 that matched the measured pCO_2, which was

determined to be accurate through the DIC modeling. When a constant A_T of 2254 µmol

kg^{-1} was combined with the pH data to model pCO_2, the mean pCO_2 difference

(measured-modeled) was -20 µatm ±15 µatm, indicating that in addition to an accurate

mean, the salinity-derived A_T is accounting for some of the variability in A_T. To further

verify the accuracy of our A_{Tsalin} relationship we also modeled A_T with the temperature-

salinity-A_T relationship of Lee et al. (2006) (not shown). The Lee et al. relationship for

this region predicts an A_T that is ~21 µmol kg^{-1} higher than our A_{Tsalin} value from G.

Freiderich. When the Lee A_{Tsalin} is combined with pH to model pCO_2, the difference

between the measured and modeled pCO_2 increases to -19 µatm ±15 µatm. The Lee

A_{Tsalin} is also 5 µatm below the measured pCO_2 at the start of the deployment, while the

Freiderich A_{Tsalin} is only 1.5 µatm below the measured pCO_2 initially. Subtracting 10

µmol kg^{-1} from the Freiderich A_{Tsalin} would produce a modeled pCO_2 that matches the

measured pCO_2 initially, suggesting that the Freiderich A_{Tsalin} is likely within 10 µmol

kg^{-1} of the actual value. The accuracy of the pCO_2 data modeled from pH and the Gernot A_{Tsalin} also indicates that the DIC modeled from these parameters is correct. The relationship between the four measurable inorganic carbon parameters dictates that if the pH and A_{Tsalin} correctly predict pCO_2, the modeled DIC must also be accurate. To further examine the sensor behavior we compared the modeled DIC with measured nitrate (below).
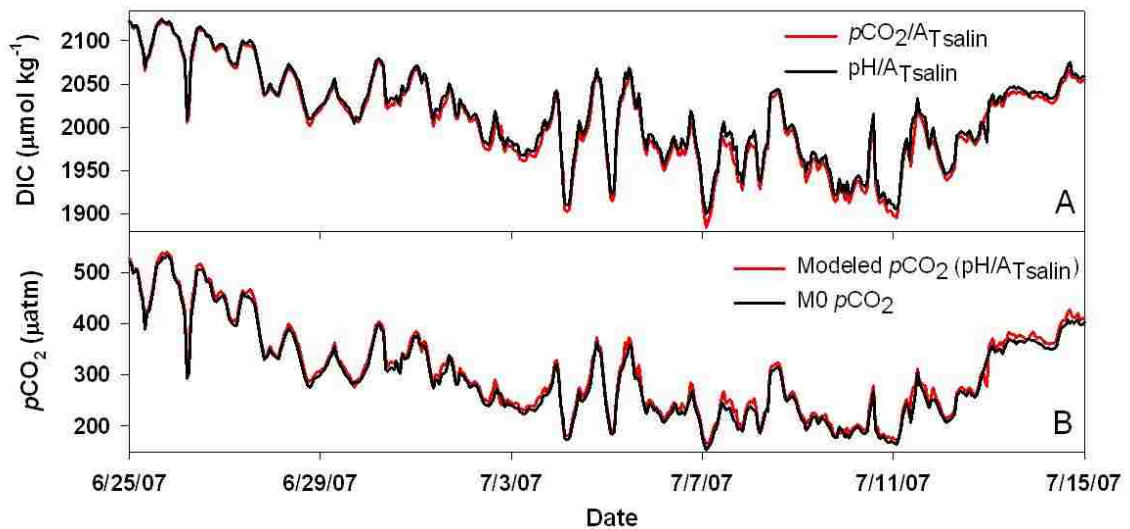
Fig. 3.4.5. (A) Blowup of modeled DIC derived from unfiltered pH-A_{Tsalin} (black) and unfiltered pCO_2-A_{Tsalin} (red). (B) Blowup of unfiltered measured pCO_2 from the M0 non-dispersive infrared analyzer (black) and modeled pCO_2 derived from unfiltered pH-A_{Tsalin} (red).

3.4.3 Nitrate

The raw and 30-hour low-pass filtered nitrate data from the M0 buoy are shown in Fig. 3.4.6A. The nitrate varied between 0.3 and 15.2 μM, with higher nitrate values following the stronger upwelling periods. Through Redfield ratio calculations the nitrate data were compared to the pH-pCO_2 derived DIC. $\Delta DIC_{nitrate}$ was calculated from the

change in the 30-hour low-pass filtered nitrate (ΔNO_3^-) each hour, referenced to the initial value, and the Redfield ratio (Eqn. (3.7)).

$$\Delta DIC_{nitrate} \quad = \quad \Delta NO_3^- \quad * \quad \frac{106 \, CO_2}{16 \, NO_3^-} \qquad\qquad (3.7)$$

The ΔDIC, referenced to the initial value, was also calculated using the DIC modeled from 30-hour low-pass filtered pH-A_{Tsalin} and pCO_2-A_{Tsalin} (Fig. 3.4.6B). When nitrate was less than 4 μM, the $\Delta DIC_{nitrate}$ did not follow the other ΔDIC estimates. Johnson (2010) showed similar trends further offshore in Monterey Bay. During low nitrate periods, fixed nitrogen is thought to be supplied from other sources such as ammonium or vertically migrating phytoplankton from deeper high nitrate waters (Johnson, 2010). Table 3.4.1 shows the differences between the various ΔDIC values for the periods when nitrate is > 4 μM. During the first time period both the $\Delta DIC_{pH/ATsalin}$ and the $\Delta DIC_{pCO2/ATsalin}$ match the $\Delta DIC_{nitrate}$ to within 2 ± 5 μmol kg^{-1}. By the end of the deployment the $\Delta DIC_{pH/ATsalin}$ was within -1.4 ± 6.9 μmol kg^{-1} of the $\Delta DIC_{nitrate}$ while the difference between the $\Delta DIC_{pCO2/ATsalin}$ and the $\Delta DIC_{nitrate}$ was 9.8 ± 6.0 μmol kg^{-1}. The direction of the ΔDIC errors relative to the nitrate data are consistent with the DIC drift from the pH-pCO_2 combination, with high pH data and low pCO_2 data (Table 3.4.1). The $\Delta DIC_{nitrate}$ further reinforces that the pH and pCO_2 instruments are providing accurate DIC data over the deployment length and supports the accuracy of the nitrate data.
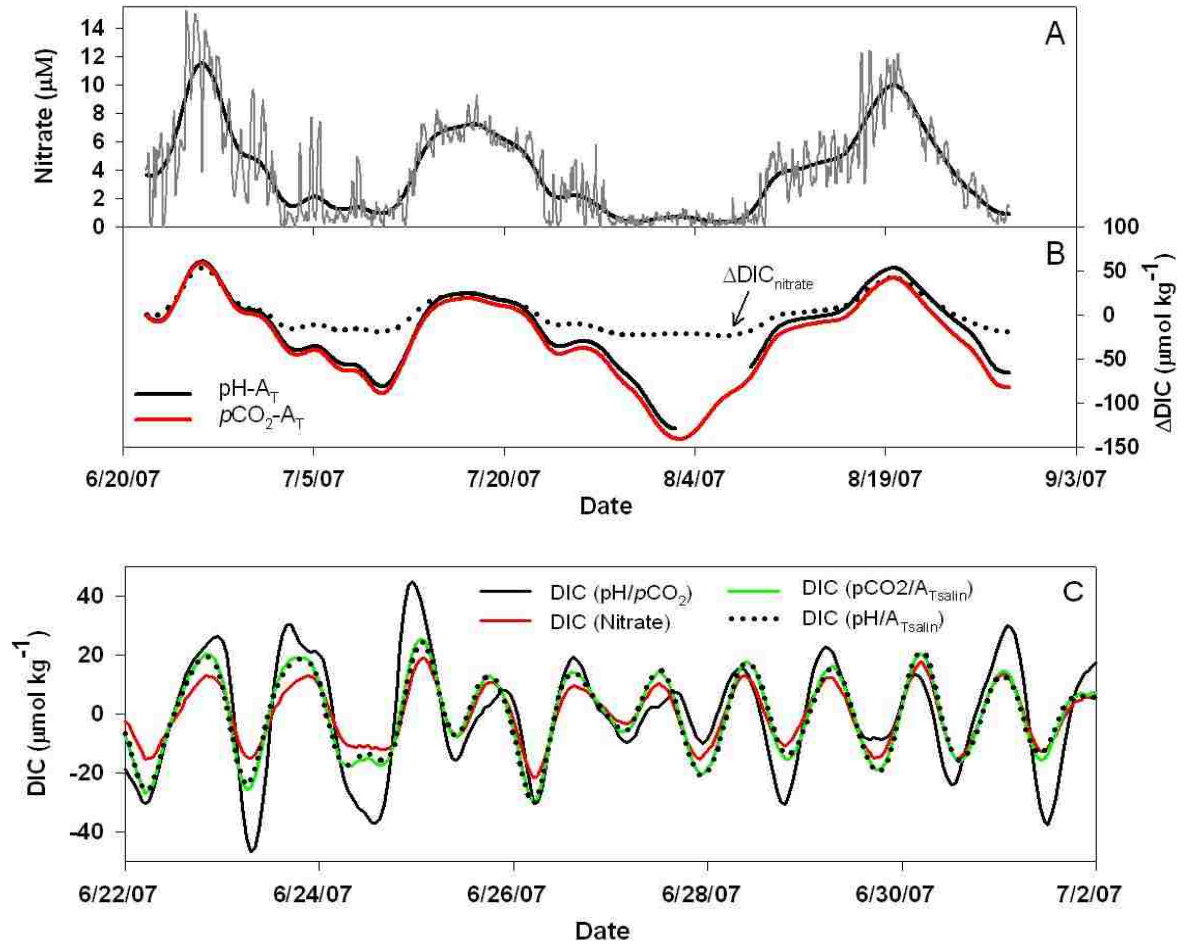
Fig. 3.4.6. (A) Unfiltered nitrate (gray) and 30-hour low-pass filtered nitrate (black) from the ISUS nitrate sensor on the M0 buoy. (B) Modeled $\Delta DIC_{nitrate}$ (dotted black), ΔDIC from pH-A_{Tsalin} (solid black), and ΔDIC from pCO_2-A_{Tsalin} (solid red). $\Delta DIC_{nitrate}$ is calculated using the ΔNO_3 data and the Redfield ratio. The ΔDIC values are all calculated from 30-hour low-pass filtered data and referenced to the initial value. The gap in the data corresponds to clogging of the SAMI-pH inlet tubing. (C) Blowup of 33 hour high-pass filtered DIC modeled from pH-pCO_2 (black), pCO_2-A_T (green), pH-A_{Tsalin} (dotted black) and nitrate (red). The DIC values are all calculated from 4-hour filtered data. DIC from nitrate was calculated using the Redfield ratio (106:16) and adjusted to an initial DIC of 2035 $\mu mol\ kg^{-1}$. Note the change in the timescale for C.

Table 3.4.1

Mean difference between $\Delta DIC_{nitrate}$ and $\Delta DIC_{pH/ATsalin}$ or $\Delta DIC_{pCO2/ATsalin}$ for Monterey Bay.

Time Period	$\Delta DIC_{nitrate}-$ $\Delta DIC_{pH/ATsalin}$	$\Delta DIC_{nitrate}-$ $\Delta DIC_{pCO2/ATsalin}$
6/23/07 00:00 - 7/1/07 06:00	-0.4 ± 4.8	1.8 ± 5.4
7/13/07 00:00 - 7/22/07 12:00	2.6 ± 5.0	8.4 ± 4.2
8/11/07 20:00 - 8/24/07 07:00	-1.4 ± 6.9	9.8 ± 6.0

ΔDIC differences are given in $\mu mol\ kg^{-1}$. The time periods represent nitrate values >4 $\mu mol\ L^{-1}$. All ΔDIC values are referenced to the initial DIC value.

In addition to providing a long-term accuracy check, the nitrate data were used to verify the short-term changes in modeled DIC seen in Fig. 3.4.4B. Figure 3.4.6C shows the 33-hour high-pass filtered DIC modeled from 4-hour low-pass filtered pH-pCO_2, pCO_2-A_T and pH-A_T, as well as the DIC derived from nitrate using Eqn. (3.7). The $\Delta DIC_{nitrate}$ was scaled to an absolute $DIC_{nitrate}$, using the initial $DIC_{pH/pCO2}$ value of 2035 $\mu mol\ kg^{-1}$. The 33-hour high-pass filter was applied to the data after modeling to eliminate the long-term variability in the data. The pH-A_T and pCO_2-A_T DIC followed each other closely, with a mean difference of 0.0 ± 1.4 $\mu mol\ kg^{-1}$ between the two series. The $DIC_{nitrate}$ showed short-term changes of up to 40 $\mu mol\ kg^{-1}$, reinforcing the validity of the 4-hour filtered DIC from these two inorganic carbon pairings (Fig. 3.4.6C). In contrast, the pH-pCO_2 DIC diel range was often much larger than the $DIC_{nitrate}$ range, sometimes larger than 80 $\mu mol\ kg^{-1}$. The small difference between the pH-A_T and the pCO_2-A_T curves lead to much of the larger variability seen in the pH-pCO_2 plot, as predicted from the discussions of the pH-pCO_2 combination, above. Differences between the $DIC_{nitrate}$ and the pH-A_T and pCO_2-A_T curves could also be due to a breakdown in the

A_T-salinity relationship during high nitrate upwelling periods. Future research is needed to definitively determine what is causing these differences.

3.4.4 Saturation State

While the pH-pCO$_2$ combination can produce long-term drifts in A_T and DIC estimates, pH-pCO$_2$ may be useful for modeling long-term changes in aragonite and calcite saturation states (Ω_{arg}, Ω_{cal}). Saturation state is defined in Eqn. (1.10). Since saturation states are dependent on the CO_3^{2-} concentration, which is much smaller than the A_T or DIC concentrations, they are potentially less sensitive to pH-pCO$_2$ errors. Aragonite and calcite were modeled in CO2SYS (Pierrot et al., 2006) using pH-pCO$_2$, pH-A_{Tsalin} and pCO$_2$-A_{Tsalin} (Fig. 3.4.1D, Table 3.4.2). For the first seven days of the deployment the pH-pCO$_2$ modeled saturation states match the other model pairings to within 0.003±0.017. Over time, the pH-pCO$_2$ modeled Ω_{arg} and Ω_{cal} slowly drift below the curves produced by the additional carbonate parameter pairings (Fig. 3.4.1D, Table 3.4.2). The pH-pCO$_2$ data modeled the CaCO$_3$ saturation states to within 0.15 ± 0.095 for aragonite and 0.24 ± 0.15 for calcite over the 69 day deployment (Fig. 3.4.1D, Table 3.4.2) compared to the A_{Tsalin} derived values.

Table 3.4.2
Final and mean difference between modeled saturation state values for Monterey Bay.

$CaCO_3$ Mineral	Saturation State Model Parameters	Saturation State Difference (after 69 days)	Mean Difference ± Std Deviation
Calcite	(pH-A_{Tsalin})-(pH-pCO_2)	0.35	0.14 ± 0.087
Calcite	(pCO_2-A_{Tsalin})-(pH/pCO_2)	0.58	0.24 ± 0.15
Aragonite	(pH-A_{Tsalin})-(pH-pCO_2)	0.22	0.09 ± 0.056
Aragonite	(pCO_2-A_{Tsalin})-(pH/pCO_2)	0.37	0.15 ± 0.095

Saturation ranged from 1.8-3.7 and 2.9-5.8 for aragonite and calcite, respectively (Fig. 3.4.1D). The changes in saturation state are inversely related (R^2=0.0885, p<0.0005, n=291, for aragonite) to the upwelling index. Upwelled waters are more acidic and have lower carbonate concentrations than surface waters. When the saturation state drops below 1, $CaCO_3$ becomes under-saturated and dissolution is expected. However, numerous studies have shown that decreases in the saturation states can have detrimental effects on $CaCO_3$ forming organisms, even when the saturation state is still above 1 (Langdon and Atkinson, 2005; Langdon et al., 2000; Leclercq et al., 2002). Our data agree with that of Feely et al. (1984) who found aragonite saturation values between 2 and 3 for Eastern North Pacific waters. Feely et al. (2008) also showed that surface waters near Monterey Bay were oversaturated with respect to aragonite down to approximately 50 meters during the 2007 upwelling season. However, the $CaCO_3$ saturation states are expected to continue to decline as atmospheric CO_2 levels increase

(Feely et al., 2004; Kleypas et al., 1999b) and coastal sites north of Monterey Bay have already shown aragonite undersaturation in surface waters (Feely et al., 2008). As anthropogenic CO_2 uptake combines with upwelling events, this site could be at risk for surface aragonite undersaturation in the near future.

3.5 Southern Ocean Deployment

To further confirm the consistency of using pH data for inorganic carbon modeling, data from the Southern Ocean Gas Exchange cruise (2008) were examined. During this cruise a SAMI-pH and a SAMI-CO_2 were deployed in tandem. The data are shown in Fig. 3.4.7A, along with temperature and salinity (Fig. 3.4.7B). The pH and $p$$CO_2$ ranged from 8.11-8.16 pH units and 305-331 μatm, respectively, with temperature and salinity ranges of 4.3-6.3 ^{o}C and 33.6-33.8, respectively. The differences in variability between the pH and the $p$$CO_2$ data are possibly due to differences in instrument placement on the MAPCO2 buoy. The SAMI-pH was attached directly to the buoy at the surface, where water may not have exchanged as well as with the SAMI-CO_2, located on the mooring chain at 5 meters. Discrete DIC and A_T samples collected during the cruise were used for comparison with the SAMI-pH and SAMI-CO_2 data. The salinity-derived A_T was calculated using the Lee et al. (2006) relationship for the Southern Ocean, but was not used for modeling as it did not match the discrete A_T points (measured-modeled $A_T = 16 \pm 3$ μmol kg^{-1}). This difference is not unexpected since there is not a well-defined A_{Tsalin} relationship for this region of the Southern Ocean because of a lack of data (Lee et al., 2006), unlike the relationship used for Monterey Bay.
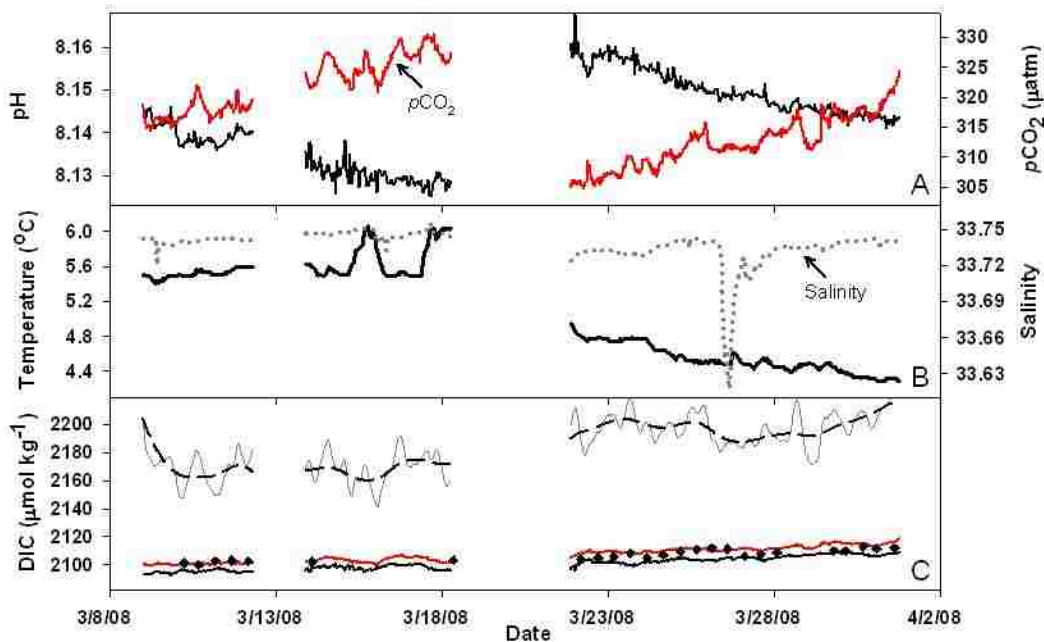
Fig. 3.4.7. Data from the Southern Ocean Cruise. (A) In situ pH (solid black) and pCO_2 (red). (B) Salinity (dotted gray) and temperature (solid black). (C) Discrete DIC (black diamonds), DIC modeled from 4-hour low-pass filtered pH-pCO_2 (gray) and DIC modeled from 30-hour low-pass filtered pH-pCO_2 (dashed black), pH-$A_{Tdiscrete}$ (solid black) and pCO_2-$A_{Tdiscrete}$ (solid red). The first gap in the data corresponds to when the instruments were removed from the water for instrument reconfiguration. The second gap in the data corresponds to when the instruments were removed from the water due to rough weather.

Similar to the Monterey Bay data, when DIC is modeled from the unfiltered in situ pH and pCO_2 data, the resulting unfiltered DIC data show large short-term variability (32-103 μmol kg^{-1}, not shown) compared to the discrete DIC data. Figure 3.4.7C shows the 4-hour and 30-hour low-pass filtered pH-pCO_2 derived DIC. While the filters reduced the short-term variability in the DIC data, similar to the Monterey Bay data, the modeled DIC does not match the discrete DIC even at the start of the deployment. The mean DIC offset (discrete-modeled$_{pH-pCO2}$) was -82 μmol kg^{-1} ± 18 μmol kg^{-1} (n=25). The offsets between the modeled and discrete DIC values are fairly consistent throughout

the deployment, rather than the slowly increasing offset seen in the Monterey Bay data. There was an increase in the constant offset after the instruments were removed from the water on March 18th for rough weather. This supports the observation that there was no fouling of the instruments during this deployment, suggesting that the observed DIC offsets are caused by inaccuracy from the pH-pCO_2 combination. As mentioned above, a pH error of ± 0.0016 and a pCO_2 error of ± 5 µatm will generate a DIC error of 60 µmol kg^{-1} and these errors are within the normal accuracy range of both SAMIs. This DIC offset may also be caused by errors in the pKa' of the mCP indicator at the low (4-6 ^{o}C) measurement temperatures. Current work by T. Moore and R. Spaulding have shown an offset in the pKa' at low temperatures but the magnitude and direction of this error are still uncertain.

Discrete A_T samples were collected, making it possible to model DIC from pH/$A_{Tdiscrete}$ and pCO_2-$A_{Tdiscrete}$. The mean DIC difference between the discrete DIC and the pH-$A_{T\ discrete}$ derived DIC was 5 ± 2 µmol kg^{-1} (n=25) while the DIC difference between the discrete DIC and the pCO_2-$A_{T\ discrete}$ derived DIC was -1 ± 3 µmol kg^{-1} (n=25) over the entire deployment. The mean drift between the DIC modeled from pH-$A_{T\ discrete}$ and the DIC modeled from pCO_2-$A_{T\ discrete}$ was 7 ± 1 µmol kg^{-1} over 21 days, similar to the drift in the Monterey Bay data, 3 ± 2 µmol kg^{-1} over 21 days. The mean offsets for each of the three sub-deployments are shown in Table 3.4.3.

Table 3.4.3
Mean difference between discrete DIC and modeled DIC (unfiltered data) for the
Southern Ocean cruise. Values shown represent the mean value ± standard deviation.

Time Period	Discrete-(pH-pCO$_2$)	Discrete-(pH-A$_{Tdiscrete}$)	Discrete-(pCO$_2$-A$_{Tdiscrete}$)
3/08/08 - 3/12/08 (n=5)	-61 ± 13	8 ± 3	2.5 ± 2
3/13/08 - 3/18/08 (n=2)	-50 ± 6	5 ± 2	1 ± 1
3/21/08 - 3/31/08 (n=18)	-91 ± 10	5 ± 2	-2 ± 2

DIC difference values are given in µmol kg^{-1}.

These data reinforce our observations that while the pH and pCO$_2$ combination can have difficulties accurately modeling long-term DIC and A$_T$ changes, the pH and pCO$_2$ can be combined with discrete or salinity-derived A$_T$ to model DIC and to check for internal consistency between the pH and pCO$_2$ data. The pH data were combined with the discrete A$_T$ data to model pCO$_2$ with an accuracy of 12 ± 3 µatm compared to the measured pCO$_2$ (not shown). A pH accuracy error of ~0.007 combined with an A$_T$ accuracy error of 2 µatm would lead to the average observed DIC difference (~7 µmol kg^{-1}, Table 3.4.3) and pCO$_2$ errors. The next generation SAMI-pH design will include a Tris buffer standard (DelValls and Dickson, 1998) that will be used to check, and correct, the accuracy of the pH measurement throughout the deployment.

3.6 Conclusions

The Monterey Bay data showed large changes in pH and pCO$_2$ due to seasonal upwelling, while the Southern Ocean values were fairly constant. Despite these differences, both datasets illustrated that the pH or pCO$_2$ data can be combined with discrete or salinity-derived A$_T$ to produce accurately modeled long-term DIC changes.

These inter-comparisons can also help verify pH and pCO$_2$ instrument performance. The Monterey Bay data suggested that heavily filtered pH and pCO$_2$ might be useful for DIC modeling under conditions where fouling does not occur, but the Southern Ocean data did not support this, as the modeled DIC showed large offsets from discrete values even with no instrument fouling. Additional pH-pCO$_2$ deployments on a coral reef off of the coast of Puerto Rico have shown pH-pCO$_2$ drifts over time similar to the Monterey Bay data, while deployments in an upwelling area off the coast of Oregon have produced pH-pCO$_2$ DIC data that matches pH-A$_T$ and pCO$_2$-A$_T$ DIC records throughout a two month period. These conflicting results indicate that further research is needed to determine the quality of long-term pH-pCO$_2$ DIC modeling on moorings. The Monterey Bay data did show that pH variability at this coastal site is large compared with open ocean values (Emerson et al., in preparation). Organisms that have evolved in these upwelling environments are presumably accustomed to a broad range of pH and CaCO$_3$ saturation. However, this pH range has already dropped by 0.1 pH units due to anthropogenic CO$_2$ accumulation (Caldeira and Wickett, 2003) and will continue to drop with increasing CO$_2$ penetration. The pH-pCO$_2$ combination proved useful for estimating accurate saturation state changes at this site.

When unfiltered pH or pCO$_2$ data from Monterey Bay were combined with A$_{Tsalin}$, the two modeled DIC series showed nearly identical short-term variability, reinforcing the accuracy of the pH and pCO$_2$ data. In situ pH data is also valuable for modeling pCO$_2$, if direct pCO$_2$ measurements are not available and an accurate A$_{Tsalin}$ relationship is known. The Monterey Bay data showed that even with a 4-hour low-pass filter, the pH-pCO$_2$ combination does not always accurately model short-term changes in A$_T$ and

DIC. The large short-term spikes in modeled DIC are due to precision errors in the pH

and pCO$_2$ that are amplified in the modeling process, due to the inverse relationship

between pH and pCO$_2$. After applying a 4-hour low-pass filter to the pH and pCO$_2$ data,

the resulting short-term DIC changes are closer to DIC estimates from nitrate

measurements in Monterey Bay, but still show inconsistent large errors. Future research

is needed to fully understand what is driving the smaller differences in variability

between the nitrate and pH-pCO$_2$ data. These data highlight the usefulness of in situ pH

data for estimating DIC, pCO$_2$ and saturation states, but also illustrate the need for long-

term, in situ A$_T$ and DIC sensors which would allow us to over-characterize, and better

understand, changes in the marine inorganic carbon cycle.

CHAPTER 4

Short-Term to Seasonal pH Variability in a Coral Reef

4.1 Abstract

In order to characterize the short-term and seasonal pH variability in a coral reef, autonomous sensors for pH and the partial pressure of carbon dioxide (pCO_2) were deployed on Media Luna reef, Puerto Rico for two month periods over three seasons. pH was at a minimum of 7.89 pH units during the fall and at a maximum of 8.17 pH units during the winter. Average monthly pH varied between 7.99 and 8.10 pH units. The average diel pH range was 0.08 ± 0.03 pH units, with a seasonal diel minimum and maximum of 0.012 and 0.176 pH units, respectively. In order to determine what was driving pH changes at the site, sensors for temperature, salinity, depth, wind speed, current speed and direction, and oxygen were simultaneously deployed with the pH and pCO_2 sensors. Half of the seasonal pH variation was driven by temperature, with the remaining changes due to organic carbon and $CaCO_3$ production. CO_2 gas fluxes showed that the reef was a source of CO_2 to the atmosphere during the summer and fall seasons, and a sink during the winter. Annually, the reef was a source of CO_2, with a flux of 1.19 mol m^{-2} year^{-1}. Calcium carbonate saturation states modeled with pH and pCO_2 showed seasonal values between 2.7-4.7 for aragonite and 4.1-7.0 for calcite. Model predictions indicate that aragonite saturation will be at a mean saturation of 3.0 year-round if atmospheric CO_2 values increase to 500 µatm. Calcification rates determined from pH, pCO_2 and O_2 data showed very small fluxes of -0.012-0.010 mol m^{-2} hr^{-1} during the winter, which are within the margin of error of the instruments. During the fall, daily

fluxes were larger at -0.023 to 0.029 mol m^{-2} hr^{-1}. The net seasonal change for the fall

was -1.0919 mol m^{-2}, indicating $CaCO_3$ dissolution on the reef.

4.2 Introduction

Atmospheric carbon dioxide (CO_2) levels have increased dramatically over the

last century due to anthropogenic emissions, with the oceans absorbing approximately

one third of this carbon (Sabine et al., 2004). While this absorption has helped reduce

greenhouse gas levels, it can also lead to significant changes in the chemistry of the

oceans (Feely et al., 2004). Absorbed CO_2 reacts with seawater to form carbonic acid,

lowering the seawater pH, the concentration of carbonate ions (CO_3^-) and the $CaCO_3$

saturation states (e.g.Cao et al., 2007; Fabry et al., 2008; Orr et al., 2005). These

combined effects have been termed ocean acidification. The ocean pH has already

decreased more than 0.1 pH units since the start of the industrial revolution (Caldeira and

Wickett, 2003). Once CO_2 is absorbed in the oceans there is no practical way to remove

it, and the oceans will require thousands of years to naturally return to a higher pH state

(Raven et al., 2005; Solomon et al., 2009).

These pH changes will likely have a large negative impact on marine organisms

and ecosystems (Fabry et al., 2008; Raven et al., 2005). Corals and other calcifying

organisms are particularly at risk due to their dependence on $CaCO_3$ saturation states

(Gledhill et al., 2008). Laboratory tests have shown that as the pCO_2 of seawater is

increased, coral $CaCO_3$ production begins to decline (Jokiel et al., 2008; Langdon and

Atkinson, 2005; Langdon et al., 2003; Leclercq et al., 2000). These experiments provide

insights into how corals may react to changing CO_2 levels, but it can be difficult to

extrapolate the data to natural systems, in part because the natural range of pH variability is unknown. Measurement temporal coverage is also typically a limiting factor. While some studies have used in situ pCO_2 or pH sensors to obtain more continuous data, high temporal resolution of important parameters such as $CaCO_3$ saturation states has not been possible.

The current field studies of pH in reefs have predominantly used pH electrodes to examine shallow reefs (0.5-4 m water depth), often at low temporal resolution. Ohde (1995) measured the pH of discrete samples on a platform reef off of Okinawa over a two day period. Twelve hour surface pH variations were ~0.15 pH units in the reef lagoon (4 m depth) and ~0.64 pH units in the back reef (1.5 m depth), which experienced slack water periods during low tides. Discrete pH samples collected over a three day period in a reef lagoon (1.5-3 m depth) off Miyako Island showed 12 hour pH variations of ~0.14 pH units (Kraines et al., 1997). Samples were collected during three different seasons but pH values were only reported for the fall. Kayanne et al. (2005) measured pH over an entire year with a pH sonde on a fringing reef (1.5-2.5 m depth) off of Ishigaki Island and reported an average yearly diel change ~0.5 pH units and a seasonal pH change of ~0.1-0.2 pH units. On the Molokai reef flat, Yates and Halley (2006) pumped water from an in situ isolation chamber on the reef (1-2 m water depth) to a flow through pH electrode system for 1 day periods in the winter and summer seasons. Twelve hour pH variability ranged from 0.05 pH units on a coral rubble surface in the winter to 0.26 pH units on a patch reef in the summer, with a seasonal pH change of ~ 0.19 pH units on the patch reef. pH was measured over 24-48 hour periods approximately monthly from 2000-2002 by Silverman et al. (2007). Over the two year period, the monthly pH average in the reef

lagoon (1.5-1.8 m water depth) varied by 0.08 pH units, from 8.18-8.26 pH units. Boron

isotopic proxy records have also been used to estimate natural reef pH. Data from the

Great Barrier Reef have shown pH variations of 0.3 pH units over the last 300 years at

Flinders Reef (Pelejero et al., 2005) and a pH decrease of ~0.2-0.4 pH units from the

1940's to the present at Arlington Reef (Wei et al., 2009).

Ocean pH variability has also been studied outside of coral reefs. Data from the

European Time Series in the Canary Islands (ESTOC) showed seasonal pH variability of

0.03-0.04 pH units (Santana-Casiano et al., 2007), while data from the coastal eastern

Atlantic ocean showed diel pH variations of 0.24 pH units and seasonal variations of up

to 1 pH unit (Wootton et al., 2008). All of these data were measured with pH electrodes,

with the exception of the ESTOC site, which used pH electrodes until 1997 and the

discrete spectrophotometric pH technique (Byrne and Breland, 1989) after 1997.

Monthly records from the Bermuda Atlantic Time Series (BATS) show seasonal modeled

pH variations of 0.07-0.1 pH units, while data from the Hawaii Ocean Time Series show

modeled seasonal pH variations of 0.03-0.04 pH units. pH data at the time series stations

were modeled using A_T and DIC discrete samples. Models for the Southern Ocean have

estimated annual pH variability at 0.06 pH units (McNeil and Matear, 2008).

The above studies all relied on discrete and continuous potentiometric pH

measurements, discrete spectrophotometric pH measurements or modeling from discrete

A_T and DIC samples. While pH electrodes can provide continuous pH measurements,

they are subject to large systematic errors (Dickson, 1993) and have not been frequently

used for long-term in situ pH measurements. With the development of

spectrophotometric pH methods (Byrne and Breland, 1989), precise and accurate pH

measurements became possible, but until recently also required the collection of discrete samples. Discrete field sampling programs can be costly and time consuming to maintain and may still miss the dynamic short-term and seasonal inorganic carbon changes on coral reefs. This lack of high temporal resolution, long term, quality pH data has made it difficult to determine the natural range of pH on coral reefs and to predict how reef ecosystems will respond to ocean acidification. In an effort to overcome these problems, several sensors for spectrophotometric pH measurements have been developed in the past (Liu et al., 2006; Nakano et al., 2006; Seidel et al., 2008). An indicator-based pH sensor , the submersible autonomous moored instrument for pH (SAMI-pH), is now available and is capable of long-term, in situ pH measurements (Cullison et al., in preparation; Martz et al., 2003; Seidel et al., 2008). In addition to determining pH variability, the SAMI-pH data can be used to further characterize the inorganic carbon cycle. In particular, the pH can be combined with in situ pCO_2 data to determine continuous calcium carbonate ($CaCO_3$) saturation state records (Cullison et al., in preparation). While $CaCO_3$ saturation states can be calculated from any two of the four inorganic carbon parameters, pH and pCO_2 are currently the only inorganic parameters for which long-term in situ sensors are available.

In this work we used the SAMI-pH (Martz et al., 2003; Seidel et al., 2008), in conjunction with the SAMI-CO_2 (DeGrandpre et al., 1995), to study inorganic carbon changes on a coral reef in Puerto Rico, USA. The main objectives of this study were to characterize the full range of seasonal and short-term pH variability on the reef and to determine what processes control pH variability and saturation states at this site. These data represent the first time the SAMI-pH was deployed in a coral reef system.

4.3 Methods

4.3.1 Site Description

The La Parguera shelf reef system is located on the southern coast of Puerto Rico. The reefs are surrounded by coarse-grained carbonate sediments, with the community consisting of three main coral zones across the shelf (Acevedo et al., 1989). The first zone, the Mixed Coral Zone, occupies the flat section of the reef front at a depth of 4-10 meters. Montastrea annularis and Acropora cervicornis are the dominant species, with low coral cover (Acevedo et al., 1989). The second coral zone is the Massive Coral Zone, where corals grow on a steep slope at a depth of 9-24 meters. Montastrea, Porites and Agaricia species dominate, with moderate coral cover. At a depth of 22-24 meters the reef system shifts to the Agaricia-Montastrea zone, which continues down the shelf slope to 40 meters. Agaricia species and Montastrea annularis are dominant, with moderate to low coral cover (Acevedo et al., 1989). Coral bleaching has been frequent at La Parguera since the mid-1980's, with an increase of 0.7 $^{\circ}$C in the maximum summer temperature from 1966-1995 (Winter et al., 1998). The area consists of a nearshore mangrove system (Acevedo et al., 1989) and water on the shelf reef system has an oceanic source, with a general east to west current flow (discussed below).

The study location was selected to take advantage of measurements being made at the NOAA Coral Reef Early Warning System (CREWS) buoy on Media Luna Reef (Fig. 4.3.1). Media Luna Reef is approximately 1.5 km long, located roughly 3.3 km south of La Parguera, Puerto Rico, and is within the mixed coral zone of the La Parguera reef system. Sample sites were located at the head (17°56'17"N, 67°02'25"W) and tail (17°56'19"N, 67°03'7"W and 17°56'7"N, 67°02'54"W) of Media Luna reef, with waters

approximately 4 m deep at head site A, and 5 and 4 m deep at tail sites B and C,

respectively (Fig. 4.3.1).
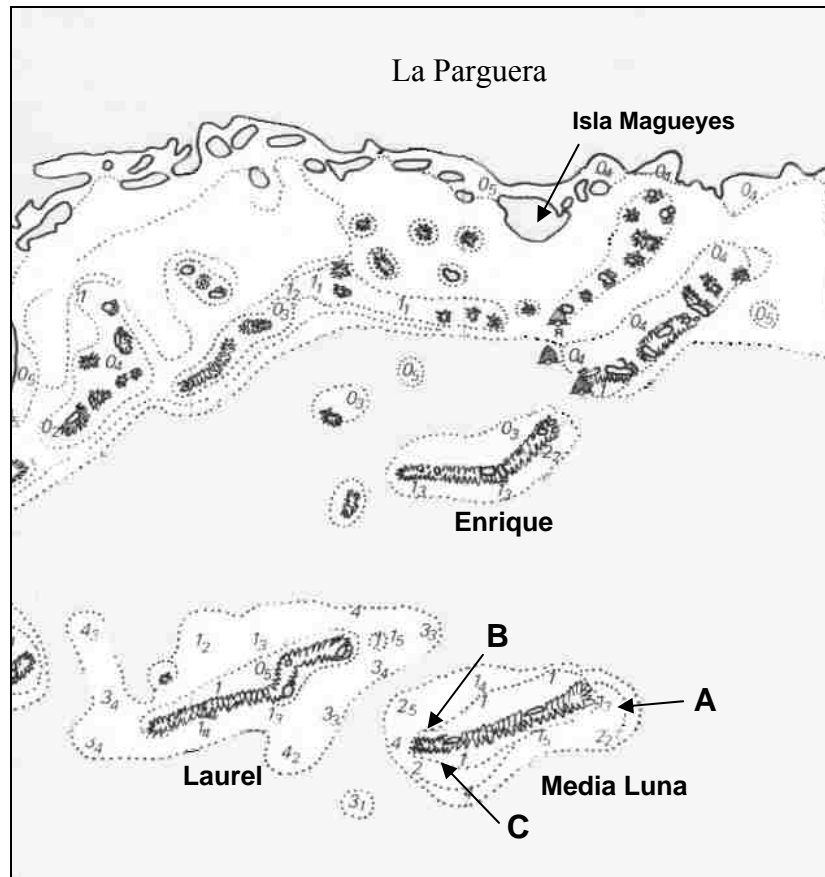
Fig. 4.3.1 Location of Media Luna reef off the southwest coast of Puerto Rico at La Parguera. Point A shows the location of the SAMIs at the Media Luna reef head for all three deployments, point B shows the location of the CREWS mooring and the SAMIs at the Media Luna reef tail for deployments #1 and #2 and point C shows the SAMIs location at the reef tail for deployment #3.

The NOAA CREWS buoy is located at the reef tail site B. The CREWS buoy

was installed at Media Luna because the reef met NOAA's numerous site considerations

which included the site: be within a US territory, have a bottom surface hard enough to

drill into, be accessible for cleaning every ten days to two weeks and be located on the lee

side from prevailing winds (J. Hendee, pers. comm., 2009). The University of Puerto

Rico, Mayagüez satellite campus on Magueyes Island in La Parguera, Puerto Rico

provides cleaning and research support for the buoy. For this study, two sites were

selected at the head and tail of the reef in order to measure differences in the water

coming onto and leaving the reef. Site A is located on the leading edge of the reef in

terms of the prevailing currents, while site B is located at the CREWS buoy on the reef

tail. Three separate deployments were carried out on Media Luna reef from June 19-

August 21 2007, January 7-March 14 2008 and September 16-November 21 2008. After

examining current and salinity data from the second deployment, we determined that

water masses from site A were not traveling directly to site B. For the third deployment,

a new reef tail site was chosen (site C) so that the reef tail site would be directly in the

flow path of water coming from site A.

4.3.2 In situ Measurements

Air and water temperature, salinity, photosynthetically active radiation (PAR) and

wind velocity were measured hourly on the NOAA CREWS mooring. Water

temperature, salinity and PAR sensors were located near the reef bottom (~5 m depth).

In situ pH and pCO$_2$ data were measured every half hour using SAMI-pHs and SAMI-

CO$_2$s, respectively, which were deployed on the bottom at sites A and C and

approximately 1 m from the bottom at the CREWS site B (Fig 4.3.1). The SAMI-pH and

the SAMI-CO$_2$ are both indicator-based sensors. The SAMI-pH mixes a meta cresol

purple (mCP) indicator with a seawater samples and measures the change in absorbance

to determine pH. The SAMI-CO$_2$ consists of a silicone rubber membrane filled with

bromothymol blue (BTB) indicator. The CO_2 in seawater diffuses across the membrane and reacts with the indicator. The change in the absorbance of the indicator is then measured to determine pCO_2. Before deployment, the SAMI-pH accuracy was checked by comparison with UV/VIS measurements of seawater samples or with Tris buffer in synthetic seawater (DelValls and Dickson, 1998). These measurements gave an accuracy of 0.001-0.005 ± 0.0006 pH units. The SAMI-CO_2s were calibrated using CO_2 gas mixtures verified with an infrared CO_2 analyzer (LI-COR) then checked for accuracy in a laboratory water tank with a CO_2 membrane equilibrator leading into a LI-COR. Accuracy of the SAMI-CO_2 is 5 µatm with a precision of $\pm$ 1 µatm. Dissolved oxygen (Aanderaa Optodes 4175) was measured every half hour during the last two deployments. Oxygen sensors were calibrated in saturated and zero oxygen solutions before deployment. The saturated solution was prepared by bubbling room air through a beaker of water overnight while the zero air solution was prepared by adding excess sodium sulfite to a beaker of water to remove O_2. The O_2 sensors have an accuracy of <8 µM or 5%, whichever is greater, with a resolution of <1 µM.

The air-sea CO_2 flux was estimated using $F_{GAS} = kS\Delta pCO_2$, where k is the gas transfer velocity, S is the gas solubility and ΔpCO_2 is the difference in pCO_2 between the surface ocean and the atmosphere (pCO_{2aq}-pCO_{2atm}). A negative F_{GAS} represents a flux from the atmosphere to the ocean. The gas transfer velocity was estimated using the wind-speed relationship of Wanninkhof (1992). Atmospheric pCO_2 was calculated from hourly dry mole fraction CO_2 at Mauna Loa, converted to wet CO_2 using local reef temperature and pressure. The Mauna Loa site, at $19^o32'$N, is the closest continuous atmospheric CO_2 measurement site to the Media Luna sites at $17^o56'$N. The temperature

data for the Caribbean Time Series (CaTS) site were derived from satellite data at the CaTS location (17^o36'N, 67^0W) using the NOAA Comprehensive Large Array-data Stewardship System (CLASS) for 2007. The salinity data from the CaTS station were measured using a Sea-Bird Electronics SBE19 CTD (conductivity-temperature-depth) unit on a near monthly basis from 1993 to 1999 (Corredor and Morell, 2001). Reported values in Fig. 4.4.1 are the average of monthly values for all measurement years (average $n = 5$ for all months).

4.3.3 Discrete Measurements

To verify the in situ measurement data quality, discrete samples were collected from the reef head (A) and one of the two sites at the reef tail (B or C) frequently during the first 1-2 weeks of each of the deployment, as well as several other times throughout the deployment. When possible, samples were collected on the half hour, to match the SAMI sampling intervals. Samples for total alkalinity (A_T), pH and O_2 were collected using a Van Dorn horizontal water sampler (Wildco) and were dispensed into 200 mL plastic, 600 mL glass and 200 mL glass bottles, respectively with no headspace. Samples were stored in the dark at room temperature until analyzed. A_T samples were analyzed by potentiometric titration with HCl within 3 days of collection using a custom-built Gran titration system (Langdon et al., 2000). Certified reference materials (CRMs) (Dickson et al., 2003) were used to calibrate the accuracy of the HCl titrant. Precision of field samples was ±1.5 μmol kg^{-1}. pH samples were measured spectrophotometrically on the total pH scale within 8 hours of collection on a UV-VIS spectrophotometer (Shimadzu UV-1601) following DOE procedures (Dickson et al., 2007). Precision was

±0.0031 pH units. Molar absorptivity ratios of the mCP indicator were measured on the

Shimadzu at the beginning of the first and third deployments (Table 4.3.1).

Table 4.3.1
Molar absorptivity ratios for the UV/VIS spectrophotometer

Parameter	Summer '07	Fall '08
e_1	0.0033	0.0062
e_2	2.2328	2.2146
e_3	0.1246	0.1296

Molar absorptivity ratios reported at 25 ^{o}C

During the third deployment, Tris seawater buffers (DelValls and Dickson, 1998)

became available to assess the accuracy of the UV-VIS pH measurements. The accuracy

of the Tris measurements was 0.0061 ± 0.0023 pH units for Batch 1 of Tris (uncertainty

of 0.002 pH units). The SAMI pH data was interpolated to a 5 min interval to more

closely match the discrete sampling times. Agreement between the SAMI-pH and the

discrete pH samples was generally within ± 0.02 pH units, with no systematic bias

(mean=0.0006 ± 0.0082, n=86) (Fig. 4.3.2). These relatively large pH differences are

likely due to small spatial and temporal offsets between SAMI measurements and the

discrete samples. Given the rapid changes in pH at this site, time mismatches can lead to

large pH differences. To quality control pCO_2, discrete A_T and SAMI-pH data were used

to model pCO_2 in CO2SYS. The average difference between the SAMI-CO_2 and the

modeled pCO_2 was -0.7 ± 13.8 µatm (n=86, not shown). Oxygen samples were analyzed

using the Winkler titration method. Agreement between the Aanderaa O_2 optodes and

discrete Winkler O_2 measurements was -0.6 ± 3.7 % saturation (n=28).
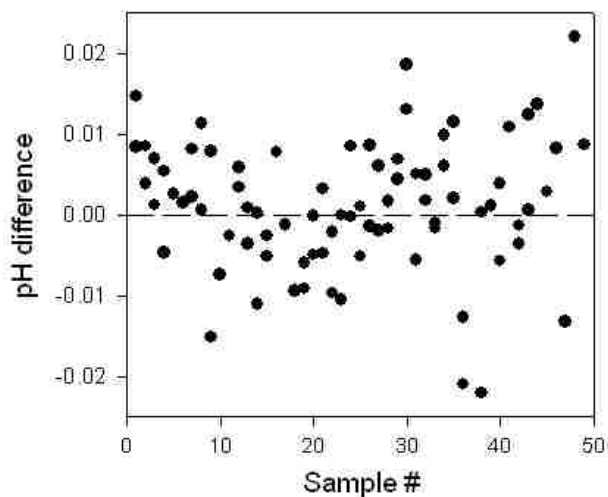
Fig. 4.3.2 Difference between the Puerto Rico SAMI-pHs and discrete UV/VIS pH samples (SAMI-UV/VIS)

4.4 Results

4.4.1 Reef Hydrography

Data from the open ocean Caribbean Time Series (CaTS), located 52 km south of Puerto Rico (17^o36'N, 67^0W), were compared to the hydrographic conditions at Media Luna reef. Water depth at the CaTS station is approximately 2000 meters (Corredor and Morell, 2001). Figure 4.4.1 shows continuous temperature and salinity from the CREWS mooring for 2007-2009. The temperature data were compared to satellite temperature data calculated at the CaTS site for 2007, while salinity data were compared to monthly averages of salinity measured at the CaTS station at a nominal depth of 5 meters. The reef temperature and salinity were very similar to the CaTS site, indicating that open ocean water is the main end-member for reef water and that there are no significant local groundwater or riverine inputs to the reef. These data also showed that our seasonal data from 2007 and 2008 are representative of the typical hydrography based on comparison with the CREWS data from other years. The exception is the rapid drop in salinity

during the fall of 2008 due to a large rain event (discussed below), where the reef took

several months to recover to the open ocean value. CTD casts conducted throughout the

study indicated the entire water column over the reef was always well mixed. Current

meter measurements showed that the mean water flow across the reef was towards the

west-southwest. Tides were diurnal with water depth changes between 0.05 and 0.4

meters.
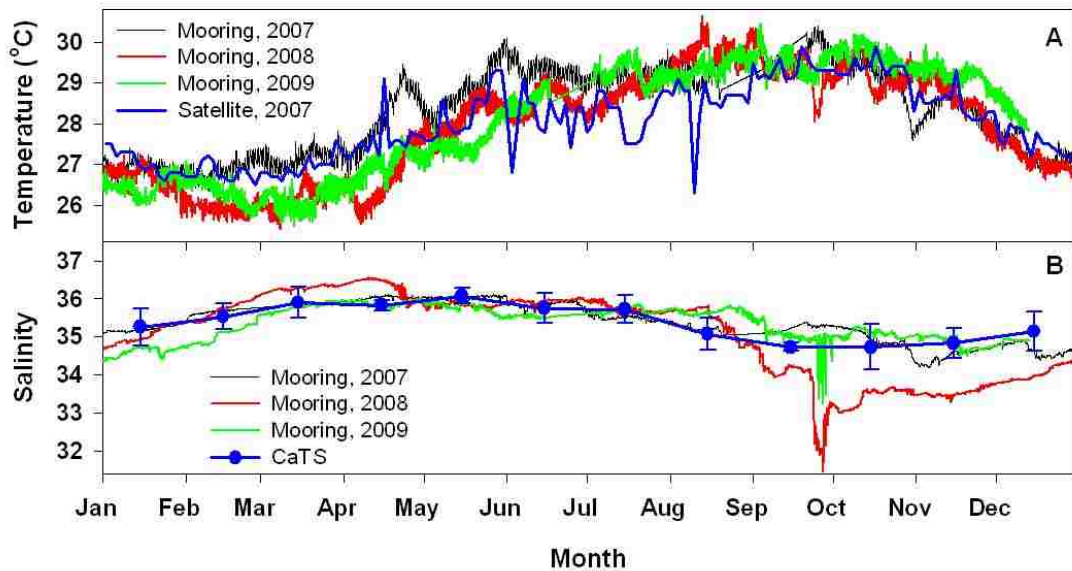
Fig. 4.4.1 (A) Annual temperature record for reef site B from the NOAA CREWS
mooring (hourly) during 2007 (black), 2008 (red) and 2009 (green) and from NOAA
satellite data (blue, every other day) for 2007 from $17.6^{o}N$, $67^{o}W$. (B) Annual salinity
record for reef site B from the NOAA CREWS mooring (hourly) during 2007 (black),
2008 (red) and 2009 (green) and from discrete CTD casts at the Caribbean Time Series
(CaTS) (blue, monthly average of points from 1993-1999, n=5 for each month) located at
$17.6^{o}N$, $67^{o}W$.

Several severe weather events occurred during the study. On August 17, 2007,

during the first deployment, hurricane Dean passed over the reef. The instruments at the

reef head were removed from the water preceding the hurricane. During the third

deployment a tropical depression, that later turned into tropical storm Kate, passed over

Media Luna reef from September 21-23 2008. This storm was accompanied by a large

rain event, with 20.3 cm of rain falling over 12 hours. Tropical storm Omar also passed

over the reef during the third deployment, from October 14-17, 2008. All instruments at

the reef head and tail were removed from the water before the storm and replaced after it

passed Puerto Rico.

4.4.2 Temporal pH Variability

Data for all three seasons at Media Luna reef are shown in Fig 4.4.2. pH, pCO_2,

O_2 and temperature all showed large diel and seasonal variations. Temperature and

salinity ranged between 25.5-30.7 ^{o}C and 31.4-36.3, respectively. pH and pCO_2 ranged

from 7.89-8.17 pH units and 176-613 µatm, respectively with oxygen saturation from 55-

190 %. Mean value, by season, are shown in Table 4.4.1. Diel wind speed variability

was between 3.0 and 12.0 m s^{-1}. Diel ranges represent the difference between the

maxima and minima for a 24 hour period. Discrete pH, O_2 and saturation state samples

are shown in Fig. 4.4.2 for comparison with the in situ data.
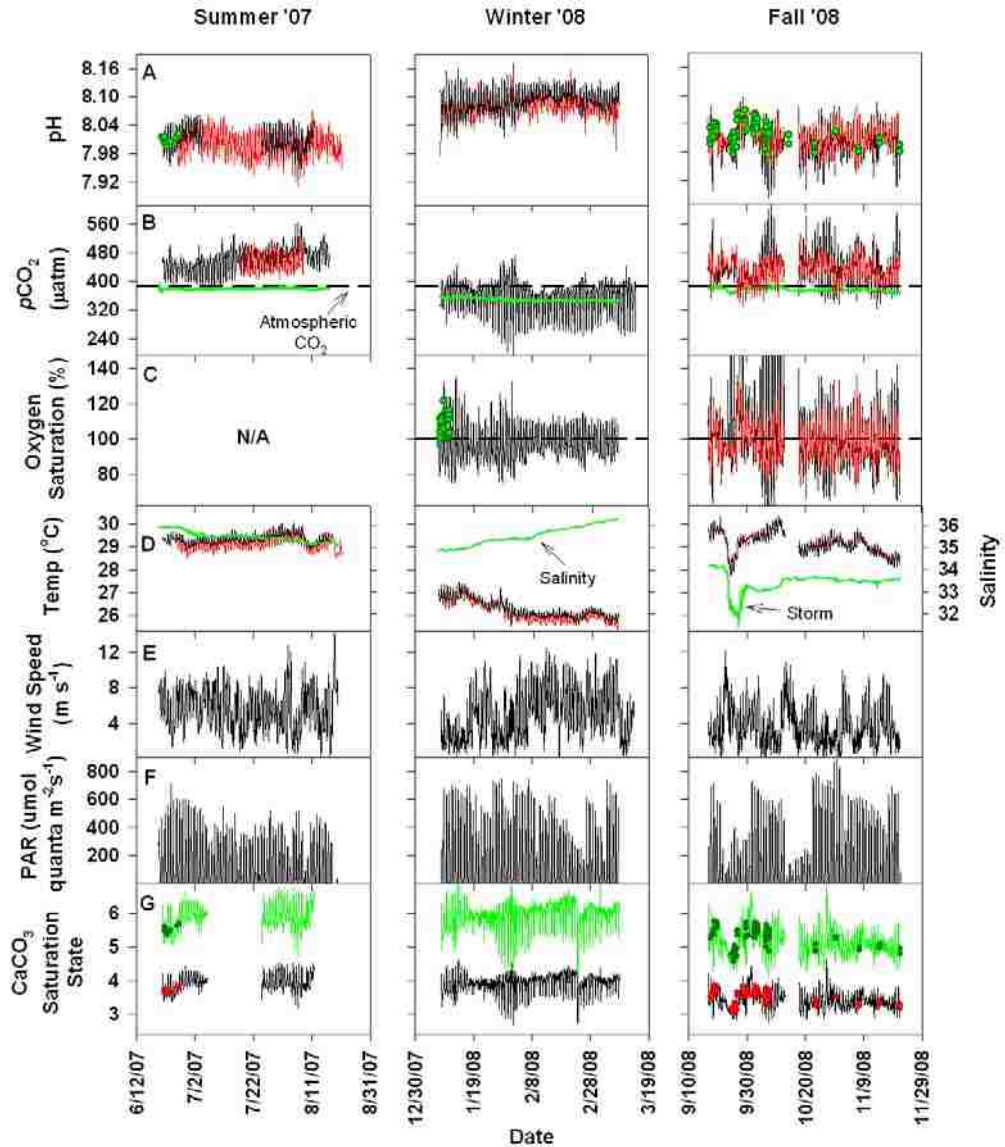
Fig. 4.4.2 (A) pH from the SAMI-pH at the reef head (black) and reef tail (red). (B) pCO_2 the reef head (black) and reef tail (red) The dashed black line shows the average atmospheric pCO_2 value from Mauna Loa (pCO_2=382 µatm). The green line shows estimated open ocean pCO_2 at the reef temperature, calculated using the relationship of Olsen et al. (2004). (C) O_2 from Aanderaa O_2 optodes at the reef head (black) and reef tail (red). No O_2 sensors were deployed during the summer 2007 deployment. The dashed black line shows 100% O_2 saturation. (D) Temperature from the SAMI-pH at the reef head (black) and tail (red) and salinity (green) from the NOAA CREWS mooring at the reef tail site B. (E) Wind speed from the NOAA buoy at reef tail site B. (F) Photosynthetically Active Radiation (PAR) from the NOAA CREWS mooring at the reef tail site B. (G) Aragonite (black) and calcite (green) $CaCO_3$ saturation states modeled from SAMI-pH and SAMI-CO_2 data. Gaps in the fall pH, pCO_2, O_2 and temperature data correspond to when the SAMIs were removed from the reef preceding severe weather.

Table 4.4.1
Average of each measured parameter by season

Parameter	Summer '07	Winter '08	Fall '08
Temperature (^{o}C)	29.3 ± 0.24	26.3 ± 0.40	29.1 ± 0.45
Salinity	35.8 ± 0.22	35.2 ± 0.35	33.8 ± 0.50
PAR (umol quanta m^{-2} s^{-1})	109 ±153	135 ± 199	122 ± 193
O_2 Saturation (%)	-----	97.5 ± 9.5	101.6 ± 21.6
Wind Speed (m s^{-1})	5.6 ± 2.4	5.0 ± 2.8	3.7 ± 2.2
pH	8.01 ± 0.02	8.09 ± 0.02	8.00 ± 0.03
pCO_2 (µatm)	460 ± 32.5	356 ± 42.8	437 ± 43.7
Aragonite	3.94 ±0.24	3.94 ± 0.25	3.42 ± 0.26
Calcite	5.90 ± 0.36	5.95 ± 0.38	5.13 ± 0.39

The summer 2007 deployment showed high temperatures with a relatively flat

seasonal mean (~1 ^{o}C) and diel changes of 0.2-0.7 ^{o}C. Salinity decreased by 0.9, in

keeping with the oceanic salinity trend (Fig. 4.4.1B). Large diel pH variability was

observed in the summer, with changes of 0.04-0.15 pH units per day. Water on the reef

was almost always supersaturated with respect to atmospheric CO_2 values (~386 µatm,

Fig. 4.4.2B), with diel pCO_2 changes of 34-129 µatm. The winter deployment had the

coldest temperatures, with a mean seasonal decrease of ~2 ^{o}C and a diel temperature

range of 0.2-1.0 ^{o}C (Fig 4.4.2D). Salinity increased over time from 34.8 to 36.3, again in

keeping with open ocean salinity trends (Fig. 4.4.1B). The highest average PAR values at

depth were observed in winter, most likely due to clearer waters during the colder winter

months. Average pH was highest during the winter, with diel changes of 0.02-0.14 pH units, very similar to the daily summer changes. Average pCO_2 was lowest during the winter and was mostly undersaturated with respect to the atmosphere, with a diel pCO_2 range of 73-298 µatm. The diel range in O_2 was between 13-58 % saturation and was negatively correlated with average wind speeds ($r^2 = 0.71$). Diel variability in wind speed was between 2.4 and 10.1 m s^{-1}.

The fall showed a return to higher temperatures, with a mean seasonal change of ~2.6 °C and diel changes of 0.04-1.0 °C (Fig. 4.4.2). Temperatures at the reef head and reef tail were nearly identical (mean difference = 0.08 °C) after moving the reef tail instruments from site B to site C. Salinities were the lowest of any season due in part to lower salinity oceanic waters (Fig 4.4.1B) on the reef. Salinity was further reduced by freshwater inputs from storms (Fig 4.4.2D). The two time periods with extremely low PAR values also correspond to storms (9/22/08 and 10/14/08). pH showed the largest diel variability of any season with changes of 0.01-0.18 pH units, as well as the lowest absolute pH value at 7.89 pH units. pCO_2 reached the highest value of any season (613 µatm) and was mostly supersaturated with respect to the atmosphere, with a diel pCO_2 range of 6-232 µatm. The oxygen diel variability was 14-132 % saturation at the reef head and 4-62 % saturation at the reef tail. The diel range in O_2 was negatively correlated with the average wind speed ($R^2 = 0.61$ m s^{-1}). Diel variability in wind speed was between 2.0 and 9.7 m s^{-1}, similar to winter values.

4.4.3 Spatial pH Variability

In addition to temporal pH variability, spatial pH variability was also examined across the La Parguera reef system. The location of the reefs studied is shown in Fig. 4.4.3.
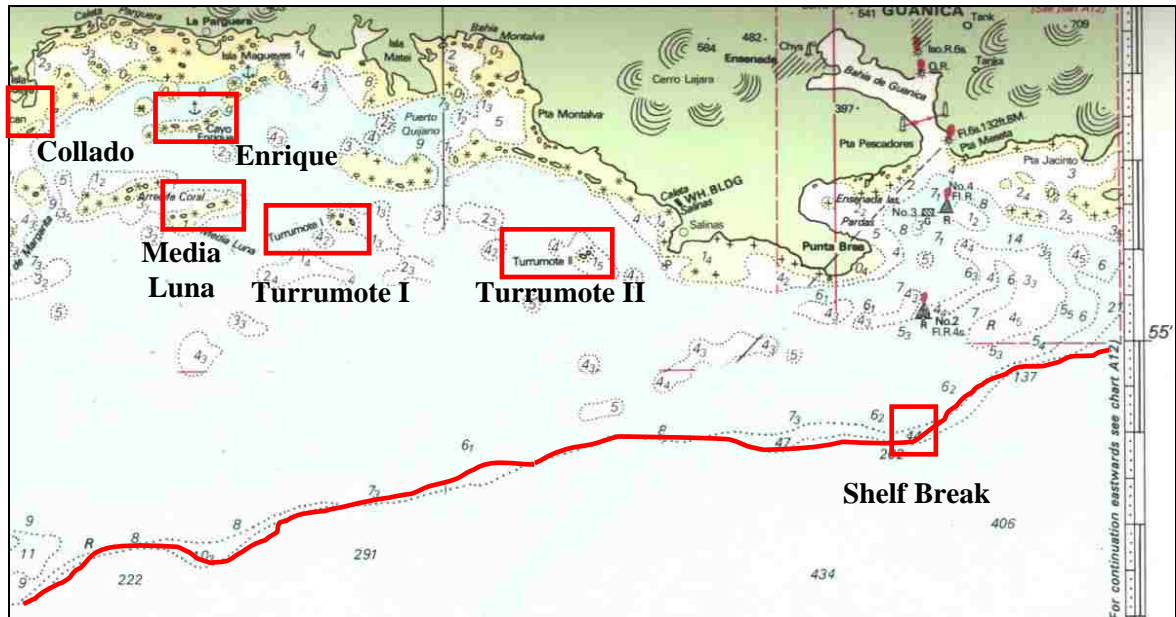
Fig. 4.4.3 Map of the coral reef system off the southwest coast of Puerto Rico at La Parguera.

Figure 4.4.2 shows the pH, pCO_2, O_2 and temperature variability between the head and tail of Media Luna measured with in situ sensors. pH and temperature differences between the reef head and tail are less pronounced during the fall deployment because the Media Luna reef tail site was moved from site B to site C (Fig. 4.3.1). During the summer and winter seasons, pH, pCO_2 and temperature were higher at the reef head. The mean differences between the reef head and tail for each parameter are shown in Table 4.4.2. The monthly differences in pH, pCO_2, O_2 and temperature are shown in Fig. 4.4.3.

Table 4.4.2 Average difference in raw data between the Media Luna reef head and tail sites (head-tail) for each measured parameter by season

Parameter	Summer '07	Winter '08	Fall '08
pH (pH units)	0.011 ± 0.022	0.012 ± 0.021	0.008 ± 0.08
pCO_2 (µatm)	24.0 ± 26.2	-----	6.0 ± 28.4
O_2 Saturation (%)	-----	-----	6.9 ± 26.5
Temperature (^oC)	0.2 ± 0.1	0.1 ± 0.1	-0.04 ± 0.08
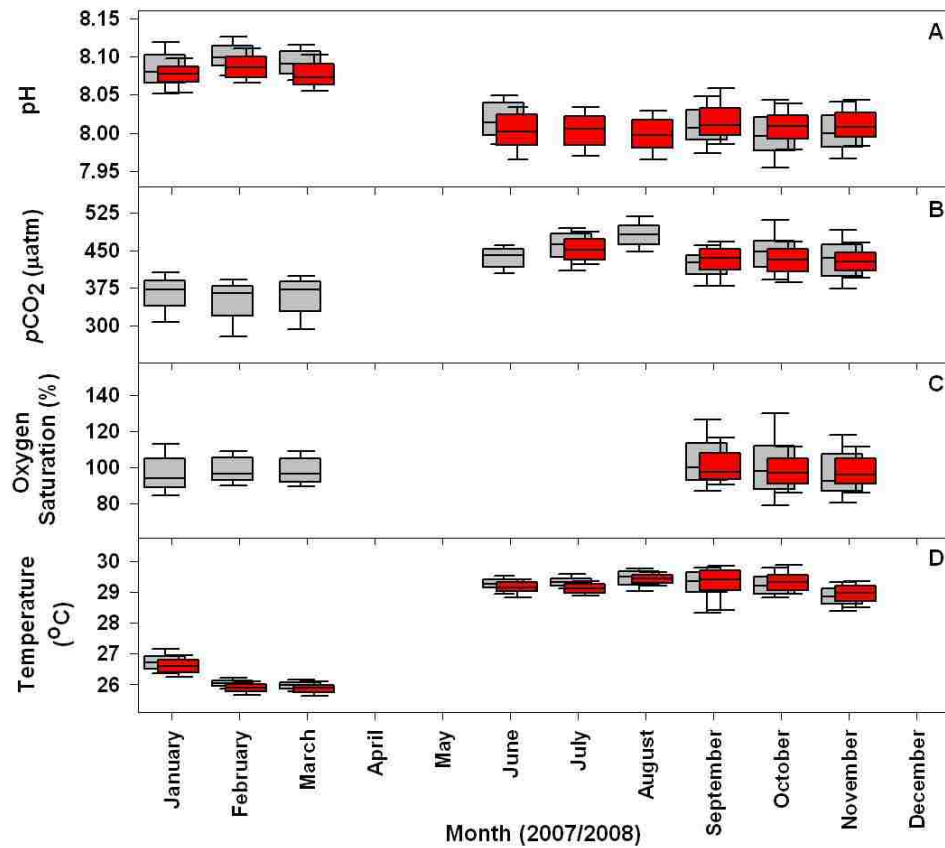
Fig. 4.4.4 Monthly changes in spatial variability of each parameter over an annual cycle. Data in gray are from reef head site A. Data in red are from reef tail site B for Jan-Aug. and reef tail site C for Sept-Nov. For each box the center line is the monthly median, the top and bottom of each box are the 75th and 25th percentiles and the top and bottom whiskers are the 90th and 10th percentiles.

Figure 4.4.5 shows the pH variability at sites across the La Parguera shelf, measured from discrete samples. For a given time, the shelf break site showed the highest pH values with pH generally decreasing across the La Parguera reef shelf from east to west. This trend matches the general water flow of east to west across the shelf. Since calcification produces CO_2 and lowers pH, water that has interacted with numerous reefs across the shelf is expected to have a lower pH. As with the in situ samples, pH at the head of Media Luna was higher compared to pH at the reef tail. Enrique reef is directly inshore of Media Luna and experiences similar or slightly lower pH values. The Turrumote I site showed lower pH values, despite being further west compared to the Turrumote II site. This is likely a function of local reef processes and the time difference between sample collections at the two sites.
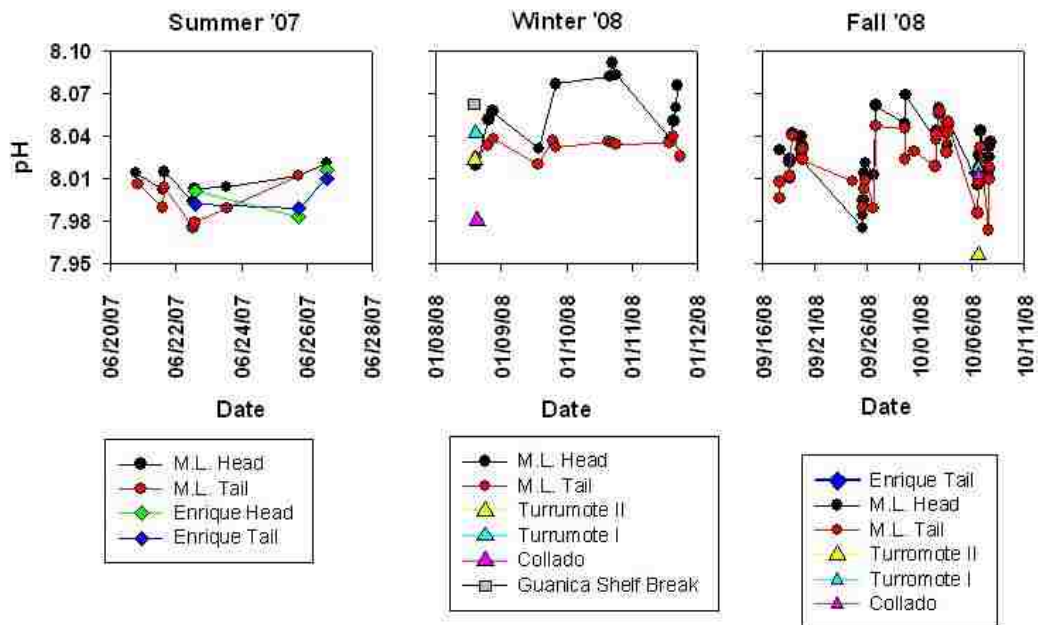
Fig. 4.4.5 Spatial pH variability across the La Parguera reef shelf by season. M.L = Media Luna.

4.5 Discussion

4.5.1 Short-Term and Seasonal Variability

The monthly ranges for temperature, pH and pCO_2 are shown in Fig. 4.5.1. Both temperature and pCO_2 started out low in the winter, increased throughout the summer and started to decrease slightly in the fall. The pH showed the expected inverse relationship with pCO_2. In order to determine how the ~3.5 ^{0}C seasonal temperature change influenced the seasonal pH and pCO_2 variability, the pH and pCO_2 data were temperature corrected to the annual mean temperature, 28 ^{o}C (Fig. 4.5.1B-C). The temperature correction reduced the seasonal change in pH by 50%, from 0.1 pH units to 0.05 pH units. The mean seasonal pCO_2 range was reduced by 54%, from 117 µatm to 63 µatm. The remaining seasonal variability is likely dominated by a combination of organic carbon, $CaCO_3$ production/dissolution and air-sea gas fluxes. In order to determine the balance between these two processes, we examined A_T values on the reef and offshore. Reef A_T was determined from discrete sampling points, while offshore A_T was calculated from the temperature/salinity relationship of Lee et al. (2006) at the CaTS site (Fig. 4.5.2). The offshore values showed increasing A_T throughout the winter and spring with a maximum in May, decreasing A_T throughout the summer and a return to increasing A_T in the fall. When salinity-normalized to a mean of 35, the offshore A_T values do not vary of the annual cycle since dilution is the main factor affecting A_T in the open oceans. The reef A_T followed the offshore seasonal pattern until mid-September at the onset of the storm season, after which the reef alkalinity decreased significantly.
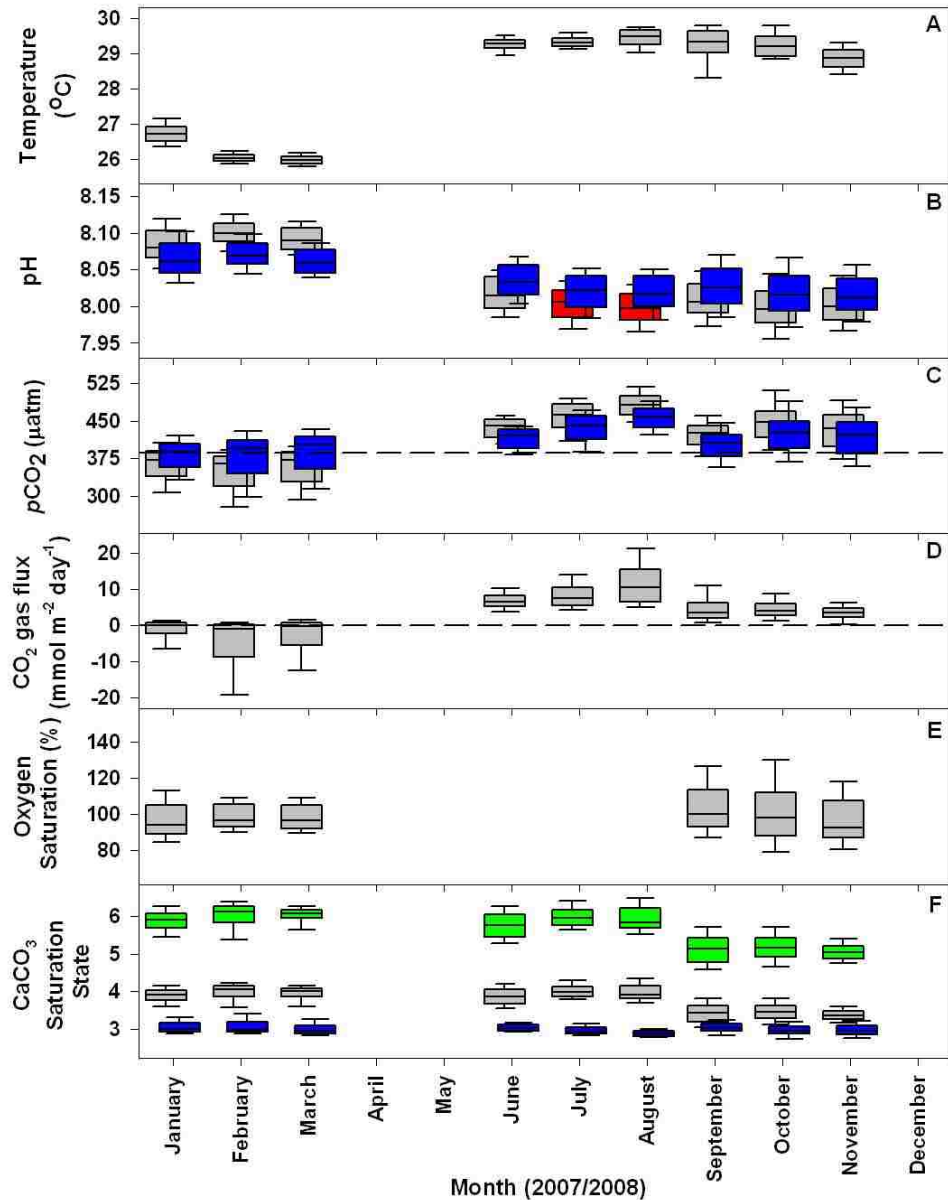
Fig. 4.5.1 Monthly changes in each parameter over an annual cycle. All data in A-E are from the reef head site A with the exception of the July and August pH data (shown in red). For plots A-D the gray and red boxes show measured data while the blue boxes show the measured data after it was corrected to the annual mean temperature of 28 ^{o}C. For plot D, a negative CO_2 flux is from the atmosphere to the ocean. For plot F, the gray boxes are the aragonite saturation state and the green boxes are the calcite saturation state. Blue boxes represent the projected aragonite saturation if pCO_2 increases to 500 μatm. For each box the center line is the monthly median, the top and bottom of each box are the 75th and 25th percentiles and the top and bottom whiskers are the 90th and 10th percentiles.

In order to determine if the differences between the reef and offshore A_T were due

to dilution, we normalized the reef A_T to a salinity of 35. At a constant salinity, the

remaining differences between reef and offshore waters should be due to local processes

on the reef. In January, reef A_T is within 15 ± 13 μmol kg^{-1} of the offshore value while

late February reef values are slightly lower compared to offshore values (difference = 25

± 7 μmol kg^{-1}). In the summer there was a marked decrease in reef A_T relative to

offshore waters (difference = 42 ± 4 μmol kg^{-1}). This difference can indicate

calcification on the reef, which can sustain the observed pCO_2 supersaturation throughout

the summer season (Fig. 4.5.1C). During the fall season, salinity-normalized A_T for

October were significantly higher than offshore values (difference = -57 ± 9 μmol kg^{-1}).

The high salinity-normalized A_T is likely driven by terrestrial inputs as a result of the

storm, rather than significant $CaCO_3$ dissolution. The pCO_2 would be expected to

decrease by 25 μatm if the A_T decrease was due to $CaCO_3$ dissolution, but pCO_2 was

observed to increase. Terrestrial inputs have been shown to contribute to high alkalinity

and pCO_2 in coastal areas (Kawahata et al., 2000).
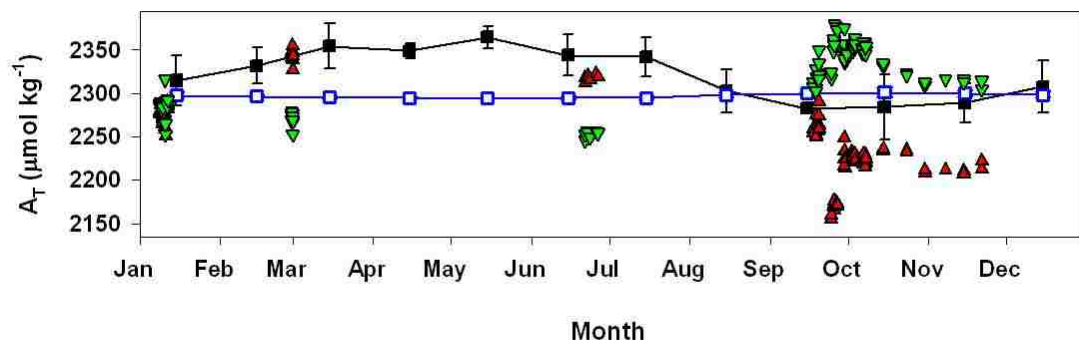
Fig. 4.5.2 Filled black squares show monthly averaged A_T for the offshore CaTS site
calculated from the Lee et al. (2006) relationship. Open blue squares show the monthly
averaged CaTS A_T corrected to a mean salinity of 35. Red triangles show measured
discrete A_T points from Media Luna reef. Green triangles show Media Luna A_T corrected
to a mean salinity of 35.

The differences in the salinity-normalized A_T from January to June at the reef and offshore sites were used to calculate the seasonal pH and pCO_2 changes due to calcification. The A_T at the offshore site decreased 3 µmol kg^{-1} from January to June, while the reef A_T decreased 31 µmol kg^{-1}, for a net reef A_T decrease of 28 µmol kg^{-1}. Assuming a A_T:DIC ratio of 2:1 for calcification, the difference in A_T and DIC from winter to summer were used to model the seasonal changes in pH and pCO_2 in CO2SYS (Pierrot et al., 2006). The initial A_T and DIC used for modeling were 2283 and 1954 µmol kg^{-1}, respectively, with initial DIC values estimated using CO2SYS. The resulting pH and pCO_2 seasonal changes were -0.02 pH units and +15 µatm. Combining the temperature and calcification effects, the remaining winter to summer pH and pCO_2 seasonal changes were -0.03 pH units and 48 µatm, respectively. These values indicate that calcification and temperature alone were not driving all of the supersaturation in pCO_2 seen during the summer and fall seasons (Fig. 4.5.1D). The terrestrial-influenced A_T values in the fall did not allow a similar calculation of calcification between the summer and fall seasons. The remaining pCO_2 supersaturation in the summer is likely driven by organic carbon inputs from local mangrove forests. The southwestern coast of Puerto Rico contains 995 ha of mangroves, as well as several offshore mangrove colonies on emergent portions of the reef (Cintrón et al., 1978; Garcia et al., 1998). Mangroves have been shown to be sources of organic carbon to the surrounding water column, leading to high pCO_2 values (Borges et al., 2005; Borges et al., 2003; Bouillon et al., 2007; Chen and Borges, 2009; Koné and Borges, 2008). The seasonality of organic carbon inputs from mangroves has not been well studied (Borges et al., 2003), but Koné and Borges (2008) found pCO_2 differences between the dry and rainy seasons in waters

surrounding mangrove forests, with higher pCO_2 during the summer to fall rainy season and lower pCO_2 during the winter to spring dry season. At Media Luna reef, organic carbon inputs from the mangroves are highest in the summer and decreasing throughout the fall into the winter season to account for most of the observed pCO_2 supersaturation (Fig. 4.5.1D), after the temperature and calcification corrections.

The variability in O_2 during the winter and fall was partially driven by changes in wind speed. Oxygen variability was high when wind speeds were lower (< 6 m s^{-1}) (Fig. 4.5.3). Higher wind speeds increase O_2 gas exchange, reducing the effect that in situ production has on O_2 and bringing water saturation values closer to air saturation (100%).
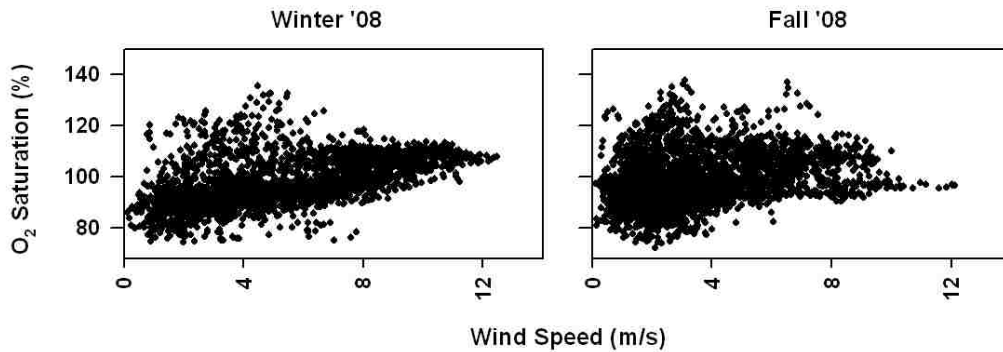
Fig 4.5.3 Relationship between O_2 and wind speed

The relationship between the pH or pCO_2 and O_2 are shown in Figures 4.5.4A and B. Lower O_2 saturation correlates with higher pCO_2 and lower pH values, as well as larger variability in the pCO_2 and pH data. For both pCO_2 and pH, the variability with O_2 was higher in the fall than the winter. Figure 4.5.4C shows the relationship between pH and pCO_2 for each season. The modeled pH and pCO_2 relationships under Redfield (DIC:A_T of 106:18) and calcification (DIC:A_T of 1:2) scenarios are shown in Fig. 4.5.4D. The two

scenarios produce similar results and it is not possible to discern if either process is

dominating given the scatter of the data in Fig. 4.5.4C.
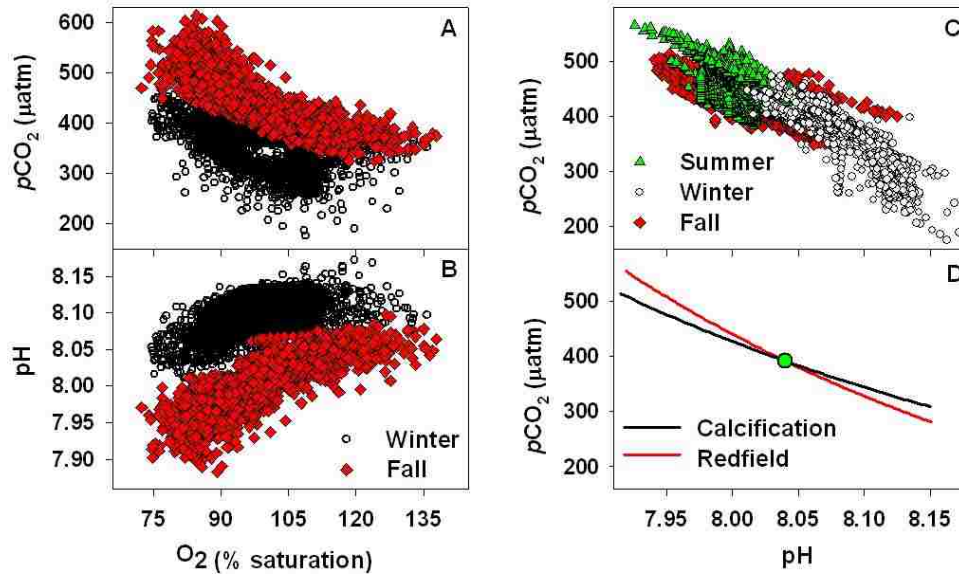
Fig. 4.5.4 (A) pCO_2-O_2 correlation plots for winter (R^2=0.8103) and fall (R^2=0.6654).
(B) pH-O_2 correlation plots for winter (R^2=0.8075) and fall (R^2=0.6736). (C) pCO_2-pH
correlation plots for summer (R^2=0.4664), winter (R^2=0.7501) and fall (R^2=0.6563).
Summer data shown in filled green triangles, winter data in open black circles and fall
deployment in filled red diamonds. (D) Modeled relationships, DIC and A_T are varied by
the Redfield ratio, 106:18 (red) and DIC and A_T are varied by 1:2 for calcification
(black). For the modeled correlations temperature=28.3 ^{o}C and salinity=34.8. The
starting point is shown by the green dot (A_T=2251 and DIC=1932).

In addition to establishing the seasonal inorganic carbon changes on the reef, the

in situ data provided the opportunity to examine extreme events, such as tropical storms,

that would be extremely difficult to study with discrete sampling. Figure 4.5.5 shows a

blow up of the changes that occurred when tropical storm Omar passed over Puerto Rico

during the fall deployment. The sharp dips in temperature and salinity were due to the

large amount of rain from the storm (20.3 cm of rain over 12 hours). The decreased

temperature and light levels led to a decrease in the diel variability of pH and pCO_2 from the average of 0.092 pH units and 130 µatm to a seasonal minimum of 0.012 pH units and 5 µatm. Approximately one week after this rain event a large algal bloom occurred (Fig. 4.5.5F). Additional photosynthesis and respiration from this bloom were most likely driving the very large diel variability seen in early October, with diel ranges of 0.167 pH units and 232 µatm in pH and pCO_2, respectively, representing seasonal maxima.

4.5.2 CO_2 Gas Flux

While the reef hydrographic properties are controlled by open ocean source waters, the reef biogeochemical composition is strongly imprinted by local processes. Using the algorithm of Olsen et al. (2004) to estimate open ocean pCO_2 at reef temperatures (Fig. 4.4.2), the summertime pCO_2 is expected to almost always be undersaturated with respect to the atmospheric value (~386 µatm), with an average value of 380 ± 2.5 µatm. The open ocean pCO_2 values show very small diel variability (4 ± 1.5 µatm) compared to summertime diel pCO_2 changes on the reef (34-129 µatm). During the winter, the estimated open ocean pCO_2 (Olsen et al., 2004) was always below atmospheric saturation, with the lowest mean for the year at 349 ± 4.1 µatm. During the fall, open ocean pCO_2 estimates return to near saturation levels (mean $= 377 \pm 4.6$ µatm).
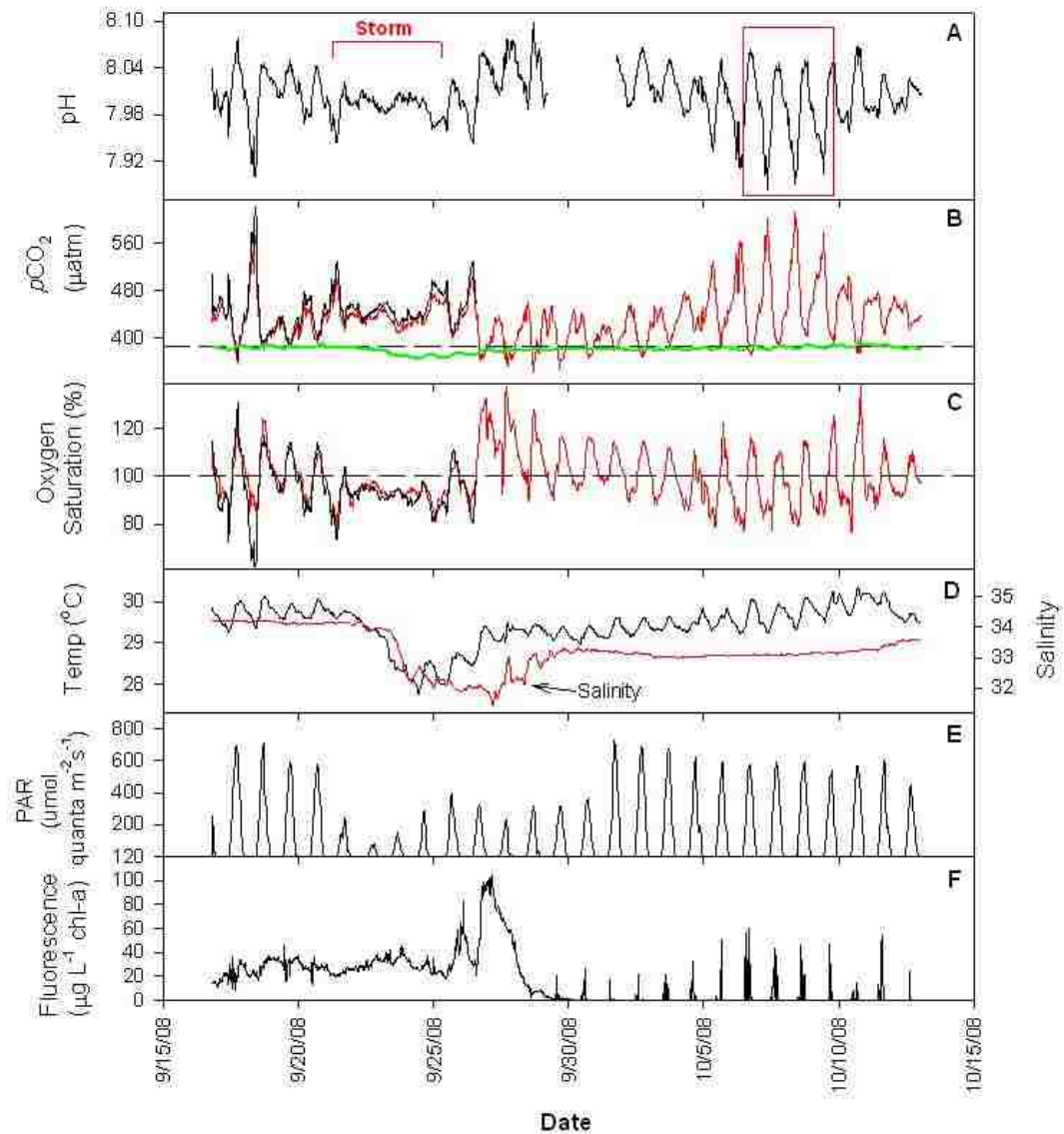
Fig. 4.5.5 Blowup of the fall storm data. (A) pH from the SAMI-pH at the reef head (black). The red bracket shows the storm period and the red box shows the large diel changes after the storm. The gap in the pH data is due to instrument problems. (B) pCO_2 from two SAMI-CO_2s at the reef head (instrument #1 in black, instrument #2 in red). The dashed black line shows the average atmospheric CO_2 value from Mauna Loa (pCO_2=385.7 µatm). The green line shows estimated open ocean pCO_2 at the reef temperature, calculated using the relationship of Olsen et al. (2004). (C) O_2 from two Aanderaa O_2 optodes at the reef head (instrument #1 in black, instrument #2 in red). The dashed black line shows 100% O_2 saturation. (D) Temperature (black) from the SAMI-pH and salinity (red) from the NOAA CREWS mooring at the reef tail site B. (E) Photosynthetically Active Radiation (PAR) from the NOAA CREWS mooring at the reef tail site B. (F) Fluorescence from a Chelsea Instruments Minitracka attached to the SAMI-CO_2.

98

These observations are similar to those by Bates et al. (2001), where the local reef

dramatically alters the open ocean biogeochemistry. The estimated pCO_2 values also

show that offshore waters should be a sink for CO_2 year round. These estimates match

measured pCO_2 values from the south eastern Caribbean (Olsen et al., 2004) where the

annual pCO_2 change was ~30 μatm, and pCO_2 values were at or below saturation year-

round.

　　　　To determine if Media Luna reef was a source or a sink of CO_2 to the atmosphere,

we calculated CO_2 gas fluxes for each season as well as annually (Table 4.5.1). The

summer and fall seasons both showed positive CO_2 fluxes out of the ocean (9.18 and 4.30

mmol m^{-2} day^{-1}, respectively), with the largest values in the summer. Bates et al. (2001)

found similar mean flux rates for the fall season (3.3 ± 4.6 mmol m^{-2} day^{-1}) at Hog Reef

Flat, Bermuda. The CO_2 gas flux was negative in the winter (-3.46 mmol m^{-2} day^{-1}). The

annual air-sea flux, calculated by interpolating measured pCO_2 values between

deployments to create continuous pCO_2 for one combined year, is positive (1.19 mol m^{-2}

year^{-1}). Wind speeds were continuous year-round. The combined annual record for CO_2

gas flux by month is shown in Fig. 4.5.1D. Data from five coral reef systems compiled

by Fagan and Mackenzie (2007) showed very similar annual CO_2 fluxes (between 1.2 and

1.8 mol m^{-2} year^{-1}) with the exception of one reef near equilibrium (0.1 mol m^{-2} year^{-1}).

Table 4.5.1 pCO_2 gas flux by season and annually

Parameter	Summer '07	Winter '08	Fall '08	Annually
pCO_2 gas flux	9.18 ± 5.04 (mmol m^{-2} day^{-1})	-3.46 ± 6.79 (mmol m^{-2} day^{-1})	4.30 ± 3.36 (mmol m^{-2} day^{-1})	1.19 ± 2.11 (mol m^{-2} year^{-1})

Negative values show a flux from the atmosphere to the ocean

4.5.3 Saturation State

Declines in coral calcification have been shown to be related to $CaCO_3$ saturation state decreases, caused by carbonate decreases (Gledhill et al., 2008; Langdon and Atkinson, 2005). In order to examine potential coral health at Media Luna reef, we modeled $CaCO_3$ saturation states for each season using pH and pCO_2 data (Fig. 4.4.2G) in CO2SYS (Pierrot et al., 2006) with K_1 and K_2 from Mehrbach et al. (1973) refit by Dickson and Millero (Dickson and Millero, 1987), KSO_4 from Dickson (Dickson, 1990) and pH on the total scale. Despite problems with the pH-pCO_2 combination for modeling other inorganic carbon parameters, this pairing has been shown to be viable for calculating saturation states (Cullison et al., in preparation, shown in Ch. 3). The aragonite (Ω_{Ar}) and calcite (Ω_{Ca}) $CaCO_3$ saturation states are based on the CO_3^{2-} concentration and are therefore less sensitive to small errors in the pH and pCO_2 data, compared to modeling of A_T or DIC (Cullison et al., in preparation). Data from discrete pH and A_T measurements were used to model 'discrete' Ω_{Ar} and Ω_{Ca} values (Fig 4.4.2G) as an accuracy check of the saturation states modeled from in situ data. The difference between the discrete and in situ modeled data was 0.46 ± 0.12 and 0.40 ± 0.19 for aragonite and calcite, respectively. Mean values for Ω_{Ar} and Ω_{Ca}, by season, are shown in Table 4.4.1. Diel Ω_{Ar} changes were 0.64 ± 0.23, 0.83 ± 0.35 and 0.72 ± 0.30 for summer, winter and fall, respectively (Fig. 4.4.2G). Ω_{Ca} diel changes for summer, winter and fall were 0.95 ± 0.34, 1.25 ± 0.52 and 1.08 ± 0.44, respectively (Fig. 4.4.2G). The large diel variability in saturation states was positively correlated with diel pH changes on the reef (R^2=0.2382, n=155, p < 0.001). Mean variability in saturation states over weekly time scales did not show a significant correlation with the spring and neap tidal cycles during

any of the three seasons, with R^2 values that were less than or equal to 0.0004 for all three

seasons (Fig. 4.5.6).
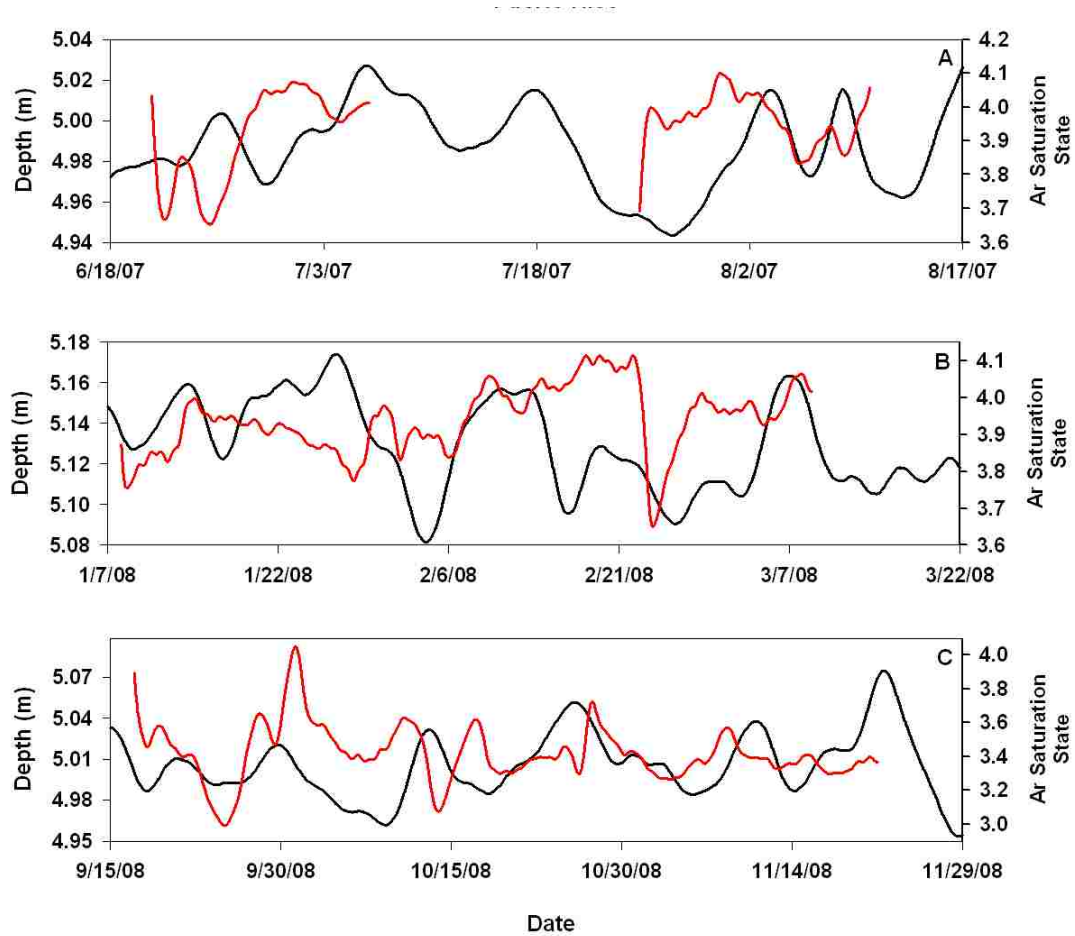
Fig. 4.5.6 30 hour filtered water depth (black) from the CREWS mooring and Ar
saturation state (red) for Media Luna site A for the summer (A), winter (B) and fall (C)
seasons.

The composite annual monthly saturation state values are shown in Fig. 4.5.1F.

Both calcite and aragonite values were fairly consistent from January to August with little

to no decrease in the saturation state from winter to summer. The winter saturation states

are close to the summer values, despite significantly higher pH values, due to the ~3 ^{o}C

lower winter temperatures, which increases the solubility of aragonite and calcite. If the winter pH and pCO_2 were used to model Ω_{Ar} at the summer temperature, the Ω_{Ar} would be approximately 0.4 higher than the observed winter values. In the fall, saturation decreased (Fig. 4.4.2G, Fig. 4.5.1F) due to dilution of the carbonate concentration by lower salinity waters on the reef at this time, similar to the fall decrease in A_T (Fig. 4.5.2). Gledhill et al. (2008) showed mean Ω_{Ar} values of 3.9 ± 0.10 for both January and August 2006 in the Caribbean Sea near southwest Puerto Rico, which compare favorably with our mean seasonal values (3.4-3.9). In addition to laboratory studies of saturation and calcification, data from naturally occurring reefs has been used to help establish saturation state limits for calcification. Kleypas et al. (1999a) have shown that Ω_{Ar} values of 3.5-4.0 are adequate, 3.0-3.5 are low and < 3.0 are extremely marginal, based on the current distribution of reefs worldwide. In waters where Ω_{Ar} is < 3.0, corals are not likely to calcify at rates higher than dissolution (Gledhill et al., 2008). Following these guidelines, Media Luna reef reaches extremely marginal values over short periods during the winter and fall seasons (Fig. 4.4.2G), but monthly averages are within the low to adequate range year round (Fig. 4.5.1F).

Atmospheric CO_2 values are expected to continue to rise from current values of ~386 µatm, possibly up to 500 µatm (by 2035-2065) or higher (Meehl et al., 2007), which will also lead to an increase in oceanic pCO_2. To estimate the effect this increase could have on the pH dynamics of the reef, we added 120 µatm to the measured pCO_2 from each season and modeled the future pH using this future pCO_2, a constant A_T of 2250 µmol kg^{-1} at the measured reef temperature and salinity. The pCO_2 increase led to average pH decreases of 0.11 ± 0.020, 0.12 ± 0.018 and 0.08 ± 0.013 for the summer,

winter and fall seasons, respectively. Ω_{Ar} and Ω_{Ca} were then re-modeled using the

predicted $p\mathrm{CO}_2$ and pH data (Fig. 4.5.1F). While measured monthly averages of Ω_{Ar}

were always above 3.0, Ω_{Ar} is projected to be at the threshold value of 3.0 year-round on

the reef if $p\mathrm{CO}_2$ increases to 500 µatm, which could occur within the next 15 years

(Meehl et al., 2007). These values will put the reef at the extremely marginal

calcification level throughout the year. Calcite saturation is projected to decrease to a

new range of 3.9-5.5 (not shown).

4.5.4 Calcification

In order to determine calcification rates at Media Luna, we compared O_2 and pH

and $p\mathrm{CO}_2$ measurements, in terms of DIC. Eqn. (4.1) shows the mass balance for the

system,

$$H \frac{\Delta DIC}{dT} = F_{gas} - F_{NCM} - F_{CaCO3} \tag{4.1}$$

$$H \frac{DO}{dT} = F_{gas} - F_{NCM} \tag{4.2}$$

$$F_{NCM} = F_{NCMO2} * \mathbf{Re}\mathrm{dfield} \tag{4.3}$$

where H is mixed layer depth, $\Delta DIC/dT$ is the change in DIC per time (either from

oxygen or pH), F_{gas} is the flux due to gas exchange, F_{NCM} is the flux due to net

community metabolism and F_{CaCO3} is the flux due to calcification. The $\Delta DIC/dT$ from

oxygen is calculated from Eqns. (4.2-4.3). The F_{NCM} is calculated from the flux due to

oxygen ($F_{NCM\ O2}$) multiplied by the Redfield ratio (Redfield). As stated above, salinity

records did not indicate any significant freshwater inputs except for the Fall 2008 storm

at the end of September, so we neglected the effects of entrainment in our calculations.

The flux due to calcification can be determined from the difference in H ΔDIC/dT due to

pH and oxygen changes. Changes in oxygen are only affected by F_{gas} and F_{ncm}, while

changes in pH and pCO_2 are affected by all three fluxes shown in Eqn. (4.1). After

correcting the oxygen and pH records for gas exchange the difference in H ΔDIC/dT is

F_{CaCO3}. The oxygen data were corrected for gas exchange and then converted to an O_2

flux. This oxygen flux was converted to a DIC flux using a Redfield ration of -106/138.

The in situ pH data were combined with an interpolated A_T record (from discrete

measurements) to model DIC over the winter and fall deployments. This DIC record was

then converted to a DIC flux. Figures 4.5.7 and 4.5.8 shows the DIC fluxes and the

differences between them in two different units.
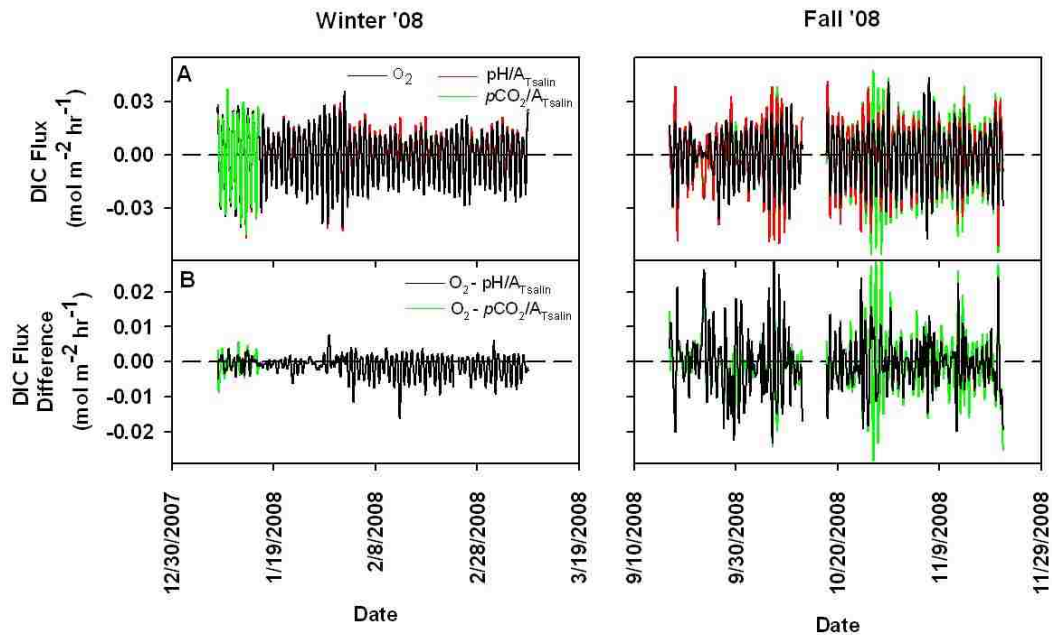
Fig. 4.5.7 (A) 8 hour low pass filtered DIC fluxes due to oxygen (black), pH/A_{Tsalin} (red) and pCO_2/A_{Tsalin} (green). (B) The difference in DIC fluxes. pH/A_{Tsalin} flux-O_2 flux in black, pCO_2/A_{Tsalin} flux-O_2 flux in green. Negative DIC difference values indicate calcification. The dashed black line shows the zero line. The DIC flux is in mol m^{-2} hr^{-1}.
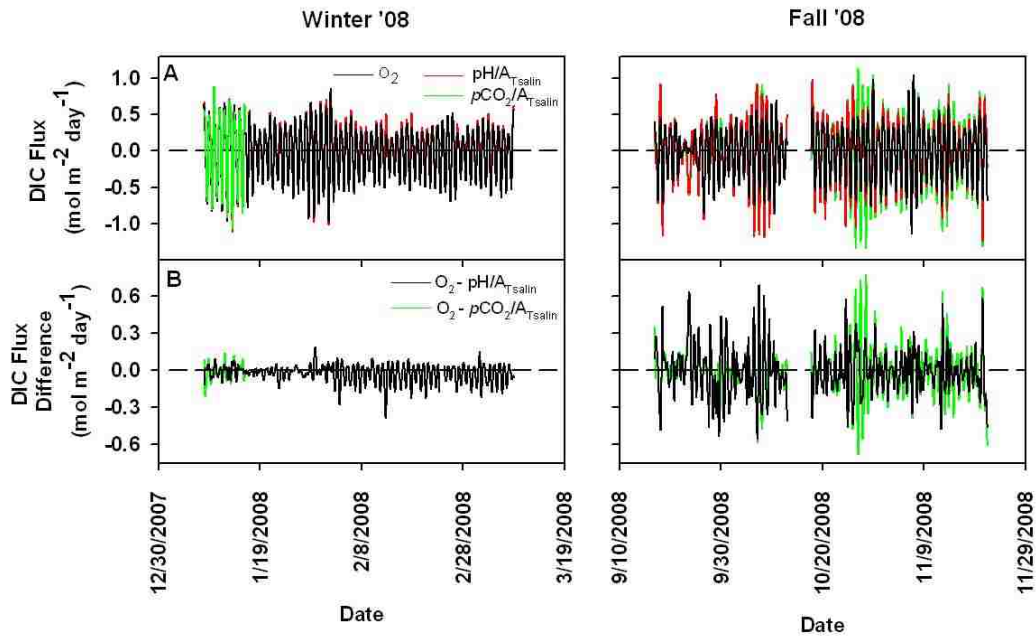
Fig. 4.5.8 (A) 8 hour low pass filtered DIC fluxes due to oxygen (black), pH/A_{Tsalin} (red) and pCO$_2$/A_{Tsalin} (green). (B) The difference in DIC fluxes. pH/A_{Tsalin} flux-O$_2$ flux in black, pCO$_2$/A_{Tsalin} flux-O$_2$ flux in green. Negative DIC difference values indicate calcification. The dashed black line shows the zero line. The DIC flux is in mol m^{-2} day^{-1}.

Since A_{Tsalin} is not representative of a calcification A_T, our pH/A_{Tsalin} and pCO2/A_{Tsalin} DIC fluxes will underestimate the calcification signal. Calcification is shown as a positive DIC flux difference, dissolution as a negative DIC flux difference (Fig. 4.5.7B). For the winter season, the O$_2$ and pH/A_{Tsalin} DIC showed small differences (-0.012-0.010 mol m^{-2} hr^{-1}, Fig. 4.5.7B). These fluxes are within the margin of error for the instruments and are therefore not interpreted further as calcification or dissolution. For the fall season, the DIC flux differences (O$_2$-pH/A_{Tsalin}) were larger at -0.023 to 0.029 mol m^{-2} hr^{-1}. Over the entire fall season there was a net dissolution of -1.0919 mol m^{-2}. Average daily values from periods throughout the fall season (9/20/08, 10/18/08, 11/19/08) showed a net dissolution for the day (-0.037, -0.052, -0.063 mol m^{-2} day^{-1}).

These values compare favorably with daily net dissolution from a variety of reef substrates (coral rubble, patch reef, sand bottom) from Molokai reef flat in Hawaii during the winter (-0.020 mol m^{-2} day^{-1}) (Yates and Halley, 2006). During the summer at Molokai reef there was a net calcification of 0.011 mol m^{-2} day^{-1} for a patch reef substrate. Calcification data were not available for the fall season at Molokai reef. Other coral reefs have generally shown net calcification over a 24 hour cycle, rather than the net dissolution seen at Media Luna. On Ishigaki Reef off the southern tip of Japan Kayanne et al. (2005) found a net calcification of 0.036 to 0.131 mol m^{-2} day^{-1} during the fall. On the Palau Islands reef off the westernmost group of the Caroline Islands Kayanne et al. (2005) found a net calcification of 0.097 mol m^{-2} day^{-1} during the summer. On Nature Reserve Reef in the Northern Red Sea Silverman et al. (2007) found net calcification rates of 0.06 ± 0.02 mol m^{-2} day^{-1} for the summer and 0.03 ± 0.02 mol m^{-2} day^{-1} for the winter. Fig. 4.5.9 shows a blowup of two times during the fall deployment, one showing lower calcification rates and one showing higher calcification rates. The pH/A$_{Tsalin}$ and the pCO2/A$_{Tsalin}$ DIC flux records track well with each other (Fig. 4.5.9A) and show very similar offsets compared to the O$_2$ DIC flux (Fig. 4.5.9B), further supporting the accuracy of the pH and pCO$_2$ data.
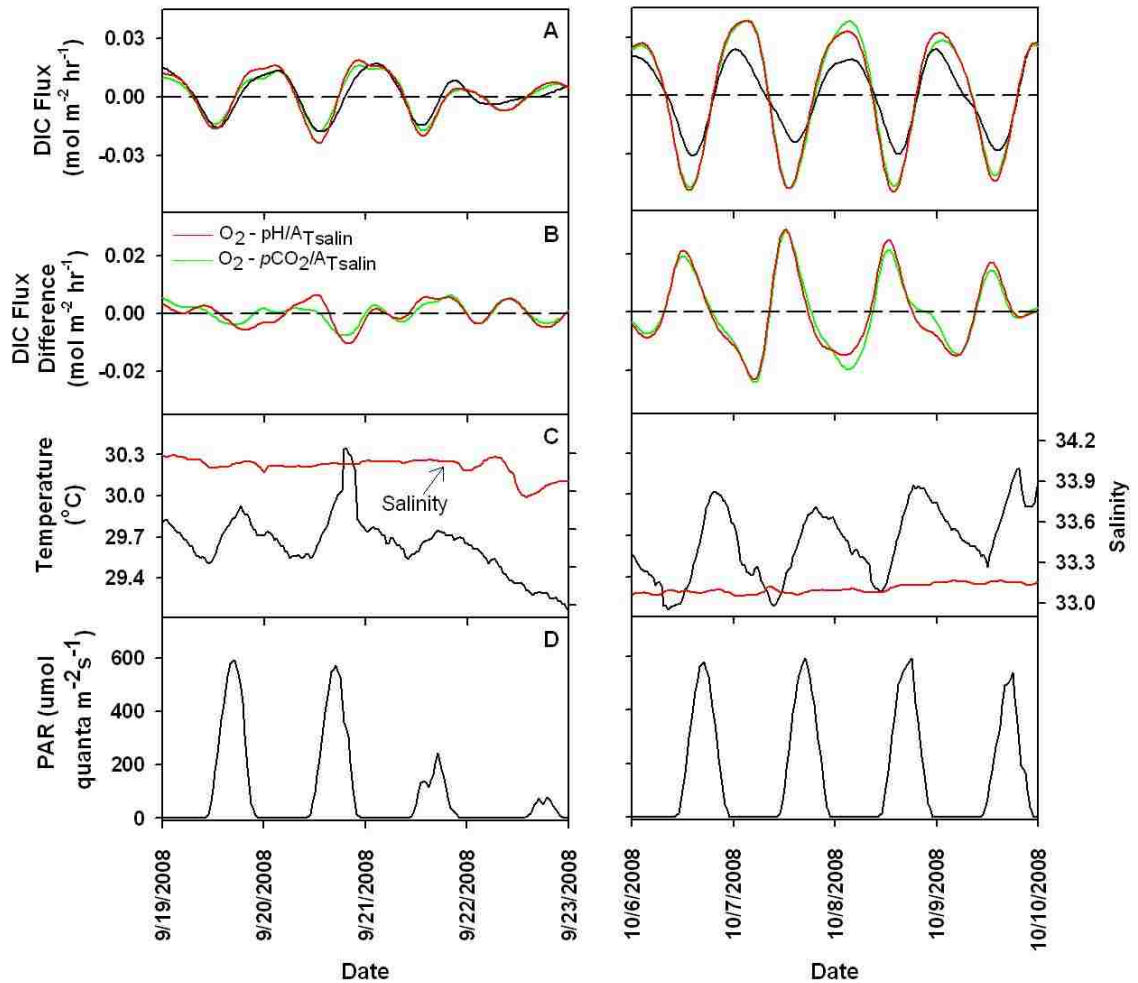
Fig. 4.5.9 (A) Blowup of the fall DIC flux for two time periods. O_2 DIC flux in black, pH/A_{Tsalin} DIC flux in red, pCO_2/A_{Tsalin} DIC flux in green. (B) DIC flux differences, O_2-pH/A_{Tsalin} in red, O_2-pCO_2/A_{Tsalin} in green. (C) Temperature in black, salinity in red. (D) PAR data.

Fig. 4.5.9 shows the correlation between the DIC flux difference and PAR for the lower (4.5.10A) and higher (4.5.10B) fall calcification scenarios. For both scenarios, the DIC flux moves from net calcification to net dissolution at night when PAR is zero. In Fig. 4.5.10A, dissolution continued to increase until light levels increased above ~300 μmol quanta m^{-2} s^{-1}. After this point, the system slowly increased to a small positive DIC flux difference throughout the remainder of the day. In Fig. 4.5.10B, dissolution started

107

to decrease as soon as PAR was above 0 μmol quanta m^{-2} s^{-1}, moving towards a higher

positive DIC flux difference as the day continued. While these differences are apparent,

more work is needed to determine what is driving these differences within a season.
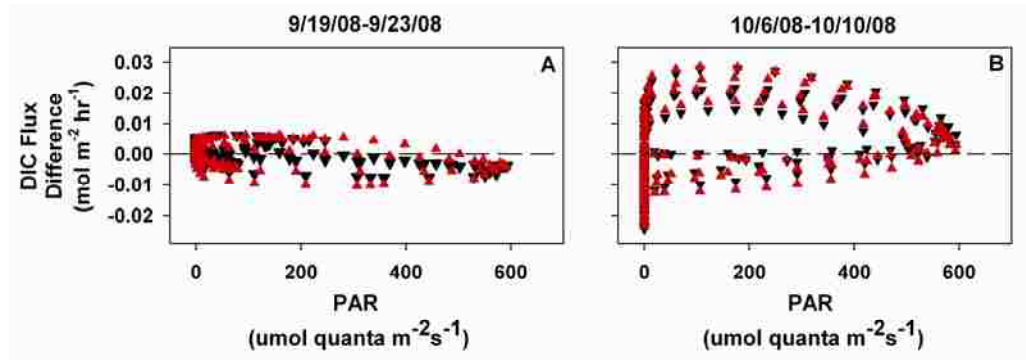
Fig. 4.5.10 (A) DIC Flux difference vs. PAR for the lower calcification period. (B) DIC
flux difference vs. PAR for the higher calcification period. O_2-pH/A_{Tsalin} in red, O_2-
pCO_2/A_{Tsalin} in black.

4.6 Conclusions

The data from Media Luna represent the highest temporal resolution

spectrophotometric pH and pCO_2 dataset for a coral reef to date, and show that the reef

experiences large variability in both pH and pCO_2 over the combined annual cycle. Diel

changes in pH (0.02-0.09 pH units) often approached the magnitude of the monthly

seasonal pH changes (0.1 pH units). These values are in the middle to low range of diel

and seasonal pH values observed previously on very shallow reefs (1-2.5 meters)

(Kayanne et al., 2005; Silverman et al., 2007; Yates and Halley, 2006). The water at

Media Luna is deeper (4-5 meters) compared to earlier studies, and the added oceanic

waters likely dilute some of the effects of production and calcification on the reef. The

reefs at La Parguera have also experienced numerous coral bleaching events since the

1980's (Winter et al., 1998), which has been shown to cause decreased coral health and coral death (Hoegh-Guldberg, 1999), leading to decreased pH variability. Half of the seasonal pH variability was driven by temperature changes. The remaining changes were due to a combination of local primary production, organic carbon export from surrounding mangroves and $CaCO_3$ production. While coral zonation at La Parguera is similar to other Caribbean reefs (Garcia et al., 1998), local factors such as mangroves and terrestrial sediment inputs can have a large impact on local dynamics. Reefs on the southern coast of Puerto Rico, east of La Parguera, have shown decreased species diversity and coral cover due to significant terrestrial sediment inputs (Acevedo et al., 1989).

The reef was a source of CO_2 to the atmosphere for only two of the three seasons studied, highlighting the importance of seasonal data in determining annual reef CO_2 fluxes. Saturation states modeled from pH and pCO_2 showed that the reef currently experiences large daily changes in saturation state, which are correlated with pH and pCO_2 diel variability. In comparison, seasonal saturation state changes were mainly affected by temperature and salinity changes on the reef. Calcification rates were below measurement limits for the winter but fall rates indicate that the reef experiences a slight net dissolution during this time. Data were not available to calculate exact summertime calcification rates, but alkalinity changes between the reef and offshore waters indicate that calcification rates may be higher during this time. These data showed that the development of in situ pH sensors has made it possible to accurately define pH variability on coral reefs. When detailed data such as these are available for more reefs systems, we will be able to more accurately determine global estimates of pH dynamics on reefs. The

SAMI-pH data can currently be used to help drive regional climate models, such as the

Caribbean saturation state model of Gledhill et al. (2008), which often do not contain

enough data for coastal and reef ecosystems to make accurate predictions in these areas.

CHAPTER 5

Summary and Future Work

5.1 Summary

The SAMI-pH was used in numerous field deployments to determine instrument performance as well as pH variability and inorganic carbon dynamics in the field. Instrument performance in the laboratory, including measurement of molar absorptivities and accuracy tests, was determined on five SAMI-pHs for use in ten different field deployments (Table 2.1.1). The average SAMI-pH accuracy was 0.0027 ± 0.0057 pH units for seawater samples and 0.0053 ± 0.0018 pH units for Tris buffer samples. Accuracy of Tris buffer samples increased to 0.0018 ± 0.0006 pH units when the Tris sample was measured at an interval of 15 minutes instead of stating a new measurement directly after the previous sample.

In the first main deployment, a SAMI-pH was deployed with a Li-COR based in situ pCO_2 sensor in Monterey Bay, CA from June-August 2007. The pH and pCO_2 data showed large weekly changes (0.32 pH units and 240 μatm, respectively) that were driven by upwelling of deeper waters to the surface. The main focus of this deployment was to determine the feasibility of using in situ data from the pH-pCO_2 pair to model the remaining inorganic carbon parameters, A_T and DIC, in addition to the calcite and aragonite saturation states. A salinity-derived A_T (A_{Tsalin}) was used as an accuracy check on the A_T modeled from pH-pCO_2 since discrete A_T and DIC samples were not collected during the deployment. 30-hour filtered A_T and DIC calculated from pH-pCO_2 matched A_{Tsalin} and DIC calculated from pH-A_{Tsalin} and pCO_2-A_{Tsalin} to within 15 μmol kg^{-1} initially. However, the pH-pCO_2 DIC and A_T drifted apart from the other calculated

values by over 150 μmol kg^{-1} throughout the 69 day deployment, potentially due to biofouling. In contrast, calculations of short-term DIC variability from 4-hour filtered pH-pCO$_2$ produced reasonable estimates of the short-term variability, based on comparisons with nitrate. The pH-pCO$_2$ pair was used to model the aragonite and calcite saturation states and values were within a mean of 0.15 ± 0.01 and 0.24 ± 0.15, respectively, compared to the pCO$_2$-A$_{Tsalin}$ and pH-A$_{Tsalin}$ values. These results showed that the pH-pCO$_2$ combination provides valuable insights into data quality and short-term A$_T$ and DIC variability as well as calcium carbonate (CaCO$_3$) saturation states, but that the reliability of long-term predictions of mean A$_T$ and DIC values from pH-pCO$_2$ requires further research.

During the second main deployment the SAMI-pH and SAMI-CO$_2$ were used to examine diel and seasonal inorganic carbon variability on Media Luna coral reef, Puerto Rico for two month periods over three seasons in 2007 and 2008. A total of ~18,500 spectrophotometric pH measurements were collected over the three deployments. pH on the reef was at a minimum of 7.89 during the fall storm season and at a maximum of 8.17 during the winter, with average monthly pH values between 7.99 and 8.10 pH units. Half of this seasonal variation was driven by temperature, with the remaining changes due to organic carbon and CaCO$_3$ production. The average diel pH range was 0.08 ± 0.03 pH units, with a seasonal diel minimum and maximum of 0.012 and 0.176 pH units, respectively. CO$_2$ gas fluxes indicated that the reef was a source of CO$_2$ to the atmosphere during the summer and fall seasons, and a sink during the winter. Annually, the reef was a source of CO$_2$, with a flux of 1.19 mol m^{-2} year^{-1}. Calcium carbonate saturation states were modeled with pH and pCO$_2$ and showed seasonal values between

2.7-5.4 for aragonite and 4.0-7.0 for calcite. Model predictions indicate that aragonite

saturation will be below 3.0 year-round if atmospheric CO_2 values increase to 500 μatm.

The pH, pCO_2 and O_2 data were used to examine calcification on the reef during the

winter and fall seasons. During the winter, calcification rates were between -0.012 and

0.010 mol m^{-2} hr^{-1}, which is within the margin of error for the instruments. During the

fall, calcification rates were between -0.023 and 0.029 mol m^{-2} hr^{-1}. Mean calcification

for the fall season showed a net $CaCO_3$ dissolution of -1.0919 mol m^{-2}. Average rates of

calcification showed that the reef was experiencing net dissolution over a 24 hour period

during the fall. This is in contrast to previous work on reefs (Kayanne et al., 2005;

Silverman et al., 2007), which generally shows net calcification during the summer and

fall, with the exception of Molokai Reef (Yates and Halley, 2006).

5.2. Future Work

With extensive field testing of the SAMI-pH complete, the instrument can now be

used in future deployments with a high confidence in the pH data. As more deployments

are carried out using both the SAMI-pH and in situ pCO_2 sensors, better evaluations of

the mean long-term accuracy of A_T and DIC modeled from the pH-pCO_2 pair will be

possible. Preliminary work by Katherine Harris in an upwelling zone off the coast of

Oregon has shown promising results for the long-term accuracy of DIC modeled using

pH and pCO_2 data. In the future, the pH SAMIs will be deployed in situ with a Tris

buffer pH standard (DelValls and Dickson, 1998). This pH standard will be run

periodically (i.e. once per day to once every several days) to help account for pH drifts

over time, such as those due to instrument fouling. Continued studies of coral reef

dynamics would ideally be carried out on a reef that is more productive than Media Luna so that A_T changes between two sites across the reef would be larger than measurement errors. Calcification on the reef could then be evaluated using both the alkalinity anomaly technique (difference in A_T over time) and the production-calcification method (differences in modeled DIC from O_2 and pH-pCO_2) as an added accuracy check. Additional reef work should include off-reef sampling locations to define the inorganic carbon dynamics of reef end-member waters.

References

Acevedo, R., Morelock, J. and Olivieri, R.A., 1989. Modification of coral reef zonation by terrigenous sediment stress. Palaios, 4: 92-100.

Barnes, D.J., 1983. Profiling coral reef productivity and calcification using pH and oxygen electrodes. Journal of Experimental Marine Biology and Ecology, 66(2): 149-61.

Bates, N.R., 2002. Seasonal variability of the effect of coral reefs on seawater CO_2 and air-sea CO_2 exchange. Limnology and Oceanography, 47(1): 43-52.

Bates, N.R., Samuels, L. and Merlivat, L., 2001. Biogeochemical and physical factors influencing seawater fCO2 and air-sea CO2 exchange on the Bermuda coral reef. Limnology and Oceanography, 46(4): 833-846.

Borges, A.V., Delille, B. and Frankingnoulle, M., 2005. Budgeting sinks and sources of CO_2 in the coastal ocean: Diversity of ecosystems counts. Geophysical Research Letters, 32: L14601.

Borges, A.V. et al., 2003. Atmospheric CO_2 flux from mangrove surrounding waters. Geophysical Research Letters, 30(11): 1158.

Bouillon, S., Dehairs, F., Velimirov, B., Abril, G. and Borges, A.V., 2007. Dynamics of organic and inorganic carbon across contiguous mangrove and seagrass systems (Gazi Bay, Kenya). Journal of Geophysical Research, 112: G02018.

Brezinski, D.P., 1983. Kinetic, Static, and Stirring errors of Liquid junction reference electrodes. Analyst, 108: 425-442.

Byrne, R.H. and Breland, J.A., 1989. High precision multiwavelength pH determinations in seawater using cresol red. Deep-Sea Res., 36(5): 803-810.

Byrne, R.H., S. McElligott, R.A. Feely, F.J. Millero, 1999. The role of pH_T measurements in marine CO_2-system characterizations. Deep-Sea Research I, 46(11): 1985-1997.

Caldeira, K. and Wickett, M.E., 2003. Anthropogenic carbon and ocean pH. Nature (London, United Kingdom), 425(6956): 365.

Cao, L., Caldeira, K. and Jain, A.K., 2007. Effects of carbon dioxide and climate change on ocean acidification and carbonate mineral saturation. Geophysical Research Letters, 34(5): L05607/1-L05607/5.

Chen, C.-T.A. and Borges, A.V., 2009. Reconciling opposing views on carbon cycling in the coastal ocean: Continental shelves as sinks and near-shore ecosystems as sources of atmospheric CO_2. Deep-Sea Research II, 56: 578-590.

Cintrón, G., Lugo, A.E., Pool, D.J. and Morris, G., 1978. Mangroves of arid environments in Puerto Rico and adjacent islands. Biotropica, 10(2): 110-121.

Clayton, T.D. and Byrne, R.H., 1993. Spectrophotometric seawater pH measurements: total hydrogen ion concentration scale calibration of m-cresol purple and at-sea results. Deep-Sea Research, 40(10): 2,115-2,129.

Clayton, T.D. et al., 1995. The role of pH measurements in modern oceanic CO_2-system characterizations: precision and thermodynamic consistency. Deep-Sea Research, Part II: Topical Studies in Oceanography, 42(2-3): 411-29.

Corredor, J.E. and Morell, J.M., 2001. Seasonal variation of physical and biogeochemical features in eastern Caribbean surface water. Journal of Geophysical Research, [Oceans], 106(C3): 4517-4525.

Cullison, S.E. et al., in preparation. Applications of in situ pH measurements for inorganic carbon calculations. Marine Chemistry.

Davison, W. and Woof, C., 1985. Performance tests for the measurements of pH with glass electrodes in low ionic strength solutions including natural waters. Analytical Chemistry, 57: 2567-2570.

DeGrandpre, M.D., Baehr, M.M. and Hammar, T.R., 1999. Calibration-Free Optical Chemical Sensors. Analytical Chemistry, 71(6): 1152-1159.

DeGrandpre, M.D., Hammar, T.R., Smith, S.P. and Sayles, F.L., 1995. In situ measurements of seawater CO_2. Limnology and Oceanography, 40: 969-975.

DeGrandpre, M.D., Olbu, G.J., Beatty, C.M. and T.R. Hammar, 2002. Air-sea CO_2 fluxes on the U.S. Middle Atlantic Bight. Deep-Sea Res. II, 49: 4,355-4,367.

DeGrandpre, M.D., Wanninkhof, R., McGillis, W.R. and Strutton, P.G., 2004. A Lagrangian study of surface pCO_2 dynamics in the eastern equatorial Pacific Ocean. Journal of Geophysical Research, 109: C08S07.

DelValls, T.A. and Dickson, A.G., 1998. The pH of buffers based on 2-amino-hydroxymethyl-1,3-propanediol ('tris') in synthetic sea water. Deep-Sea Research I, 45: 1541-1554.

Dickson, A.G., 1990. Standard potential of the reaction: silver chloride + hydrogen [AgCl(s) + 1/2H2(g) = Ag(s) + HCl(aq)] and the standard acidity constant of the hydrogen sulfate ion HSO_4^- in synthetic sea water from 273.15 to 318.15 K. Journal of Chemical Thermodynamics, 22(2): 113-27.

Dickson, A.G., 1993. The measurement of seawater pH. Marine Chemistry, 44: 131-142.

Dickson, A.G., Afghan, J.D. and Anderson, G.C., 2003. Reference materials for oceanic CO_2 analysis: a method for the certification of total alkalinity. Marine Chemistry, 80(2-3): 185-197.

Dickson, A.G. and Millero, F.J., 1987. A comparison of the equilibrium constants for the dissociation of carbonic acid in seawater media. Deep-Sea Research, Part A: Oceanographic Research Papers, 34(10A): 1733-43.

Dickson, A.G. and Riley, J.P., 1978. The effect of analytical error on the evaluation of the components of the aquatic carbon-dioxide system. Marine Chemistry, 6: 77-85.

Dickson, A.G., Sabine, C.L. and Christian, J.R., 2007. Guide to best practices for ocean CO_2 measurements. PICES Special Publication, 3, 191 pp.

Emerson, S. et al., in preparation. Production rates of $CaCO_3$ and organic carbon in ocean surface waters from in situ measurements of pCO_2 and pH. Global Biogeochemical Cycles.

Fabry, V.J., Seibel, B.A., Feely, R.A. and Orr, J.C., 2008. Impacts of ocean acidification on marine fauna and ecosystem processes. ICES Journal of Marine Science, 65(3): 414-432.

Fagan, K.E. and Mackenzie, F.T., 2007. Air-sea exchange in a subtropical estuarine-coral reef system, Kaneohe Bay, Oahu, Hawaii. Marine Chemistry, 106: 174-191.

Feely, R.A., Byrne, R.H., Betzer, P.R., Gendron, J.F. and Acker, J.G., 1984. Factors influencing the degree of saturation of the surface and intermediate waters of the North Pacific Ocean with respect to Aragonite. Journal of Geophysical Research, 89(C6): 10631-10640.

Feely, R.A., Sabine, C.L., Hernandez-Ayon, J.M., Ianson, D. and Hales, B., 2008. Evidence for upwelling of corrosive "acidified" water onto the continental shelf. Science, 320(5882): 1490-1492.

Feely, R.A. et al., 2004. Impact of Anthropogenic CO_2 on the $CaCO_3$ System in the Oceans. Science, 305(5682): 362-367.

Feely, R.A. et al., 2006. Decadal variability of the air-sea CO_2 fluxes in the equatorial Pacific Ocean. Journal of Geophysical Research, 111: C08S90.

French, C.R., Carr, J.J., Dougherty, E.M., Eidson, L.A.K., Reynolds, J.C. and M.D. DeGrandpre, 2002. Spectrophotometric measurements of freshwater pH. Analytica Chimica Acta, 453: 13-20.

Friederich, G.E., Brewer, P.G., Herlien, R. and Chavez, F.P., 1995. Measurement of sea surface partial pressure of CO_2 from a moored buoy. Deep-Sea Research I, 42(7): 1175-86.

Friederich, G.E., Walz, P.M., Burczynski, M.G. and Chavez, F.P., 2002. Inorganic carbon in the central California upwelling system during the 1997-1999 El Nino-La Nina event. Progress in Oceanography, 54: 185-203.

Fuhrmann, R. and Zirino, A., 1988. High-resolution determination of the pH of seawater with a flow-through system. Deep-Sea Research, 35(2): 197-208.

Garcia, J.R., Schmitt, C., Herberer, C. and Winter, A., 1998. La Parguera, Puerto Rico, USA In: Kjerfve B. (ed) CARICOMP - Caribbean coral reef, seagrass and mangrove sites. Coastal region and small island papers (3), UNESCO, Paris, p 187-193, available at www.unesco.org/csi/pub/papers/papers3.htm.

Gledhill, D.K., Wanninkhof, R., Millero, F.J. and Eakin, M., 2008. Ocean acidification of the Greater Caribbean Region 1996-2006. Journal of Geophysical Research, [Oceans], 113(C10): C10031/1-C10031/11.

Graham, W.M. and Largier, J.L., 1997. Upwelling shadows as nearshore retention sites: the example of northern Monterey Bay. Continental Shelf Research, 17(5): 509-532.

Hoegh-Guldberg, O., 1999. Climate change, coral bleaching and the future of the world's coral reefs. Marine and Freshwater Research, 50: 839-866.

Hood, E.M., Merlivat, L. and Johannessen, T., 1999. Variations of $f CO_2$ and air-sea flux of CO_2 in the Greenland Sea gyre using high-frequency time series data from CARIOCA drift buoys. Journal of Geophysical Research, 104: 20,571-20,583.

Johnson, K.S., 2010. Simultaneous measurements of nitrate, oxygen, and carbon dioxide on oceanographic moorings: Observing the Redfield Ratio in real-time. Limnology and Oceanography, 55(2): 615-627.

Johnson, K.S. and Coletti, L.J., 2002. In situ ultraviolet spectrophotometry for high resolution and long-term monitoring of nitrate, bromide and bisulfide in the ocean. Deep-Sea Research I, 49(7): 1291-1305.

Jokiel, P.L. et al., 2008. Ocean acidification and calcifying reef organisms: a mesocosm investigation. Coral Reefs, 27: 473-483.

Kawahata, H., Yukino, I. and Suzuki, A., 2000. Terrestrial influences of the Shiraho fringing reef, Ishigaki Island, Japan: High carbon input relative to phosphate. Coral Reefs, 19: 172-178.

Kayanne, H. et al., 2005. Seasonal and bleaching-induced changes in coral reef metabolism and CO_2 flux. Global Biogeochemical Cycles, 19(3): GB3015/1-GB3015/11, 1 plate.

Key, R.M. et al., 2004. A global ocean carbon climatology: Results from Global Data Analysis Project (GLODAP). Global Biogeochemical Cycles, 18: GB4031.

Kleypas, J.A., McManus, J.W. and Menez, L.A.B., 1999a. Environmental limits to coral reef development: Where do we draw the line? American Zoologist, 39: 146-159.

Kleypas, J.A., R.R. Buddemeier, D. Archer, J.P.G., C. Landgon and Opdyke, B.N., 1999b. Geochemical consequences of increased atmospheric CO_2 on corals and coral reefs. Science, 284: 118-120.

Koné, Y.J.-M. and Borges, A.V., 2008. Dissolved inorganic carbon dynamics in the waters surrounding forested mangroves of the Ca Mau Province (Vietnam). Estuarine, Coastal and Shelf Science, 77: 406-421.

Kraines, S. et al., 1997. Carbonate dynamics of the coral reef system at Bora Bay, Miyako Island. Marine Ecology: Progress Series, 156: 1-16.

Kuss, J., Roeder, W., Wlost, K.P. and DeGrandpre, M.D., 2006. Time-series of surface water CO_2 and oxygen measurements on a platform in the central Arkona Sea (Baltic Sea): Seasonality of uptake and release. Marine Chemistry, 101(3-4): 220-232.

Langdon, C. and Atkinson, M.J., 2005. Effect of elevated pCO$_2$ on photosynthesis and calcification of corals and interactions with seasonal change in temperature/irradiance and nutrient enrichment. Journal of Geophysical Research, [Oceans], 110(C9): C09S07/1-C09S07/16.

Langdon, C. et al., 2003. Effect of elevated CO_2 on the community metabolism of an experimental coral reef. Global Biogeochemical Cycles, 17(1): 11/1-11/14.

Langdon, C. et al., 2000. Effect of calcium carbonate saturation state on the calcification rate of an experimental coral reef. Global Biogeochemical Cycles, 14(2): 639-654.

Leclercq, N., Gattuso, J.-P. and Jaubert, J., 2000. CO_2 partial pressure controls the calcification of a coral community. Global Change Biology, 6: 329-334.

Leclercq, N., Gattuso, J.-P. and Jaubert, J., 2002. Primary production, respiration, and calcification of a coral reef mesocosm under increased CO_2 partial pressure. Limnology and Oceanography, 47(2): 558-564.

Lee, K., Millero, F.J., Byrne, R.H., Feely, R.A. and Wanninkhof, R., 2000. The recommended dissociation constants for carbonic acid in seawater. Geophysical Research Letters, 27(2): 229-232.

Lee, K. et al., 2006. Global relationship of total alkalinity and temperature in surface waters of the world's oceans. Geophysical Research Letters, 33(19): L19605/1-L19605/5.

Liu, X., Wang, Z.A., Byrne, R.H., Kaltenbacher, E.A. and Bernstein, R.E., 2006. Spectrophotometric measurements of pH in-situ: Laboratory and field evaluations of instrumental performance. Environmental Science and Technology, 40: 5036-5044.

Mackey, D.J., Butler, E.C.V., Nichols, P.D. and Higgins, H.W., 1989. Continuous shipboard and *in situ* measurements of pH and fluorescence in seawater. Mar. Chem., 28: 41-60.

Martz, T.R., Carr, J.J., French, C.R. and DeGrandpre, M.D., 2003. A submersible autonomous sensor for spectrophotometric pH measurements of natural waters. Analytical Chemistry, 75: 1844-1850.

Martz, T.R., Dickson, A.G. and DeGrandpre, M.D., 2006. Tracer Monitored Titrations: Measurement of Total Alkalinity. Analytical Chemistry, 78(6): 1817-1826.

McElligott, S. et al., 1998. Discrete water column measurements of CO_2 fugacity and pH_T in seawater: A comparison of direct measurements and thermodynamic calculations. Marine Chemistry, 60: 63-73.

McNeil, B.I. and Matear, R.J., 2008. Southern Ocean acidification: a tipping point at 450-ppm atmospheric CO2. Proceedings of the National Academy of Sciences of the United States of America, 105(48): 18860-18864.

Meehl, G.A. et al., 2007. Global climate projections. Climate change 2007: The physical science basis. Contribution of working group I to the fourth assessment report of the intergovernmental panel on climate change.

Mehrbach, C., Culberson, C.H., Hawley, J.E. and Pythowicz, R.M., 1973. Measurement of the apparent dissociation constants of carbonic acid in seawater at atmospheric pressure. Limnology and Oceanography, 18: 897-907.

Millero, F.J., 1995. Thermodynamics of the carbon dioxide system in the oceans. Geochimica et Cosmochimica Acta, 59(4): 661-77.

Millero, F.J., Lee, K., and M. Roche, 1998. Distribution of alkalinity in the surface waters of the major oceans. Mar. Chem., 60: 111-130.

Nakano, Y., Kimoto, H., Watanabe, S., Harada, K. and Watanabe, Y.W., 2006. Simultaneous vertical measurements of in situ pH and CO_2 in the sea using spectrophotometric profilers. Journal of Oceanography, 62: 71-81.

Ohde, S., 1995. Calcium carbonate production and carbon dioxide flux on a coral reef, Okinawa. Bigeochemical Processes and Ocean Flux in the Western Pacific. Terra Scientific Publishing Company, Tokyo, 93-98 pp.

Olsen, A., Triñanes, J.A. and Wanninkhof, R., 2004. Sea-air flux of CO_2 in the Caribbean Sea estimated using in situ and remote sensing data. Remote Sensing of Environment, 89: 309-325.

Omar, A.M. and Olsen, A., 2006. Reconstructing the time history of air-sea CO_2 disequilibrium and its rate of change int he eastern subpolar North Atlantic, 1972-1989. Geophysical Research Letters, 33: L04602.

Orr, J.C. et al., 2005. Anthropogenic ocean acidification over the twenty-first century and its impact on calcifying organisms. Nature (London, U. K.) FIELD Full Journal Title:Nature (London, United Kingdom), 437(7059): 681-686.

Pelejero, C. et al., 2005. Preindustrial to modern interdecadal variability in coral reef pH. Science (New York, N.Y.), 309(5744): 2204-7.

Pierrot, D., Lewis, E. and Wallace, D.W.R., 2006. MS Excel program developed for CO_2 system calculations. ORLN/CDIAC-105, Carbon Dioxide Information Analysis Center, Oak Ridge National Laboratory, U.S. Department of Energy, Oak Ridge, Tennessee.

Raven, J. et al., 2005. Ocean acidification due to increasing atmospheric carbon dioxide. The Royal Society, London.

Riebesell, U. et al., 2000. Reduced calcification of marine plankton in response to increased CO_2. Nature, 407: 364-367.

Sabine, C.L. et al., 2004. The Oceanic Sink for Anthropogenic CO2. Science (Washington, DC, United States), 305(5682): 367-371.

Santana-Casiano, J.M., Gonzalez-Davila, M., Rueda, M.-J., Llinas, O. and Gonzalez-Davila, E.-F., 2007. The interannual variability of oceanic CO2 parameters in the northeast Atlantic subtropical gyre at the ESTOC site. Global Biogeochemical Cycles, 21(1): GB1015/1-GB1015/16.

Sayles, F.L. and Eck, C., 2009. An autonomous instrument for time series analysis of TCO_2 from oceanographic moorings. Deep-Sea Research I, 56(9): 1590-1603.

Seidel, M., 2006. Dissertation: A sensor for in situ spectrophotometric measurements of seawater pH, The University of Montana, Missoula, 154 pp.

Seidel, M.P., DeGrandpre, M.D. and Dickson, A.G., 2008. A sensor for in situ indicator-based measurements of seawater pH. Marine Chemistry, 109(1-2): 18-28.

Silverman, J., Lazar, B. and Erez, J., 2007. Effect of aragonite saturation, temperature, and nutrients on the community calcification rate of a coral reef. Journal of Geophysical Research, [Oceans], 112(C5): C05004/1-C05004/14.

Skogsberg, T., 1936. Hydrography of Monterey Bay, California. Thermal Conditions, 1929-1933. Transactions of the American Philosophical Society, 29: 1-152.

Skogsberg, T. and Phelps, A., 1946. Hydrography of Monterey Bay, California. Thermal Conditions, 1929-1933, Part II. Proceedings of the American Philosophical Society, 90: 350-386.

Smith, J., W.H. and Hood, D.W., 1964. pH measurement in the ocean: a sea water secondary buffer system. In: Y. Miyake, T. Koyama (Eds), Recent researches in the fileds of hydrosphere, atmosphere and nuclear geochemistry. Published by Editorial Committee for Sugawara Volume, distributed by Maruzen Company, Ltd, Tokoyo, Japan: 185-202.

Solomon, S., Plattner, G.-K., Knutti, R. and Friedlingstein, P., 2009. Irreversible climate change due to carbon dioxide emissions. Proceedings of the National Academy of Sciences of the United States of America, 106(6): 1704-1709.

Takahashi, T. et al., 2009. Climatological mean and decadal change in surface ocean pCO_2, and net sea-air CO_2 flux over the global oceans. Deep-Sea Research, Part II: Topical Studies in Oceanography, 56(8-10): 554-577.

Wanninkhof, R., 1992. Relationship between wind speed and gas exchange over the ocean. Journal of Geophysical Research, 97: 7373-7382.

Wanninkhof, R. and Thoning, K., 1993. Measurement of fugacity of CO_2 in surface water using continuous and discrete sampling methods. Marine Chemistry, 44: 189-204.

Wei, G., McCulloch, M.T., Mortimer, G., Deng, W. and Xie, L., 2009. Evidence for ocean acidification in the Great Barrier Reef of Australia. Geochimica et Cosmochimica Acta, 73(8): 2332-2346.

Winter, A., Appeldoorn, R.S., Bruckner, A., Jr., E.H.W. and Geonaga, C., 1998. Sea surface temperature and coral reef bleaching off La Parguera, Puerto Rico (northeastern Caribbean Sea). Coral Reefs, 17: 377-382.

Wootton, J.T., Pfister, C.A. and Forester, J.D., 2008. Dynamic patterns and ecological impacts of declining ocean pH in a high-resolution multi-year dataset. Proceedings of the National Academy of Sciences of the United States of America, 105(48): 18848-18853.

Yates, K.K. and Halley, R.B., 2006. CO_3^{2-} concentration and pCO_2 thresholds for calcification and dissolution on the Molokai reef flat, Hawaii. Biogeosciences, 3(3): 357-369.

e-values at the average run temperature

Deployment	SAMI	Trial #	Date	Pathlength (cm)	Avg run temp (oC)	Ea434	Ea578	Eb434	Eb578	e1	e2	e3
PR #1	42	2	6/4/2007	0.75	21.5	17850	186	2278	38228	0.0104	2.1416	0.1276
PR #1	47	1	5/19/2007	1.0	21.9	17761	99	2558	39503	0.0056	2.2242	0.1440
PR #1	47	2	6/4/2007	1.0	21.9	18136	74	2412	39887	0.0041	2.1994	0.1330
PR #2	47	3	11/12/2007	1.0	23.1	17962	135	2702	39817	0.0075	2.2167	0.1504
PR #2	47	5	11/28/2007	1.0	22.8	13764	94	1937	31107	0.0069	2.2601	0.1407
Molasses #1	47	6	5/8/2008	1.0	23.2	18206	117	2532	40666	0.0064	2.2337	0.1391
Molasses #1	47	7	5/14/2008	1.0	18.1	18276	117	2517	41064	0.0064	2.2469	0.1377
Molasses #1	47	8	8/12/2008	1.0	22.9	18043	120	2532	40540	0.0067	2.2469	0.1403
Molasses #1	47	9	8/24/2008	1.0	23.5	17924	119	2490	39749	0.0067	2.2177	0.1389
Molasses #1	47	10	8/28/2008	1.0	24.2	18141	120	2565	40888	0.0066	2.2539	0.1414
Molasses #2	47	11	2/2/2009	1.0	22.9	18535	114	2614	41288	0.0062	2.2276	0.1411
MBARI	13	1	3/7/2007	0.75	20.2	18808	95	2508	41987	0.0051	2.2324	0.1334
MBARI	13	2	3/10/2007	0.75	20.1	18867	89	2556	42794	0.0047	2.2682	0.1355
S. Ocean	13	3	12/19/2007	0.75	22.2	14708	99	1995	32554	0.0067	2.2133	0.1356
Stn Papa #2	13	4	5/8/2008	1.0	23.2	18474	115	2579	40588	0.0062	2.1971	0.1396
Stn Papa #2	13	5	5/14/2008	1.0	17.6	18362	122	2517	40975	0.0067	2.2315	0.1371
PR #2	68	1	11/20/2007	0.75	23.3	18917	74	2468	42252	0.0039	2.2336	0.1305
PR #2	68	2	11/27/2007	0.75	23.1	18782	99	2468	42252	0.0053	2.2496	0.1314
PR #2	68	3	11/27/2007	0.75	22.9	18782	99	2394	41867	0.0053	2.2291	0.1275
PR #2	68	4	12/10/2007	0.75	23.0	18922	102	2429	42151	0.0054	2.2276	0.1284
PR#3	68	5	5/8/2008	1.0	22.9	18299	94	2332	40600	0.0051	2.2186	0.1275
PR#3	68	6	8/24/2008	1.0	24.0	18366	99	2365	40479	0.0054	2.2040	0.1288
Stn Papa #1	59	1	4/6/2007	0.75	20.0	14116	70	1844	31531	0.0050	2.2337	0.1307
Stn Papa #1	59	2	4/6/2007	0.75	20.0	18815	96	2459	41767	0.0051	2.2199	0.1307
PR #3	59	3	8/12/2008	1.00	22.6	17975	114	2340	40129	0.0063	2.2325	0.1302
Stn Papa #3	59	4	1/21/2009	1.00	22.8	18485	132	2435	40877	0.0071	2.2114	0.1317

Appendix A – e-values

e-values temperature corrected to 25 °C

Deployment	SAMI	Trial #	Date	Pathlength (cm)	Avg run temp (oC)	Ea434	Ea578	Eb434	Eb578	e1	e2	e3
PR #1	42	2	6/4/2007	0.75	21.5	17928	184	2256	38577	0.0102	2.1517	0.1258
PR #1	47	1	5/19/2007	1.0	21.9	17830	97	2538	39812	0.0054	2.2329	0.1424
PR #1	47	2	6/4/2007	1.0	21.9	18205	72	2392	40196	0.0040	2.2080	0.1314
PR #2	47	3	11/12/2007	1.0	23.1	18004	134	2690	40006	0.0074	2.2220	0.1494
PR #2	47	5	11/28/2007	1.0	22.8	13813	93	1923	31326	0.0067	2.2679	0.1392
Molasses #1	47	6	5/8/2008	1.0	23.2	18246	116	2520	40845	0.0064	2.2386	0.1381
Molasses #1	47	7	5/14/2008	1.0	18.1	18430	113	2473	41751	0.0061	2.2654	0.1342
Molasses #1	47	8	8/12/2008	1.0	22.9	18090	119	2519	40749	0.0066	2.2526	0.1392
Molasses #1	47	9	8/24/2008	1.0	23.5	17957	118	2481	39898	0.0066	2.2219	0.1382
Molasses #1	47	10	8/28/2008	1.0	24.2	18159	120	2560	40968	0.0066	2.2561	0.1410
Molasses #2	47	11	2/2/2009	1.0	22.9	18582	113	2601	41497	0.0061	2.2332	0.1400
MBARI	13	1	3/7/2007	0.75	20.2	18915	92	2478	42465	0.0049	2.2451	0.1310
MBARI	13	2	3/10/2007	0.75	20.1	18977	87	2525	43283	0.0046	2.2808	0.1331
S. Ocean	13	3	12/19/2007	0.75	22.2	14770	97	1977	32833	0.0066	2.2229	0.1339
Stn Papa #2	13	4	5/8/2008	1.0	23.2	18514	114	2568	40767	0.0062	2.2020	0.1387
Stn Papa #2	13	5	5/14/2008	1.0	17.6	18527	118	2470	41712	0.0064	2.2514	0.1333
PR #2	68	1	11/20/2007	0.75	23.3	18954	73	2458	42421	0.0039	2.2381	0.1297
PR #2	68	2	11/27/2007	0.75	23.1	18824	98	2456	42441	0.0052	2.2546	0.1305
PR #2	68	3	11/27/2007	0.75	22.9	18829	98	2381	42076	0.0052	2.2346	0.1265
PR #2	68	4	12/10/2007	0.75	23.0	18967	101	2417	42350	0.0053	2.2329	0.1274
PR#3	68	5	5/8/2008	1.0	22.9	18346	93	2319	40809	0.0051	2.2244	0.1264
PR#3	68	6	8/24/2008	1.0	24.0	18389	99	2359	40579	0.0054	2.2067	0.1283
Stn Papa #1	59	1	4/6/2007	0.75	20.0	14228	67	1813	32030	0.0047	2.2512	0.1274
Stn Papa #1	59	2	4/6/2007	0.75	20.0	18926	93	2427	42265	0.0049	2.2331	0.1282
PR #3	59	3	8/12/2008	1.00	22.6	18028	113	2325	40368	0.0062	2.2391	0.1290
Stn Papa #3	59	4	1/21/2009	1.00	22.8	18534	131	2421	41096	0.0070	2.2174	0.1306

Appendix A – e-values

					pH Accuracy - Seawater Samples					
Deployment	Measurement Date	SAMI #	Trial #	Cary Temp	Cary pH (adjusted to 20 oC)	SAMI temp	SAMI pH (adjusted to 20 oC)	Difference (Cary-SAMI)	AVG	STDEV
Monterey Bay	3/8/2007	13	1	20.01	7.9052	20.09	7.9036	0.0015		
			2	19.95	7.9118	20.09	7.9040	0.0078		
			3	19.96	7.9078	20.08	7.9033	0.0045		
			4	20.01	7.9053	20.08	7.9039	0.0014		
			5	19.97	7.9156	20.07	7.9058	0.0098	**0.0050**	**0.0037**
PR #2	12/11/2007	68	1	20.35	8.1352	20.39	8.1390	-0.0039		
			2	20.38	8.1334	20.39	8.1386	-0.0052		
			3	20.42	8.1370	20.44	8.1371	-0.0002		
			4	20.42	8.1318	20.41	8.1381	-0.0063		
			5	20.46	8.1314	20.41	8.1378	-0.0064		
			6	20.44	8.1316	20.41	8.1366	-0.0049	**-0.0045**	**0.0023**
PR #2	12/11/2007	47	1	20.35	8.1352	20.39	8.1392	-0.0041		
			2	20.38	8.1334	20.37	8.1398	-0.0064		
			3	20.42	8.1370	20.36	8.1392	-0.0022		
			4	20.42	8.1318	20.37	8.1387	-0.0069		
			5	20.46	8.1314	20.37	8.1395	-0.0081		
			6	20.44	8.1316	20.37	8.1393	-0.0077	**-0.0059**	**0.0023**
S. Ocean Gas Ex	12/20/2007	13	1	20.41	8.1512	20.82	8.1498	0.0014		
			2	20.46	8.1520	20.86	8.1476	0.0044		
			3	20.52	8.1513	20.84	8.1493	0.0020		
			4	20.48	8.1546	20.5	8.1450	0.0096		
			5	20.46	8.1555	20.48	8.1453	0.0102		
			6	20.52	8.1525	20.47	8.1443	0.0082	**0.0060**	**0.0039**

Appendix B – pH Accuracy

					pH Accuracy - Seawater Samples					
Deployment	Measurement Date	SAMI #	Trial #	Cary Temp	Cary pH (ajdusted to 20 oC)	SAMI temp	SAMI pH (ajdusted to 20 oC)	Difference (Cary-SAMI)	AVG	STDEV
Stn Papa #2	5/12/2008	13	1	19.77	7.9367	19.91	7.9384	-0.0017		
			2	19.77	7.9349	19.93	7.9383	-0.0034		
(Trial #1)			3	19.79	7.9408	19.92	7.9381	0.0027		
			4	19.81	7.9412	19.91	7.9373	0.0040		
			5	19.90	7.9437	19.91	7.9372	0.0065		
			6	19.90	7.9427	19.93	7.9368	0.0059		
			7	19.94	7.9426	19.91	7.9373	0.0053	**0.0028**	**0.0039**
Stn Papa #2	5/14/2008	13	1	20.10	7.9690	19.98	7.9639	0.0051		
			2	20.12	7.9678	19.96	7.9637	0.0041		
(Trial #2)			3	20.08	7.9683	19.98	7.9635	0.0048		
			4	20.06	7.9675	19.98	7.9636	0.0039		
			5	20.05	7.9666	19.98	7.9637	0.0028	**0.0042**	**0.0009**
PR #3	5/12/2008	68	1	19.77	7.9367	19.82	7.9331	0.0036		
			2	19.77	7.9349	19.83	7.9329	0.0020		
			3	19.79	7.9408	19.83	7.9328	0.0080		
			4	19.81	7.9412	19.83	7.9333	0.0079		
			5	19.90	7.9427	19.83	7.9339	0.0088		
			6	19.94	7.9426	19.83	7.9333	0.0093	**0.0066**	**0.0030**
PR #3	8/15/2008	59	1	20.42	8.1231	19.82	8.1172	0.0060		
			2	20.43	8.1198	19.78	8.1152	0.0046		
			3	20.40	8.1201	19.89	8.1153	0.0048	**0.0051**	**0.0007**
Molasses #1	8/15/2008	47	1	20.42	8.1231	20.11	8.1101	0.0130		
			2	20.43	8.1198	20.11	8.1089	0.0109		
			3	20.40	8.1201	20.10	8.1103	0.0097	**0.0112**	**0.0016**

Appendix B – pH Accuracy   125

| | | | | pH Accuracy - Tris Buffer Samples | | | | | |

Deployment	Measurement Date	SAMI #	Trial #	Tris pH (calc at SAMI temp	SAMI temp	SAMI pH	Difference (Tris-SAMI)	AVG	STDEV
PR #3	8/15/2008	59	1	8.2503	19.98	8.2455	0.0048		
Batch 1, Bottle 37			2	8.2493	20.01	8.2439	0.0054		
			3	8.2497	20.00	8.2432	0.0065		
			4	8.2497	20.00	8.2442	0.0055		
			5	8.2497	20.00	8.2455	0.0042		
			6	8.2497	20.00	8.2455	0.0042	**0.0051**	**0.0009**
PR #3	8/15/2008	59	1	8.2503	19.98	8.2451	0.0052		
Batch 1, Bottle 21			2	8.2506	19.97	8.2453	0.0053		
			3	8.2506	19.97	8.2454	0.0052		
			4	8.2509	19.96	8.2448	0.0061		
			5	8.2506	19.97	8.2434	0.0072	**0.0058**	**0.0009**
PR #3	8/19/2008	68	1	8.2484	20.04	8.2420	0.0064		
Batch 1, Bottle 32			2	8.2481	20.05	8.2421	0.0060		
			3	8.2487	20.03	8.2424	0.0063		
			4	8.2481	20.05	8.2427	0.0053		
			5	8.2484	20.04	8.2415	0.0069	**0.0062**	**0.0006**
PR #3	8/15/2008	Cary	1	8.2375	20.38	8.2456	-0.0081		
Batch 1, Bottle 37			2	8.2359	20.43	8.2448	-0.0089		
			3	8.2378	20.37	8.2462	-0.0083	**-0.0085**	**0.0004**
PR #3	8/15/2008	Cary	1	8.2385	20.35	8.2482	-0.0097		
Batch 1, Bottle 21			2	8.2372	20.39	8.2450	-0.0078		
			3	8.2378	20.37	8.2477	-0.0099	**-0.0091**	**0.0011**
PR #3	8/19/2008	Cary	1	8.2407	20.28	8.2515	-0.0108		
Batch 1, Bottle 32			2	8.2484	20.04	8.2582	-0.0098		
			3	8.2481	20.05	8.2577	-0.0096	**-0.0100**	**0.0006**

Appendix B – pH Accuracy

				pH Accuracy - Tris Buffer Samples					
Deployment	Measurement Date	SAMI #	Trial #	Tris pH (calc at SAMI temp	SAMI temp	SAMI pH	Difference (Tris-SAMI)	AVG	STDEV
Stn Papa #3	1/30/2009	59	1	8.1169	24.19	8.1168	0.0001		
			2	8.1047	24.58	8.0987	0.0059		
			3	8.1019	24.67	8.0949	0.0069		
			4	8.1000	24.73	8.0945	0.0055		
			5	8.0990	24.76	8.0922	0.0068		
			6	8.0981	24.79	8.0912	0.0069		
			7	8.0978	24.80	8.0901	0.0077		
			8	8.0975	24.81	8.0895	0.0080	**0.0060**	**0.0025**
Molasses #2	2/5/2009	47	1	8.2500	19.99	8.2477	0.0023		
Batch 1, Bottle 20			2	8.2503	19.98	8.2501	0.0002		
			3	8.2503	19.98	8.2496	0.0007		
			4	8.2503	19.98	8.2495	0.0008		
			5	8.2500	19.99	8.2489	0.0011		
-ran on a 60 minute			6	8.2503	19.98	8.2501	0.0002		
interval rather than			7	8.2506	19.97	8.2503	0.0004		
triggering SAMI			8	8.2503	19.98	8.2483	0.0020		
			9	8.2503	19.98	8.2486	0.0017		
			10	8.2503	19.98	8.2490	0.0013		
			11	8.2500	19.99	8.2491	0.0009		
			12	8.2503	19.98	8.2482	0.0021		
			13	8.2503	19.98	8.2487	0.0016		
			14	8.2503	19.98	8.2486	0.0017	**0.0012**	**0.0007**

Appendix B – pH Accuracy

				pH Accuracy - Tris Buffer Samples					
Deployment	Measurement Date	SAMI #	Trial #	Tris pH (calc at SAMI temp	SAMI temp	SAMI pH	Difference (Tris-SAMI)	AVG	STDEV
Molasses #2	2/5/2009	47	1	8.2497	20.00	8.2468	0.0029		
Batch 1, Bottle 20			2	8.2497	20.00	8.2482	0.0014		
			3	8.2500	19.99	8.2475	0.0025		
-ran on a 15 minute			4	8.2500	19.99	8.2488	0.0012		
interval rather than			5	8.2500	19.99	8.2483	0.0017		
triggering SAMI			6	8.2500	19.99	8.2487	0.0013		
			7	8.2500	19.99	8.2482	0.0018		
			8	8.2500	19.99	8.2481	0.0019	**0.0018**	**0.0006**
Molasses #2	2/5/2009	47	1	8.2497	20.00	8.2487	0.0009		
Batch 1, Bottle 20			2	8.2500	19.99	8.2464	0.0036		
			3	8.2500	19.99	8.2455	0.0045		
-Triggered SAMI			4	8.2500	19.99	8.2457	0.0043		
immediately after each			5	8.2500	19.99	8.2458	0.0042		
each measurement was									
finished			6	8.2500	19.99	8.2471	0.0029	**0.0034**	**0.0014**

Appendix B – pH Accuracy   128